POLITECNICO DI MILANO

Scuola di Ingegneria Industriale e dell'Informazione
Corso di Laurea Magistrale in Ingegneria Biomedica

A microstructural dosimetry model for the investigation of SIRT treatment

Supervisor: Prof. Gabriele Angelo DUBINI
Co-Supervisor: Ass. Prof. Johanne BEZY
Co-Supervisor: Ph.D. Elena CUTRI
Co-Supervisor: Ph.D Monica PIERGIOVANNI

Authors:
Federico BUDELLI Matr. N. 900387
Veronica CARCERERI Matr. N. 877078

Anno Accademico 2018-2019

LIST OF CONTENTS

LIST OF FIGURES

FIGURE **PAGE**

LIST OF FIGURES (CONTINUED)

FIGURE **PAGE**

LIST OF FIGURES (CONTINUED)

FIGURE **PAGE**

LIST OF TABLES

TABLES **PAGE**

LIST OF EQUATIONS

EQUATIONS **PAGE**

SUMMARY

The hepatocellular carcinoma (HCC) is the second (men) and sixth (women) most common cause of cancer-related death, due to its high incidence in developing countries and low curability. More than 700000 new cases appear every year and contributing factors to HCC are, mainly, chronic hepatitis (type B and C), in developing countries. In developed countries, the causes are more related to alcohol-related cirrhosis and obesity-related fatty livers.

Surgery is possible only for a small minority of all primary and metastatic intrahepatic tumors. The options for prolonged survival are chemotherapy, external beam radiation therapy (EBRT) transarterial chemoembolization (TACE) and radioembolization (RE), also referred to as Selective Internal Radiation Therapy (SIRT).

SIRT is a recently developed local treatment of intermediate and late stage HCC, which limits side effects and efficiently increases patients overall survival.

Specifically, such treatment consists in inter-arterial administering of radioactive microspheres, typically Yttrium-90 (^{90}Y), via catheter directly into the hepatic artery upstream from the tumor which then are, ideally, captured by the denser and more consuming vessels arterial network of the tumor.

The activity can be delivered through two different kinds of microspheres, namely resin (SIR-Spheres®), or glass (Therasphere®) spheres.

The work presented in this dissertation is part of a larger project, led by the “Laboratoire Traitement du Signal et de l'Image” (LTSI) of the University of Rennes 1 (France). The overall aim of this project is to optimize the SIRT through the developing of a full, patient-specific simulation of the treatment.

The treatment protocol presents numerous steps that have not been optimized yet, and still depend on the radiologist’s decisions. The tools available for the radiologist with the aim of tumor targeting are indeed limited, and the treatment is not currently planned in a full patient-specific way. To this aim, accounting for the different parts involved in this multidisciplinary process is mandatory. Specifically, image processing and protocol optimization for the

extraction of patients data, simulation of the patients vasculature, simulation of blood flow and of microspheres transport, simulation of microspheres distribution at liver's microscale and dose absorption will be taken into account. All the approved methods regarding the calculation of an absorbed dose assume that the distribution of microspheres is uniform. Based on recent observation it is not the case. The distribution of ^{90}Y microspheres is never uniform and the absorbed dose varies drastically on a microscopic scale. In the radioembolization treatment millions of individual sources are deposited inside the tissue. The deposition depends highly on numerous variables, like the blood flow and the catheter placement. This also impact on the release of the dose to the immediately adjacent tissues. The absorbed dose is therefore very heterogeneous when viewed on a microscopic scale and the non-uniformity at the microscale can lead to poor results of the treatment

In this context, the work here presented is devoted at the development of a microscale model of the liver based on a simplification of the hepatic lobule to investigate the dose delivered to the liver, analyzing then different scenarios (namely healthy and tumor liver), as well as different distributions of radioactive spheres in the lobules.

To this aim, an open source software, GATE, based on Monte Carlo method was used.

The Monte Carlo method is a statistical approach of deriving a macroscopic solution to a problem by the use of random numbers. It involves the random sampling of probability distribution functions (PDFs) that describe the problem of interest.

GATE offers well-validated physics models, geometry modeling tools, and visualization of the simulated doses by a three-dimensional rendering.

Different simulations of the hepatic lobules were performed. First, single-lobule simulations were performed to account for different microspheres configurations (in terms of amount of initial activity and spatial distribution) and different materials (normal liver tissue / tumor liver tissue). Specifically, four scenarios were taken into account: 1) one radioactive source placed in the middle of each hepatic arterioles (SL-UNIF); 2) three equidistant radioactive sources placed in three hepatic arterioles (SL-3M); 3) five equidistant radioactive sources in two hepatic arterioles (SL-5M); 4) one radioactive source placed in the middle of each hepatic arterioles of a pathological lobule (SL-Tumoral). Subsequently, a multi-lobule geometry was used to evaluate the effect of sources placed in a bigger portion of tissue and how they affect the total absorbed dose. Also in this context, different microspheres scenarios and materials were analyzed: 1) one radioactive source placed in the middle of

each hepatic arterioles of every single lobule (ML-UNIF); 2) one radioactive source placed in the middle of each hepatic arterioles of 81 lobules, collocated in the upper right corner (ML-NOUNIF); 3) one radioactive source placed in the middle of each hepatic arterioles of 81 tumoral lobules and of 9 healthy lobules adjacent to the pathological ones (ML-MIX); 4) one radioactive source is placed in the middle of each hepatic arterioles of 81 healthy lobules and of 9 tumoral lobules adjacent to the normal ones (ML-MIX 2).
For each simulation, the absorbed dose was evaluated to assess the local effects of the "injected" microspheres. Furthermore, the results obtained allowed to study the relationship between the initial administered activity and the related absorbed dose (Fig. I). When simulating the single lobule with different amounts of injected activity, a proportional relationship between the initial activity and the final absorbed dose was found. Then a single tumoral lobule was studied. Although with a not high discrepancy, the comparison of the results with respect to the ones regarding the healthy lobule showed a lower absorption of dose by the tumor tissue with respect to the healthy one. This behavior was expected due to the fact that the tumoral tissues are described as a denser tissue, as reported in literature.
From the analysis of the multi-lobule simulations, new considerations were arrived at.
The results indeed showed values of absorbed dose not proportionally related to the amount of initial activity set. This highlights the importance of the effect of the adjacent spheres placed in the surrounding lobules. In fact, considering a single lobule, this kind of effect is obviously neglected. On the contrary, in a multi-lobule configuration, the radiation from other sources placed in the lobules spread isotropically around each source, affecting and increasing the absorbed dose in all the others.
The investigation of the scenarios with the coexistence of healthy and tumoral lobules highlighted once again the difference in absorbed dose due to the presence of materials with different density.
On the basis of the results obtained, the models implemented in GATE proved to be valid and flexible, making especially the multi-lobule simulations an improvement to the current state-of-the-art regarding patient-specific models of SIRT treatment.

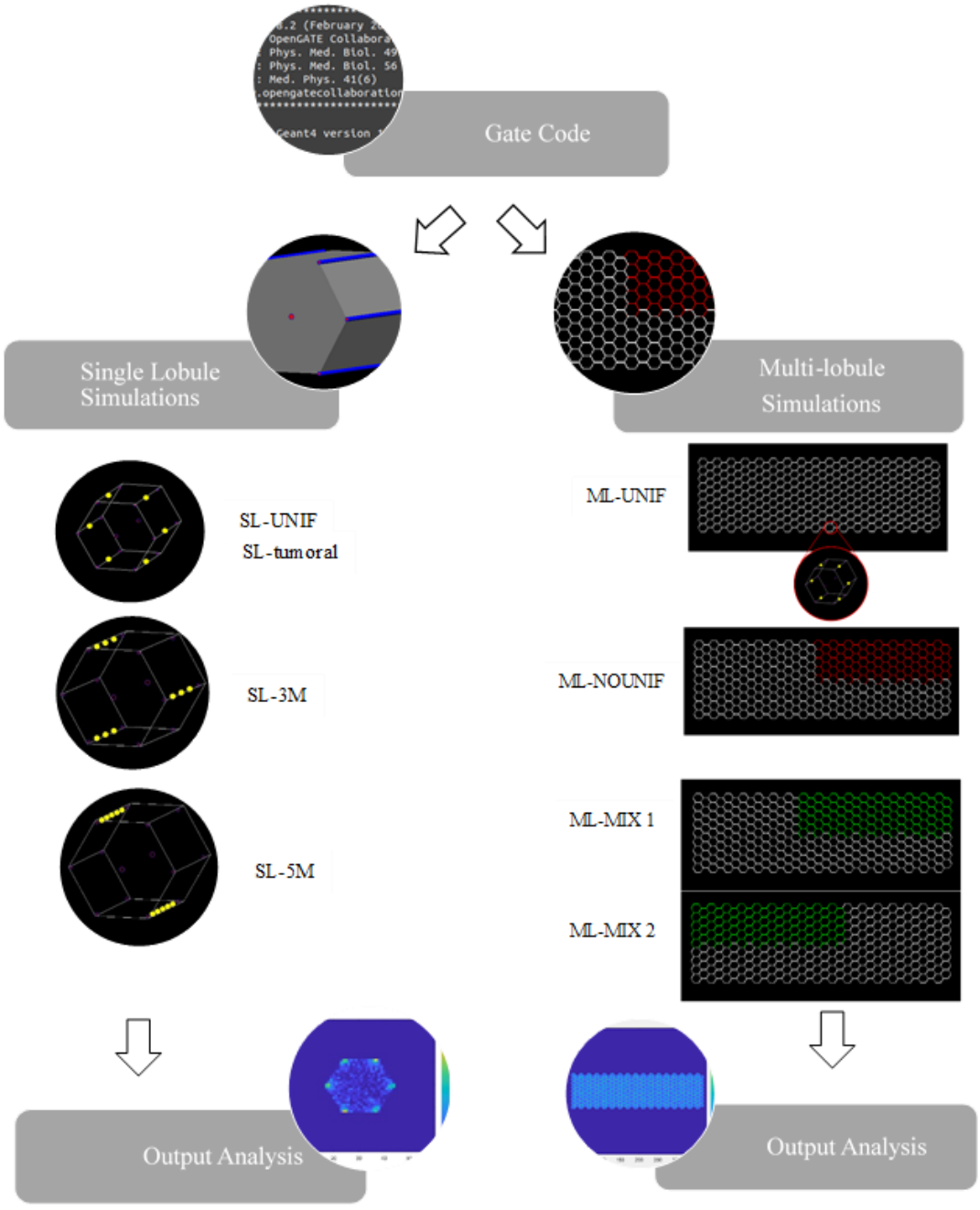

Figure I: Workflow of the project presented in this dissertation. First, the creation of the GATE code, in order to implement a microscale model of the liver based on a simplification of the hepatic lobule. Then, it was applied for single lobule simulations generating the relative outputs. Finally, it was applied to multi-lobule simulations with the respective outputs.

SOMMARIO

Il carcinoma epatico primario, principalmente denominato carcinoma epatocellulare (HCC), è la seconda (uomo) e la sesta (donna) causa più comune di morte per cancro, a causa della sua elevata incidenza nei paesi in via di sviluppo e della sua bassa curabilità. Più di 700000 nuovi casi compaiono ogni anno e i fattori che contribuiscono all'HCC sono, principalmente, l'epatite cronica (tipo B e C), nei paesi in via di sviluppo. Nei paesi sviluppati invece le cause sono maggiormente legate alla cirrosi ed all'obesità.
La chirurgia è possibile solo per una piccola minoranza di tumori intraepatici primari e metastatici. Le opzioni per una sopravvivenza prolungata sono la chemioterapia, la chemioembolizzazione transarteriale (TACE), la radioterapia a raggi esterni (EBRT) e la radioembolizzazione (RE), nota anche come SIRT (Selective Internal Radiation Therapy). Il SIRT è un trattamento locale recentemente sviluppato per la cura dell'HCC intermedio e in fase avanzata, che limita gli effetti collaterali e aumenta efficacemente la sopravvivenza globale dei pazienti.
In particolare, tale trattamento consiste nella somministrazione inter-arteriosa di microsfere radioattive, tipicamente ittrio-90, attraverso un catetere posizionato direttamente nell'arteria epatica a monte del tumore. Queste ultime vengono quindi, idealmente, catturate dalla rete più fitta di vasi che irrora la parte di tessuto tumorale.
L'attività può essere somministrata attraverso due diversi tipi di microsfere: sfere di resina (SIR-Spheres®) o di vetro (Therasphere®).
Il lavoro presentato in questa tesi è incluso in un più ampio progetto, guidato dal "Laboratoire Traitement du Signal et de l'Image" (LTSI) dell'Università 1 di Rennes (Francia). Lo scopo di questo progetto è quello di sviluppare una simulazione completa e paziente-specifica del trattamento SIRT. Il protocollo per il trattamento presenta numerosi passaggi che non sono tuttavia stati ottimizzati e dipendono ancora dalle decisioni del radiologo. Gli strumenti a disposizione del radiologo con l'obiettivo del targeting specifico del solo tumore sono davvero limitati e il trattamento non è attualmente pianificato in modo tale da essere paziente-specifico.
Per questo obbiettivo è necessario prendere in considerazione tutti i suoi passaggi multidisciplinari: elaborazione delle immagini e ottimizzazione del protocollo per l'estrazione dei dati del paziente, simulazione del sistema vascolare del paziente, simulazione

del flusso sanguigno e conseguente trasporto nei vasi delle microsfere, simulazione della distribuzione delle microsfere a livello microscopico all'interno del fegato e assorbimento della dose.

Tutti i metodi approvati riguardanti il calcolo della dose assorbita assumono una distribuzione uniforme di microsfere. Tuttavia, da recenti osservazioni, la distribuzione di microsfere non si presenta mai uniforme e la dose assorbita varia drasticamente in scala microscopica.

In tale contesto, il lavoro qui presentato si concentra sullo sviluppo di un modello alla micro-scala del fegato basato su una semplificazione del lobulo epatico, con l'intento di studiare le radiazioni assorbite dal fegato.

Al fine di raggiugere questo obbiettivo, è stato utilizzato un software basato su un codice Monte Carlo.

Il metodo Monte Carlo è un approccio statistico per derivare una soluzione macroscopica ad un problema mediante l'uso di numeri casuali. Esso implica il campionamento casuale di funzioni di distribuzione di probabilità (PDF) che descrivono il problema di interesse.

GATE offre modelli fisici ben validati, strumenti di modellazione geometrica e di visualizzazione della dose simulata tramite rendering tridimensionale.

Sono state quindi effettuate diverse simulazioni. Innanzitutto, sono state prese in considerazione le simulazioni su un singolo lobulo con diverse configurazioni di microsfere (in termini di quantità di attività iniziale e distribuzione spaziale) e diversi materiali (tessuto epatico normale / tessuto epatico tumorale). Nello specifico, sono stati indagati quattro scenari: 1) disposizione di una sfera radioattiva in ogni arteriola del lobulo (SL-UNIF); 2) disposizione di tre sfere equidistanti in tre arteriole epatiche (SL-3M); 3) disposizione di 5 sfere radioattive in due arteriole epatiche (SL-5M); 4) disposizione di una sfera radioattiva in ogni arteriola di un lobulo tumorale (SL-Tumoral).

Successivamente, differenti configurazioni sono state eseguite su di una geometria multi-lobulo, in modo da valutare l'effetto delle microsfere radioattive su di una superficie epatica maggiore. Anche in questo caso sono stati analizzati scenari differenti: 1) disposizione di una sfera radioattiva nel mezzo di ogni arteriola di ogni singolo lobulo (ML-UNIF); 2) disposizione di una sfera radioattiva nel mezzo di ogni arteriola di 81 lobuli (ML-NOUNIF); 3) disposizione di una sfera radioattiva nel mezzo di ogni arteriola di 81 lobuli tumorali e 9

lobuli sani adiacenti a questi (ML-MIX 1); 4) disposizione di una sfera radioattiva nel mezzo di ogni arteriola di 81 lobuli sani e 9 lobuli tumorali, adiacenti a questi (ML-MIX 2).

Per ciascuna simulazione sono stati quindi studiati i valori della dose assorbita nelle geometrie al fine di quantificare gli effetti locali delle microsfere "iniettate". Inoltre, i risultati ottenuti hanno permesso di studiare la relazione tra l'attività iniziale somministrata e la relativa dose assorbita.

Facendo riferimento alle simulazioni in un singolo lobulo, variando la quantità di attività inziale, è stata riscontrata una relazione proporzionale tra questa e la dose finale assorbita.

Successivamente, è stato preso in considerazione il caso di un singolo lobulo in condizione patologica (tessuto tumorale). Il confronto dei risultati tra la suddetta simulazione e quelle precedentemente effettuate (lobulo composto da tessuto sano) hanno mostrato un valore di dose assorbita finale inferiore. Questo comportamento trova spiegazione nel fatto che, come riportato in letteratura, il tessuto tumorale è descritto come materiale con una più alta densità.

Dall'analisi dei risultati ottenuti dalle simulazioni multi-lobulo, si è giunti invece a nuove considerazioni.

I valori di dose assorbita ottenuti mostrano infatti una non più lineare relazione tra il dosaggio e la dose totale assorbita. A differenza del caso del singolo lobulo, le microsfere infatti emettono radiazioni in modo omogeneo in tutto lo spazio, influenzando ed aumentando in tal modo la dose assorbita totale nei lobuli attigui.

Dall'analisi delle simulazioni multi-lobulo con la compresenza di tessuto sano e tessuto tumorale, è stata nuovamente dimostrata una differenza di dose assorbita causata dalla presenza di materiali con diversa densità.

Sulla base dei risultati ottenuti, i modelli implementati in GATE dimostrano di essere validi e facilmente modificabili in relazione alle configurazioni desiderate, rendendo specialmente le simulazioni multi-lobulo un miglioramento all'attuale stato dell'arte riguardante i modelli paziente-specifico di SIRT.

CHAPTER 1

1. Introduction

1.1 Liver anatomy and functionalities

Liver is the largest internal organ of the human body, accounting for approximately 2% to 3% (1,5 kg) of the total body weight of an adult, and is located in the upper right corner of the abdomen, below the lungs and the heart, and to the right of the stomach, intestine and spleen. In addition or because of its specific location and anatomy, the liver is one of the organs that handle the highest number of functions. The liver has indeed three main types of roles for synthesis, breakdown of molecules and storage. Firstly, the liver handles the synthesis of many molecules either by the metabolism of some or by the secretion of others (carbohydrates, proteins, fats). Secondly, the liver handles the breakdown of some molecules, in particular some drugs, hormones and toxins. Finally, the liver has also a storage role for many vitamins, glucose and iron [1][2].

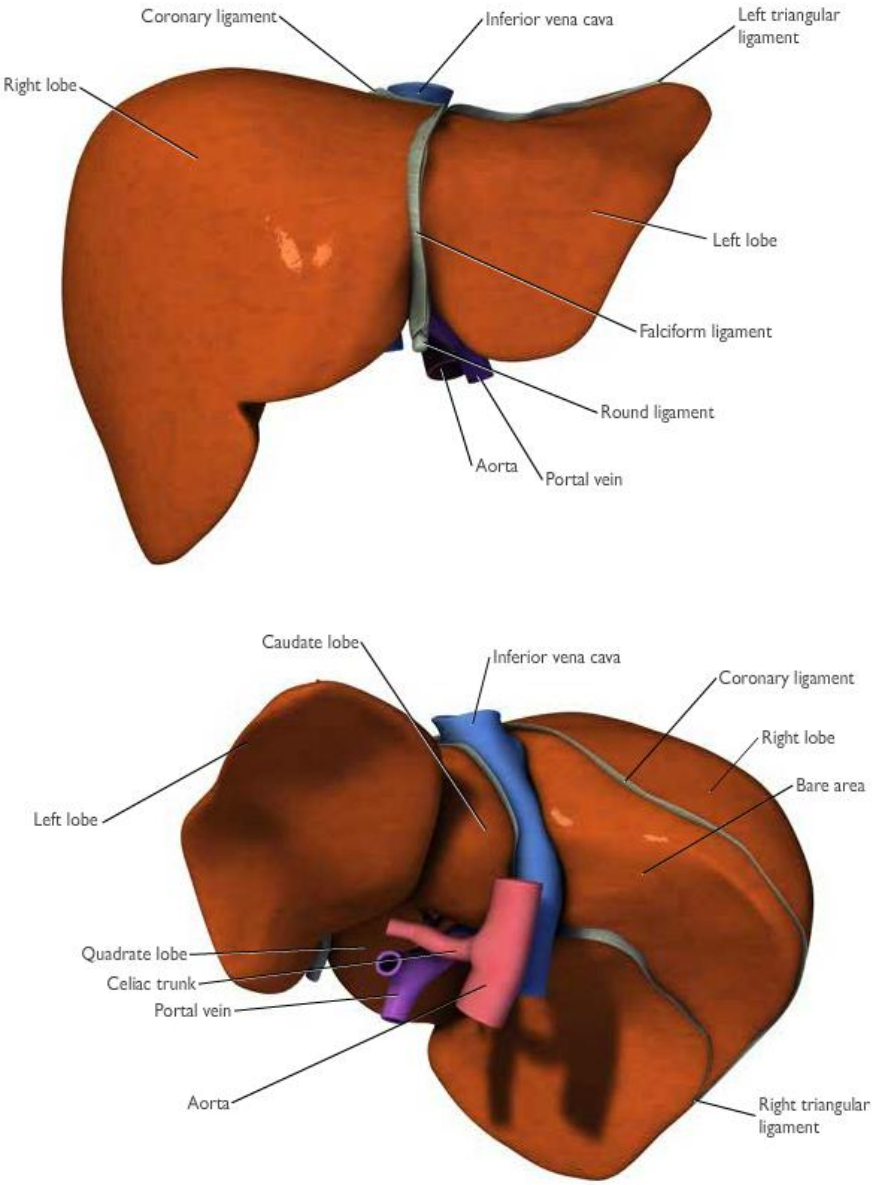

Figure 1: Views of front(top) and back (bottom) surfaces of the liver [7].

It is divided into four lobes. On the anterior surface, the falciform ligament marks the boundary between the left lobe and the right lobe. Then, the groove of the vena cava allows to divide the right lobe from the small caudate lobe; inferiorly to the latter there is the square lobe, between the left lobe and the gall bladder [3] (Fig 1).

As shown in Fig. 2, liver is often divided in eight anatomical segments that amount to independent vascular regions. These anatomical segments are especially relevant for surgical resection in case of tumoral lesions.

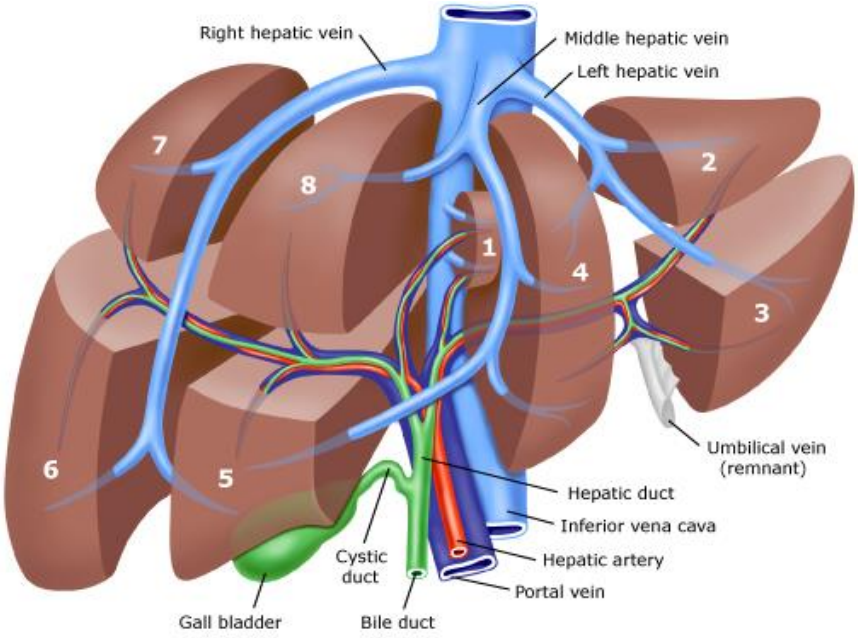

Figure 2: Liver division into eight segments by the hepatic veins [8]

The liver is a very vascularised organ and its vasculature is peculiar, due to its double blood supply. Indeed, it is uniquely divided between the hepatic artery, which contributes for the 25% to 30% of the blood supply, and the portal vein, which is responsible for the remaining 70% to 75% (Fig. 3). The former provides the liver with the oxygen, and the latter supplies the liver with the nutrients coming from the intestine. The portal vein brings about 1050 milliliters per minute, while additional 300 milliliters flow through the hepatic artery, for a total amount of about 1350 ml/min, which makes approximately 27% of the total cardiac output [3].

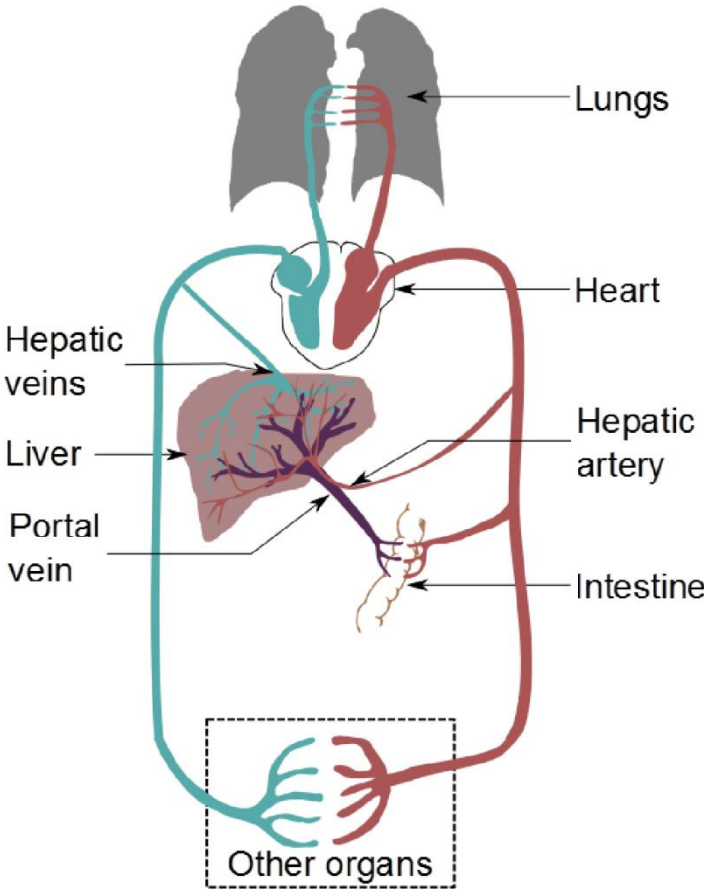

Figure 3: Human circulatory system with focus on the liver [9].

Hepatic artery takes origin from the celiac trunk, an artery bifurcating from the descending aorta before the renal arteries (Fig. 4). Before the bifurcation leading to the proper hepatic artery, the celiac trunk divides into the left gastric artery and next to the splenic artery. The section after this bifurcation is called the common hepatic artery. From the latter the gastroduodenal, the supraduodenal and the right gastric arteries sprout. Next, this same vessel is called the proper hepatic artery, and it further divides into left and right hepatic arteries, the latter being usually larger than the former, due to the volume proportion between the two lobes [4].

As illustrated in Fig. 4, the portal vein forms from the confluence of the superior mesenteric vein and splenic vein behind the neck of the pancreas. At the porta hepatis, the portal vein bifurcates into right and left branches before entering the liver. Then they branch and

rebranch within the liver to form a system that travels together in a conduit structure, the portal canal. From this portal canal, after numerous branching, the portal vein finally drains into the sinusoids, which is the capillary system of the liver. Here, in the sinusoids, blood from the portal vein joins with blood flow from end-arterial branches of the hepatic artery. Once passed through the sinusoids, blood enters the collecting branch of the central vein, and finally leaves the liver via the hepatic vein.

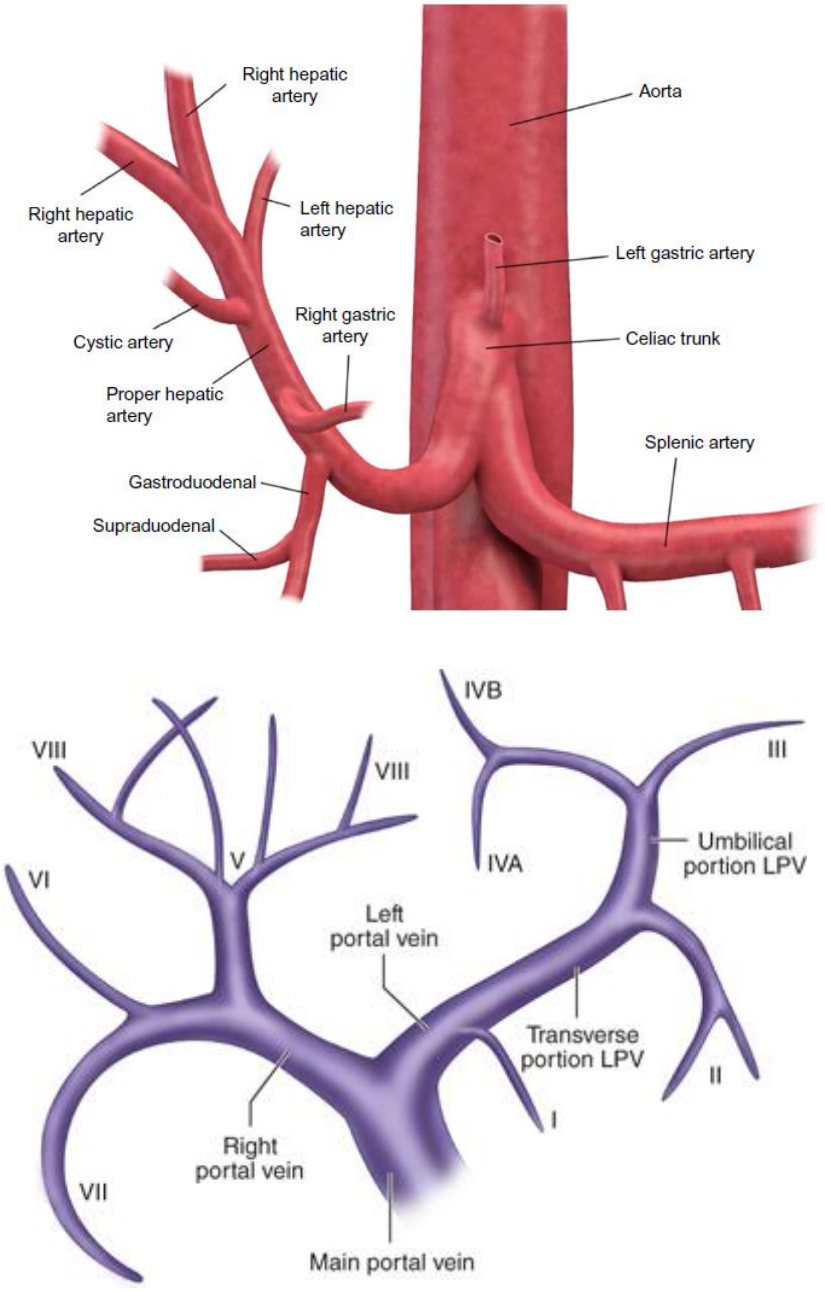

Figure 4: Major arteries sprouting from the celiac trunk (top);Branching pattern of the portal vein (bottom) [10].

The structure with portal canals draining into one central vein, is defined as a lobule (Fig. 5). It is the functional units of the liver and each lobe contains 100000 of them.

In general, each lobule contains one hepatic centrilobular vein and a number of portal tracts. A portal tract is composed of a hepatic artery, a portal vein and a bile duct. Both hepatic artery and portal vein distribute blood to the liver lobule via an irregular capillary network (sinusoids). Each sinusoid is lined with fenestrated endothelial cells that allow exchange of fluid and some metabolic substances between the sinusoids and the liver cells, called hepatocytes. Blood flow from the portal tract and through the sinusoids into the hepatic centrilobular vein undergoes repeated anastomoses with other hepatic centrilobular veins from different lobules to form a sublobular vein, and these veins merge together to form the hepatic vein, draining blood back to the heart via the inferior vena cava.

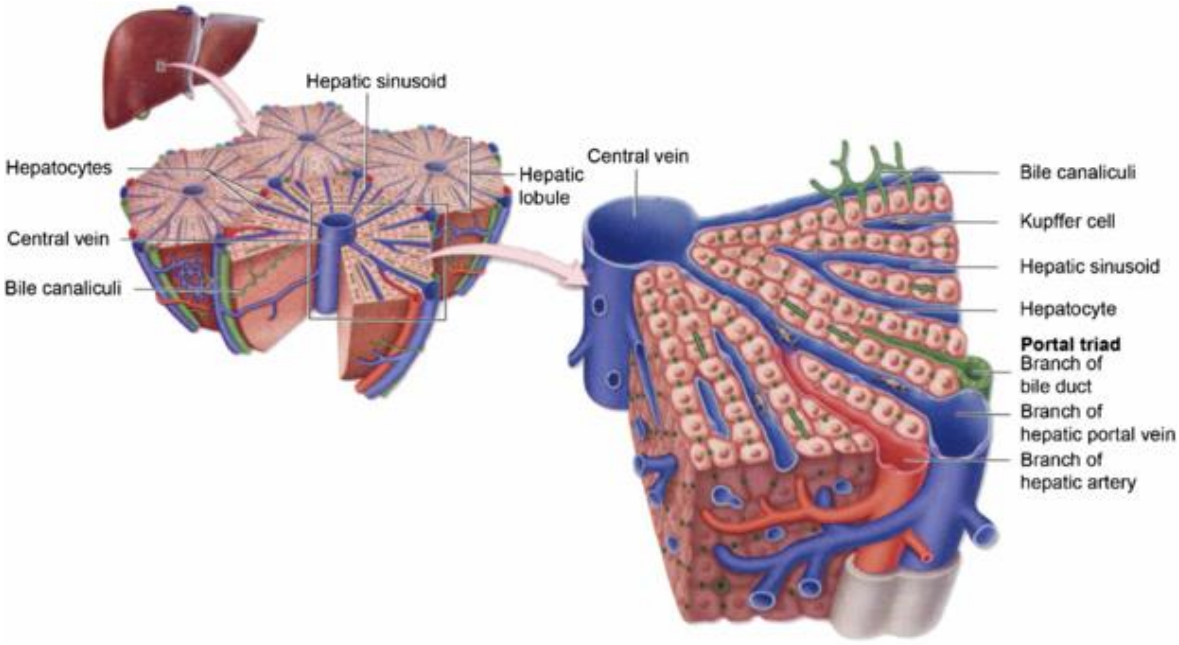

Figure 5: The liver lobule with central vein, portal tracts and sinusoids [11].

The number and the arrangement of the lobular vessels (centrilobular veins and portal tracts) in the histological sections are often irregular, and so over time a simplified model of the lobule has been proposed [1][2][3].

It is usually described as a classic 3D hexagon, with radius (*r)* of 0.6 mm and height (*H)* of 1.5 mm (Fig. 6). The centrilobular vein, set in the middle of the hexagon, has a diameter of 0.66 mm and the portal tracts are composed by the portal vein and the hepatic artery (with a diameter of 0.05 mm) [1][6].

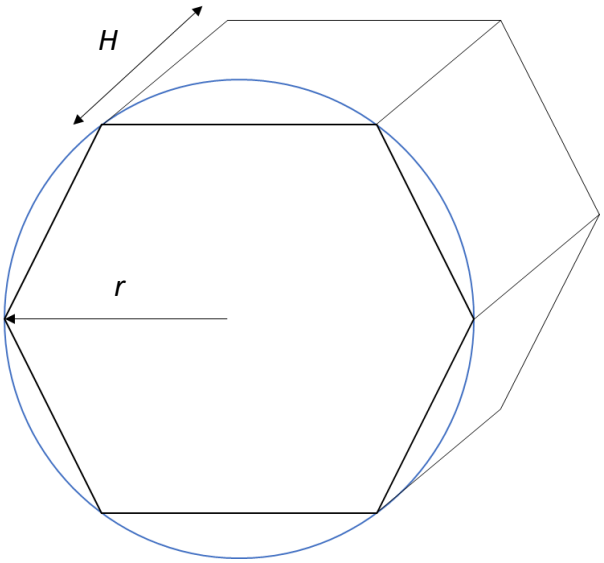

Figure 6: Simplified model of the lobule: 3D hexagon with radius r = 0.6 mm and height H = 1.5 mm.

It should be noted that the anatomy described above represents the standard pattern, but many kind of anomalies exist in number, size or position of this structure.

1.2 Hepatocellular carcinoma

HCC represents approximately 90% of all cases of primary liver cancer and it the fifth most common malignant tumor in men, the eight in women, with more than 800000 new cases worldwide per year [14]. Incidence rates vary widely between geographical regions and are highest in East Asia and Sub-Saharan Africa, where approximately 85% of all cases occur and the major contributor is the presence of hepatitis B. Nevertheless, also in Western countries with relatively low incidence rates, such as United States and Europe, incidence has increased in the last decade. In such countries the development of an HCC is mainly related to alcoholism, hepatitis C and non-alcoholic fatty liver disease [12].

Even if the portal vein contributes to 80% of the hepatic blood supply, a peculiarity of HCC is that it is mainly vascularized by the hepatic artery. Indeed, like most common cancers, HCC is a highly vascularized tumor. Neoplastic tissue requires a supply of oxygen and nutrients. Thus, avascular solid tumors only grow to a certain size and then undergo regression, if their metabolic demands are not met. For continued growth, it is necessary for a tumor to orchestrate the formation of a functioning system of blood vessels, which allows the delivery of metabolites (including growth factors) and cells (immunological cells and other cellular precursors) to the tumor environment. This arterial hypervascularization of HCC is the reason why the arterial supply of blood flow within the tumor is 3 to 7 times greater than in the surrounding noncancerous tissue [14].

According to the American Join Committee on Cancer, the classification of different stages of the tumor is based on microvascular invasion and tumor size. Four principal stages exist [19]:

- T1: the tumor is isolated and does not present any microvascular invasion.
- T2: multiple lesions smaller than 5 cm appear, or the tumor presents some microvascular invasion.
- T3a: multiple lesions bigger than 5 cm appear.
- T3b: invasion of a major branch of the portal vein or hepatic vein.
- T4: direct invasion of adjacent organs or perforation of the peritoneum.

2. State of the art

2.1 Treatments of hepatocellular carcinoma

Unfortunately, the diagnosis of HCC is too often made with advanced disease when patients have become symptomatic and have some degree of liver impairment. At this late stage, there is no effective treatment that would improve survival. But, with proper screening and vigilance, many patients can be diagnosed with early disease and preserved liver function. Currently, there are several treatment options, both surgical and nonsurgical, that can have a positive impact on survival [1]. For a tumor in an early stage the possibilities are liver transplantation, resection or percutaneous ablation by radiofrequency or microwave. Intermediate or advanced stage HCC can be treated with chemotherapy or the administration of chemoembolization through the vascular path. Radiotherapy can be administered (also as adjuvant to other treatments) at any stage of an HCC.
Surgical resection is the accepted treatment of choice for noncirrhotic patients and offers the best curative rate with a 5-year survival of 41%–74%. The resect ability of the tumor is dependent on the tumor size, location, underlying liver function, and whether or not the remaining liver volume will allow for resection without drastically increasing postresection morbidity and mortality. The candidates for this therapy are patients with a solitary tumor confined to the liver, no radiologic evidence of vascular invasion, and well-maintained liver function.
Liver transplantation is the treatment of choice in cases of HCC limited to the liver that cannot be submitted to surgical resection due to poor hepatic function or to technical impossibility. Liver transplantation not only eliminates the neoplasia but can also cure the base liver disease. Nevertheless, based on surgical data, the ideal candidate for liver transplantation is a patient with a single HCC smaller than 5 cm or with up to 3 nodules, none of them larger than 3 cm, without signs of neoplastic invasion of the portal system or of distant metastases. Despite its advantages, the procedure also involves some disadvantages. The lack of donors with a consequent increase in the time on the waiting list, the high cost of the procedure, the possibility of tumor recurrence and the frequent postoperative infections. With regards to the radiotherapy, the major limitation is the risk of causing radiation-induced liver disease. Therefore, it is important to develop local and

regional treatments. The peculiar vascularization of the liver has allowed the development of intra-arterial type therapies which allow the drugs to be administered selectively within the tumor via the hepatic artery system, minimizing the effects on the healthy parenchyma which is instead vascularized mainly by the portal system. These techniques include: intra-arterial injection of chemotherapeutic agents, radio-labeled particles, or non-reactive particles, with the only aim of embolization, i.e. of preventing the blood from delivering nutrients to the cancerous cells. Trans Arterial Chemo Embolization (TACE) is thus considered as the gold standard for treating intermediate stage HCC. It consists in the infusion of chemotherapeutic agents via the hepatic arterial blood supply, through a percutaneously placed trans-arterial catheter. Usually, it is then followed by a selective arterial embolization of the tumor vascular supply. Despite its advantages (decrease in tumor size between 10% and 60% of the original volume), complications in postembolization syndrome are present and severe and they include abdominal pain, nausea, ileus, and fever. A valid alternative is represented by Trans-Arterial Radio Embolization (TARE): it consists of the selective intra-arterial administration of microspheres loaded with a radioactive compound such as ^{90}Y or Lipiodol labeled with iodine by means of a percutaneous access. The latter is strong limited by the emission of high energy gamma radiation. On the other hand, ^{90}Y is mostly used. Indeed, it is a pure β rays' emitter with a maximum energy of 2.27 MeV and a mean of 0.9367 MeV [22][26]. It has been shown that TARE techniques have a far less embolizing characteristics than TACE and globally it gives equivalent results for early and intermediate stage HCC, with moreover fewer side effects [22].

2.2 Selective Internal Radiation Therapy (SIRT)

Selective Internal Radiation Therapy (SIRT) falls within the TARE framework. It is a radioembolization therapy during which microspheres containing radioactive ^{90}Yare administered through a microcatheter placed in the hepatic arterial vasculature to irradiate liver tumors from within. This therapy exploits the peculiar vascularization of the HCC: liver tumors are almost exclusively vascularized by the hepatic artery, whereas the healthy liver tissue receives most of its blood supply from the portal vein. Therefore, following the administration in the hepatic artery, microspheres will be carried preferentially toward distal arterioles in and around tumors (Fig. 7).

Clusters of microspheres are formed inside and in the periphery of the tumors, where they emit high energy β-radiation to induce cell death, while relatively sparing the healthy liver tissue [27].

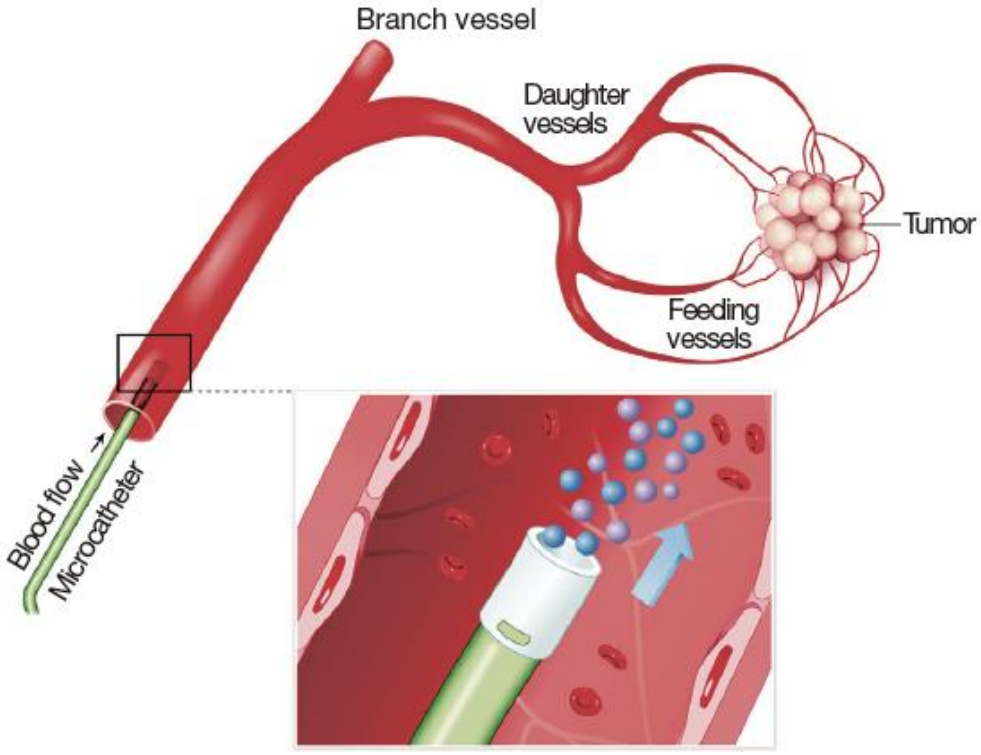

Figure 7: Injection of radioactive microspheres into the hepatic artery [35]

Microspheres continue to emit radiations during several weeks after injection, but radiation intensity decreases quickly to insignificant levels. The half-life of ^{90}Y is 64.1 hours, and 94% of the dose is emitted in 11 days while it decays to stable Zirconium-90 [28]. ^{90}Y is produced by bombardment of Yttrium-89 (^{89}Y) with neutrons in a nuclear reactor. Indeed, ^{90}Y is a pure (99.99%) β-emitter, with maximum and mean beta particle energy of 2.28 MeV and 0.934 MeV, respectively. It also produces 0.01% of 1.7 MeV photons along the way [12].

Beta decay (β-decay), otherwise called beta-minus decay happens in the nucleus of an atom. During β-decay, one of the neutrons in the nucleus turns into a proton and produces an electron. The electron that is created is a fast-moving electron that is released from the atom. These fast-moving electrons are called β-particles.

Atoms experience radioactive decay on the grounds that they are unstable. In particular, an atom that undergoes β-decay often has more neutrons in the nucleus than protons, making it unstable. By β-decaying, the atom can achieve a more stable arrangement of its protons and neutrons. This process gives off radiation in the form of β-particles or high-energy β-rays. In the case of ^{90}Y, the β-decay is described in this way:

$$Y^{90} \rightarrow Z^{90} + \beta^{-}$$

The maximum and mean penetration ranges of the β-particles are 11 mm and 2.5 mm, respectively, in water or soft tissue [28].

In patients with HCC, SIRT is generally reserved for patients with intermediate and early advanced diseases stages [27]. These are patients with large multinodular tumors, with or without macrovascular invasion or sufficient liver function.

Radioembolization is a minimally invasive, image-guided, locoregional alternative, or adjunct to more conventional therapies such as surgery, chemotherapy and external beam radiation therapy (EBRT). The advantages of this treatment are the targeted delivery of a very high radiation-absorbed dose to tumors, with limited systemic side effects and hepatotoxicity [26][29].

SIRT can be delivered through two different kinds of microspheres: glass ^{90}Y-microspheres (Theraspheres®, Nordion Inc. for BTG International, Ottawa, ON, Canada) and resin ^{90}Y-microspheres (SIR-Spheres®, Sirtex Medical Limited, North Sydney, Australia).

Glass microspheres are produced by incorporating ^{89}Y into the glass matrix of the microsphere and subsequent activation by neutron bombardment in a nuclear reactor facility. Compared to the others, Theraspheres® have a relatively high density and a high activity per sphere, such as 2500 Bq. Therefore, 10-20 times less particles need to be injected than with resin one to administer the same treatment activity. Consequently, the embolic effect is much smaller during the injection and the duration of the intervention lasts 2 – 5 minutes.
On the other hand, the production process of resin microspheres is different. Indeed, ^{90}Y cations in solution are chemically incorporated onto the bland microsphere surface. Because of this process, resin particles have a much lower density than glass one and lower activity per sphere, 50 Bq (Table 1).
Furthermore, the relatively low specific activity requires injection of a higher number of microspheres. Since this involves a greater embolic effect, stasis of blood flow may occur during administration. Hence, resin ^{90}Y-microspheres must be administered carefully by hand injection in smaller aliquots and the duration of the intervention can take up to 30 – 35 minutes in total [26][30].

Characteristics	**Glass Microspheres**	**Resin Microspheres**
Trade Name	Theraspheres®	SIR-Spheres®
Diameter (µm)	20 – 30	20 – 60
Specific gravity (g dl^{-1})	3.6	1.6
Specific activity (Bq/sphere)	2500	50
Material	Glass with ^{90}Y in matrix	Resin bound with ^{90}Y

Table 1: Properties of glass and resin ^{90}Y microspheres.

SIRT delivery requires truly multidisciplinary team approach involving nuclear medicine, interventional radiology and oncology. Radiologists assess liver tumor and extra-hepatic disease using computerized tomography (CT) or magnetic resonance imaging and interventional radiologists performed the required angiographies. Nuclear medicine and medical physics assist in SIRT dosimetry, delivery and radiation protection, while oncologist provide ongoing patient care [31].

The current protocol for the treatment of HCC involves different steps.

First, a cross-sectional pretreatment imaging is used for the evaluation of the liver parenchyma, vasculature and localization of liver tumors, their dimension and their relationship with surrounding vessels. CT and magnetic resonance imaging (MRI) play an important role. CT is faster, cheaper and higher in spatial resolution but nowadays the use of MRI is also increasing thanks to its less invasive nature and superiority in terms of soft-tissue contrast.

Subsequently, a preparatory angiography is performed through the injection in the liver arteries of an iodine-based contrast media and the consecutive acquisition of a 3D rotational Cone Beam CT-scan. The aim is to map the arterial anatomy and to determine the optimal injection point in the arteries.

The choice of this point is currently validated by the injection of a particular kind of human proteins, which are likely to imitate the behavior of the microspheres in its transport by blood [32]. Such protein is Technetium ^{99m}Tc albumin macroaggregate (^{99m}Tc-MAA). Furthermore, through a SPECT-CT, is estimated hepato-pulmonary shunt (Fig. 8) and an unintentional extrahepatic deposition.

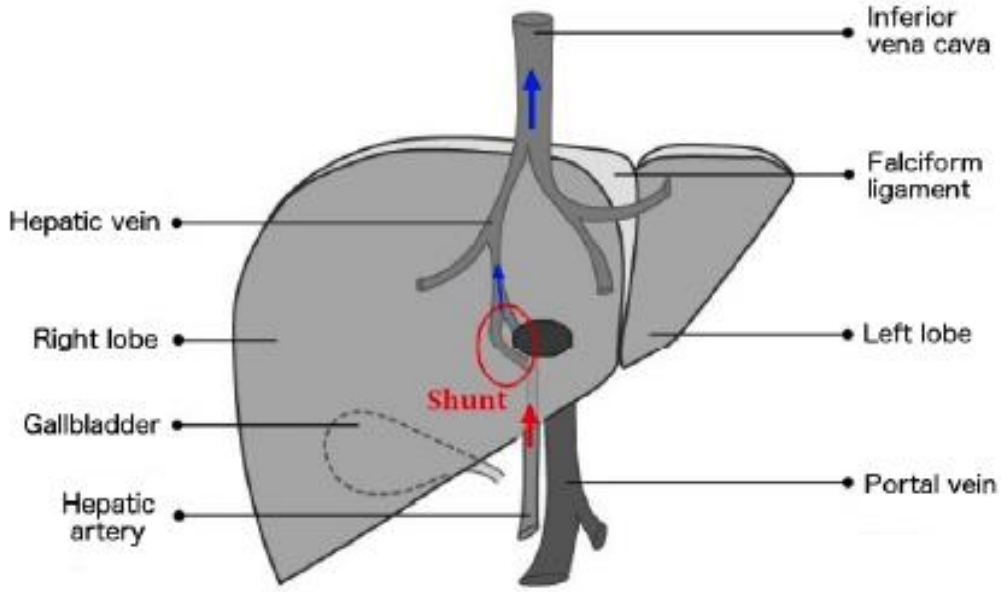

Figure 8: Schematic representation of an arteriovenous shunt induced by the presence of an HCC [5].

This diagnostic angiography also permits to determine the dosimetry. Indeed, the intrahepatic scout dose distribution should ideally be a good predictor for the treatment distribution, since determining the particle distribution in tumorous and nontumorous tissue (T/N ratio) would enable a patient-tailored treatment strategy [33]. The pretreatment activity/dosimetry calculations will be detailed in paragraph 2.6 then considered in detail.

Following this pretreatment workup, the intervention procedure is typically scheduled in 1-2 weeks. During treatment, radioactive microspheres should be administered at the same catheter position as during the preparatory angiography unless contraindications were discovered from the scout dose simulation.

Another SPECT/CT is then acquired to observe microspheres distribution and finally the SIRT efficacy is assessed by morphologic and functional imaging (MRI, CT) performed every 2 or 3 months.

2.3 Current limitations to SIRT

When performing the SIRT, the physicians have to face multiple clinical difficulties. Firstly, the choice of the injection point is of utmost importance to target the tumor and to avoid the delivery of the dose to healthy tissue. To this aim, the injection point is currently validated by the injection of a ^{99m}Tc-MAA. The choice of injection point is performed by the radiologist without any technological help, making it difficult to be reproducible and subject to human error.

Secondly, the potential extra-hepatic uptake, namely to the lungs or the digestive tract must be assessed. Indeed, it is essential that the lungs don't receive more than 50 Gy as cumulated radiation dose. A planar scintigraphy after the administration of ^{99m}Tc-MAA is also used to calculate the risk of extra-hepatic uptake of radioactive microspheres. Nevertheless, in patients with relatively hypovascular liver tumors, it has been demonstrated that the use of ^{99m}Tc-MAA itself leads to an overestimation of the true liver-to-lung shunting, probably due to the differences in particle characteristics, the broad range of ^{99m}Tc-MAA size and circulating free pertechnetate [37] [38].

In this context, it has also been noticed that difference in particle characteristics between ^{99m}Tc-MAA and ^{90}Y-microspheres, including different particle size, density, shape and number, strongly affects the particle distribution and consequently the calculation of the activity to be injected. [37][38].

Nevertheless, on the other hand, many authors have recently evaluated the validity of the administration of ^{99m}Tc-MAA in patients with markedly hypervascular HCCs. Indeed, in these cases the preferential tumoral blood flow is so strong that the differences in particle characteristics have less influence, making the ^{99m}Tc-MAA distribution a more reliable predictor [106][107][108][109].

However, in spite of variable correlation between ^{99m}Tc-MAA and ^{90}Y microspheres in the literature, the majority of authors agree that ^{99m}Tc-MAA is a good option for treatment planning and predictive dosimetry.

Lastly, the evaluation of the exact activity (or dosage) to be injected. This point plays an important role, since the dosage of ^{90}Y has a weak correlation to the absorbed dose that will be received by the patient's tumor, normal hepatic parenchyma, or extra hepatic tissues. Factors such as liver and tumor volume, lung shunt fraction (LSF) and catheter position form the complex relationship relating dosage to absorbed dose in a particular tissue. Commonly

accepted methods calculating average absorbed dose, some of which described later in chapter 2.6, assume uniform distribution of microspheres. In reality, the distribution of ^{90}Y microspheres is never uniform and the absorbed dose varies drastically on a microscopic scale. Radioembolization therapy indeed involves deposition of millions of individual sources, each capable of widely variable dose deposition to the immediately adjacent tissue. The absorbed dose is therefore very heterogeneous when viewed on a microscopic scale. There is potential for variable local dose deposition at different points within the tumor.

Another limitation to SIRT is its high cost compared to chemoembolization or to radiofrequency ablation [39].

Globally, SIRT is more efficient than other HCC therapies, but it still to be optimized in terms of time, cost, prevision and modeling. A numerical model of liver tissue, that involved blood and microspheres flow, microsphere distribution up to the microscale and the expected absorbed dose, would help the physician in the optimization of the treatment.

2.4 State of the art about SIRT modelling

A wide range of mathematical methods for the simulation of SIRT have been proposed in the literature. Indeed, a numerical model of the treatment would open the way to the possibility of numerically test different scenarios, analyze different results and automatically identify the optimal conditions for tumor targeting, predicting also the distribution of the microspheres and the amount of dosage to be injected.

As mentioned before, numerous steps are needed to achieve a complete simulation.

Concerning the vascular tree modeling, it has been highlighted that in vivo imaging does not provide sufficient details. Hence, an algorithmic concept for extending imaged vascular tree data is needed such that geometrically realistic structures can be generated. Significant improvements were obtained this last decade in the mathematical modeling of the hepatic vascular tree. Three different approaches are competing: constrained constructive optimization (CCO), deterministic geometric construction, and angiogenesis-based construction. Currently, CCO, introduced by Schreiner and Buxbaum in 1993 [114], is among them the most promising approach. The basic principle of CCO is to construct a strictly binary tree by adding one leaf node at a time to an initial tree, each time introducing an optimal bifurcation. Thus, CCO can be seen to be driven by the assumption of equal in- or outflow at all leaf nodes representing constant supply/drainage for each lobule. Moreover, at bifurcations the radii are balanced such that the flow resistance according to the Hagen-Poiseuille law is equal for both subtrees. This finally results in equal exit pressures at the leaf nodes [40]. The initial tree consists of a major hepatic vessel network obtained from CT angiography. Recently, Schwen et al. (2014) [41] proposed a simplified simulation of vascular tree. The model considers firstly the simulation of vasculature and tissue of the mouse liver, considering only two vascular trees, the one supplying blood, the other one draining it, and the parenchyma, represented at the length scale of lobules (~ 2 mm). The algorithm is initialized with two vascular trees segmented from in vivo micro-CT imaging, skeletonized and converted to a binary graph.

A similar method for the simulation of representative dog hepatic vasculature and tissue is proposed by White et al. (2016) [42]. The vascular model is developed starting from a 2D initial tree, then transformed into a pseudo 3D model in order to avoid vessels overlap between the two trees. Another method presented in literature is the one of Kretowski et al.

[115], in which the generation of growing three-dimensional vascular structures perfusing the tissue is described and applied to simulate the growth of liver vascular structures. The model is designed to simulate the development of a given extensive organ (starting with a small fraction of it), in which all cells are able to divide all along their life. The change in size and structure of the organ and the corresponding vascular trees operate at discrete time instants called cycles. The literature also proposes models specifically more linked to the simulation of SIRT treatment, namely including also the blood flow and microspheres distribution.

In this context, using the same CCO scheme, Walrand et al.(2014a) (2014b) [43][44] proposed a similar hepatic arterial tree growth model as the one described by Schwen et al for the SIRT simulation. [41]. Walrand et al. built indeed a full 3D hepatic arterial tree, optimizing though the total vessel length rather than the total vessel volume. When the arterial tree is built, the blood flow of all vessels is computed to ensure an equal blood flow to all the terminal triad arteries. Furthermore, microspheres distribution from larger arteries until portal triads is simulated by taking into account a constant symmetric or asymmetric probability at every bifurcation. The probability of each terminal triad artery trapping a microsphere was computed by following, in reverse, the artery path from the triad to the injection point. This model showed good results and it was able to well predict microspheres cluster size distribution, then better investigated by the works of Högberg et al. (2014) [111], (2015a) [112], (2015b) [113]. Indeed, Högberg et al. conducted a first real three-dimensional scanning of the microspheres clusters of a normal liver tissue explained 9 days after radioembolization, identifying two different types of clusters: linear clusters, described by a sequential of trapped microspheres in a terminal triad artery, and globular clusters that correspond to microspheres trapped in larger arteries. Although, linear clusters are well modeled by Walrand et al., globular ones are no present. In order to also simulate them, Högberg et al. developed another arterial tree model including an exponentially decreasing diameter of arterial branches from the main trunk up to the terminal triad arteries. A good agreement was obtained for the cumulated cluster size distribution and for the cluster frequency in the different artery generations as well.

In addition to the simulation of SIRT treatment, Basciano et al. (2010) [45], Kennedy et al. (2010) [46] modeled fluid dynamics and glass and resin ^{90}Y-microspheres transport in the four major branches of hepatic arterial tree, solving the blood governing equations through a CFD software. The computations were performed in steady flow and transient dynamics

and under the hypothesis that the presence of microspheres does not impact the fluid dynamics and the interaction between them can be neglected. The simulations showed that the microspheres partition at an arterial node does not follow that of the blood. In addition, it depends on the microsphere position in the vessel lumen prior to the node, the flow acceleration, the bifurcation angles of the daughter vessels and the catheter tip radial position.

The influence of such catheter presence on the flow is likewise a field of study. The most relevant works in this area are proposed by Kleinstreuer et al. (2012) [47], Childress et al. (2012) [48] and Kleinstreuer and Childress (2014a) [49].

Recent improvements in the context of CFD simulations were made. Through the Ansys-Fluent software, patient-specific simulations have in fact been proposed by Xu et al. (2016) and Aramburu et al. (2016a). The former research team proposes a simulation domain containing on a 3D but planar representative hepatic arterial system. Instead, the work proposed by Aramburu et al. proposed a CFD blood flow simulation using a patient-specific hepatic artery, made of circular vessels reconstructed form the clinical image.

Nevertheless, no methodology aiming to extract patient-specific vessels geometries in clinical routine is illustrated, and the proposed geometries are limited in number of bifurcations and affinity to reality.

Recently, some computer models have been developed also for microsphere absorbed dose distributions. Concerning it, Gulec et al. (2010) [34] performed the first simulation of cell-scale dosimetry applied to compare the effects of hepatic radioembolization using ^{90}Y-resin and ^{90}Y-glass microspheres. Gulec et al. (2010) used electron Monte Carlo tracking (MCNP software), proposing a model of lobular micro-anatomy based on simple geometrical shapes. It is assumed that all the hepatic lobules shared the same microsphere trapping pattern and different microstructural dosimetry model are compared. Through this model, the much higher radiations concentration at the portal tracts are compared to the surrounding parenchyma and central veins. Indeed, detailed specifics of the radiation dose deposition of ^{90}Y microspheres demonstrated a rapid decrease in absorbed dose in and around the portal tracts where the microspheres are deposited.

Another important work that describes the radiations distribution in the tissue is the one of Petitguillaume [110]. It is mainly focused on three steps: the simulation of a patient specific numerical 3D voxelised phantom, the mathematical estimation of the curve of the activity

distribution over time and finally a Monte Carlo (MC) patient specific simulation of the energy in every organ/tissue.

Yet with respect to the others, in this works, hepatic vasculature model and simulation of the injection of radionuclides in the arterial tree are not considered.

2.5 Dose absorption models

In radiation therapy the calculation of the absorbed dose represents a crucial point. In the case of radioembolization, the goal is to obtain a sufficient and effective dose absorbed by the tumor tissue, while limiting the absorbed dose by the normal liver tissue in order to prevent toxicity or undesired collateral effect. The uncertainty in dose is certainly far less than that in the biological effect on the tumor and normal tissues, particularly when the dose distribution is non-uniform. During the years many efforts have been made to create radiobiological models that aim to quantify the biological effect of any treatment plans and to compare their results [118][65].

The linear quadratic model (LQM) has been used to describe the radiobiological effects in several radionuclide therapies. Firstly, developed to analyze the effect during the electron beam radiation therapy (EBRT), the LQM has been reformulated to model therapies with continuously variable dose rate, and possible non-uniform absorbed dose distribution like radioembolization [52].

The principal quantity analyzed is the biologically effective dose (BED) [61][62]. The BED is defined in terms of both physical and radiobiological parameters and it is a measure of the total amount of lethal damage sustained by a specific tissue. The BED is obtained by multiplying the total physical dose with a modifying factor which takes into account the physical aspects of dose delivery:

$$BED_i = D_i \left(1 + \frac{D_i T_{rep}}{(T_{rep} + T_{phys})\, \alpha/\beta}\right) \qquad (1)$$

Being Di the locally absorbed dose, T_{rep} and T_{phys} the halftimes for cell repair after damage and the physical halftime of ^{90}Y, respectively. α and β denote the so-called intrinsic radio sensitivity and potential sparing capacity[59.]BED is here expressed for a single unit volume i like the voxel, a compartment or a specific region over which it is calculated. BED can relate also with the surviving fraction (SF) of a population of cells after irradiation following:

$$\ln(SF) = -\alpha\, BED \qquad (2)$$

To apply the same model in case of theoretical uniform irradiation, the BED values are converted in the equivalent dose at 2Gy/fraction (EQD2):

$$EQD2 = \frac{BED_x \alpha/\beta}{2+\alpha/\beta} \qquad (3)$$

Furthermore, spatial non-uniformities can be normalized to a single number, called equivalent uniform biologically effective dose (EUBED) [63]. This number is the same for different absorbed dose distributions that have the same biological effect. EUBED can be defined as:

$$EUBED = -\frac{1}{\alpha} ln\left(\frac{\sum_i e^{-\alpha BED_i}}{n_{voxel}}\right) \qquad (4)$$

Where n_{voxel} is the number of voxels in the volume of interest under study.

This approach will help in evaluating risks and benefits of an individual absorbed dose distribution, as clinical outcome can be linked to a single number like BED or $EUBED$.

The main goal of radioembolization remains the evaluation of the absorbed dose for the planning of the radiotherapy treatment. The absorbed dose is a physical dose quantity representing the mean energy imparted to matter per unit mass by ionizing radiation. The SI unit for the absorbed dose is Gray [Gy], equivalent to J/kg. In the literature, different methods for the dose calculation, based on different parameters, has been developed during the years [51]. The recent studies are focusing on patient specific methods that take into account the specificity of the tumor treated, to better predict biological effect of dose distribution and reducing the side effects of the treatment.

2.5.1 Partition model

The partition model is a model that allows to estimate the activity of an administered dose of ^{90}Y microsphere partitioned into three compartments: tumor, normal liver and lung tissue[65]. The activity in each compartment is firstly verified by the distribution of 99mTc-MAA , then the tumor to normal liver ratio is calculate as follow:

$$TN = \frac{A_T\,[Mbq] / Mt\,[Kg]}{A_{NL}[Mbq] / M_{Nl}[Kg]} \qquad (5)$$

where A and M indicate the activity and the mass of the tumor (T) and normal liver tissue (NL) compartments. The estimated TN liver ration not always match the true TN ratio due to differences between the 99mTc-MAA particle and the microsphere used in the treatment. They in fact can differ in size, weight, administration (microcatheter placement, local change in the blood flow).

The intrahepatic activity to be administered in each compartment is chosen with the evaluation of the TN value and the segmentation of the compartments. Each compartment can be segmented with two different technique: segmentation on an anatomical image (contrast enhanced CT) or with a functional modality (SPECT thresholding) [59]. These compartments are matched with the distribution of 99mTc-MAA in order to quantify the dose to each compartment. The goal is to maximize the dose injected to the tumor while reducing the dose that reach the normal liver and the lung tissue.

The prescribed activity is then computed:

$$A\,[GBq] = D_{NL}[Gy]\,\frac{TN\;\; M_T\,[kg] + M_{NL}[kg]}{50\left[\frac{J}{GBq}\right](1-LSF)} \qquad (6)$$

where D_{NL} indicates the absorbed dose to the parenchyma, LSF the lung shunt fraction, $M_{NL,}$ MT are respectively the mass of the normal liver and the tumor compartment. With this calculation the dose is supposed to be deposited just in the compartment in which the activity is administered neglecting the effect and the activity coming from other compartments, therefore this is a simplification.

This method accounts for tumor avidity and liver involvement, it is based on whole liver infusion, and it considers the lung safety through the use of LSF parameters for activity calculation.

Lung shunt fraction is defined as:

$$LSF = \frac{C_{lungs}}{C_{lungs}+C_{liver}} \qquad (7)$$

Where C_{lungs} indicates the total counts in the lungs, and C_{liver} the total counts in the liver. Lung shunting could potentially result in radiation pneumonitis after radioembolization. At higher shunt fraction, it may be necessary to reduce the prescribed activity of microspheres so that the know upper radiation dose limit recommended of 25 Gy for Y90 is not exceeded. The highest tolerable lung shunt absorbed dose was defined as 30 Gy after a single treatment and up to 50 Gy after repeated treatments [66]. Patients who have considerable shunting of the activity to the lungs, typically greater than 20% shunt value or 16.2 mCi (600 MBq) delivered lung activity, should be disqualified from the use of microsphere brachytherapy [60].

However, the partition model does not consider the activity nonuniformity within each partition. Furthermore, the partition model cannot be accurately used for diffused tumors where tumor extent cannot be determined with confidence. A typical dose between 100 and 120 Gy is selected for Therasphere® treatments involving patients with HCC [53].

2.5.2 BSA method

The BSA-based method is the most commonly used method in radioembolization with resin microspheres, partly because of the large embolic load that such low-activity microspheres require to deliver adequate radiation. It is based on the observation that BSA correlates with liver volume in the healthy population. Thanks to this evaluation, the activity is administered based on the specific liver volume for each patients, derived directly from the weight and height of the patient. The activity is calculated according to the following relationship:

$$A\,[GBq] = (BSA\,[m^2] - 0.2) + \frac{V_{tumor}}{V_{tumor} + V_{normal\ liver}} \qquad (8)$$

where V_{tumor} and $V_{normal\ liver}$ liver indicate the volumes of the tumor and the healthy parenchyma, respectively.[59]

And the BSA is calculated as:

$$BSA\ [m^2] = 0.20247\ x\ height\ [m^2]0.725\ x\ weight[kg]0.425 \qquad (9)$$

This method is strongly dependent on the patient's height and weight and not that much dependent on the tumor infiltration. It assumes a relationship between the size of the patient and the ability to tolerate the dose. This method takes into account a radioembolization to the whole liver, so when considering a lobar or more selective treatment, the activity is reduced in proportion to the size of the liver volume being treated and the formula needs to be adjusted as:

$$A\ [GBq] = ABSA\ [GBq]\ [\frac{V_{treated}}{V_{whole\ liver}}] \qquad (10)$$

However, there is experimental evidence that the BSA method does not correlate with the liver mass or with the tumor involvement [66]. It should not be misconstrued in terms of tailored evaluation, as it neglects the individual T/NL avidity ratio, which is patient specific. Furthermore, the interindividual differences in microsphere distribution are not covered, limiting the use in patient-specific treatments.

2.5.3 MIRD mono-compartment

This method relies on a simplified dosimetry equation of the multi-compartmental model, here an absorbed dose, to the whole liver or lobe is empirically prescribed [52][50]. For glass microspheres, the activity calculation is based on the desired mean absorbed dose to the target liver mass (independent of tumor burden), following:

$$A\ [GBq] = \frac{Desired\ dose\ [Gy]\ x\ M_{target}\ [kg]}{50\ [\frac{J}{GBq}]} \qquad (11)$$

The recommended absorbed dose can vary in an interval between 80 to 150 Gy, depending on the case for every patients, and their specific tumor. When setting the desired absorbed

dose, the evaluation is made over the assumption of homogeneous distribution of spheres inside the treated region, even if it is an incorrect assumption, that largely approximate the sphere distribution inside the tumor[59]. The absorbed doses to tumor and normal liver are not separately calculated. No distinction is made for different tumor involvement and avidity. The target mass may be determined using either CT, MRI, PET, or 99mTc-MAA SPECT [67].

No liver toxicity nor efficacy threshold accompanied this methodology.

For determining the actual liver dose [Gy] delivered to the liver after injection, the following formula is used:

$$Dose\ (Gy) = \frac{50\ [\text{Injected Activity (GBq)}]\ [1-F]}{\text{Liver Mass (kg)}} \qquad (12)$$

where F is the fraction of injected radioactivity localizing in the lungs, as measured by Tc-99m MAA scintigraphy. The estimated total activity shunting to the lungs should not exceed 610 MBq, which equates to approximately 30 Gy in 1 kg lung tissue [67].

No distinction is made for different tumor involvement and avidity.

However, the average absorbed dose evaluated by the partition model or the MIRD formalism does not consider the heterogeneous activity distribution and energy deposition in the tissues.

2.5.4 Voxel based method

The voxel based method takes into account the single voxel as the unit on which calculate the dose. It gives the possibility to calculate the dose on a really small spatial unit, a big advantage compared to the multi-compartmental model in which the dose is obtain for larger compartments. Moreover, since the voxel can be a very small units (depending on the choice of its size) it makes it possible to evaluate the inhomogeneities in the sphere distribution that occurs at smaller scale as well as the change in the related absorbed dose. However, voxel-based dosimetry for radioembolization is based on nuclear medicine images (SPECT-CT, PET-CT images), which are generally noisy and of low resolution [56][57]. The voxel dose can thus be estimated with the formula:

$$D_{voxel} = A_{voxel}\ x\ S_{voxel} \qquad (13)$$

where S_{voxel} is the MIRD Snyder factor, it represents the voxel absorbed dose per one decay. They are obtained from the online free database http://www.medphys.it/ for the specific voxel size values. A_{voxel} (Bq·s) is the voxel cumulated activity (i.e. the integral activity over the time) equal to:

$$A_{voxel} = 1.443\, A_{voxel}\, T_{1/2}(90Y) \qquad (14)$$

Where A_{voxel} is the initial activity into a voxel and $T_{1/2}(90Y)$ in the physical ^{90}Y half-life. Since the total administered ^{90}Y activity is completely uptake into the treated liver lobe, the activity into the single voxel can be derived through the following simple proportion (patient-relative calibration method) [58]:

$$A_{voxel} = \frac{A_{liver}}{C_{liver}} C_{voxel} \qquad (15)$$

where C_{liver} and C_{voxel} are the counts in the total liver and in the voxel, respectively. This simple approach, called relative calibration method, do not require an absolute activity PET-CT scanner calibration.

Also, for the voxel dose method, the LSF can be taken into account subtracting from the A_{liver} the fraction of the lungs.

2.5.5 Dose-Voxel-Kernel (DVK)/ Dose-Point-Kernel (DPK)

An increase in computing speed has made it possible to implement dosimetry calculations based on volumetric integration. The dose-point kernel or dose-voxel kernel plot the energy absorption in a homogeneous medium around a source point or a voxel source respectively, according to the distance to the source. This kernel can also be scaled to different local tissue densities. The dose deposited in a voxel centered on *r* is a result of the activity contained within the central voxel as well as the activity contained in the surrounding voxels. The contribution to the central voxel dose from the surrounding voxels is a superposition of the dose distributions due to the activity in each surrounding voxel, using the activity as the weighting function [53].

Dose-voxel kernel can be calculated from integration of dose-point kernel or by direct Monte Carlo simulations.

The basic approach to kernel convolution dosimetry is to convolve a 3D in vivo activity distribution with a Monte Carlo derived 3D dose kernel. For a homogeneous medium, the dose calculation is conducted using the convolution integral:

$$D(\vec{r}) = \int \acute{A}\left(\overrightarrow{r'}\right) K\left(\vec{r} - \overrightarrow{r'}\right) d\overrightarrow{r'} \qquad (16)$$

where $D(\vec{r})$ is the absorbed dose [Gy] in the central voxel, centered at location $\vec{r}$, $\acute{A}\left(\overrightarrow{r'}\right)$ is the cumulated activity (Bq-s) at location $\overrightarrow{r'}$, and $K\left(\vec{r} - \overrightarrow{r'}\right)$ is the spatially invariant dose deposition kernel (Gy Bq^{-1} s^{-1}) between location $\vec{r}$and source location $\overrightarrow{r'}$.

The convolution of dose-point kernel has the advantage of being a one-dimensional representation of the energy deposition but requires integration within the voxels to consider their geometry. Voxel S values, also known as dose-voxel kernel, were proposed in MIRD Pamphlet #17 [73] to overcome this limitation.

The advantage of the convolution of dose-voxel kernel is its easier implementation compared to dose-point kernel, but one downside is that they depend on the voxel dimensions. Another downside of dose-voxel kernel convolution is the inability to consider tissue density heterogeneities.

2.5.6 Local deposition method (LDM)

This method constitutes applying an appropriate scaling factor to the voxel activity concentration values. It is based on the simplification that all emitted energy within a voxel is absorbed locally, within that same voxel. Another assumption is that radioembolization is a permanent implant with a relative distribution that does not change following infusion.

The calculation of the absorbed dose is than given by:

$$D_{90Y}[Gy] = \frac{A_0\left[\frac{Bq}{mL}\right] x\ 4.986\ x\ 10^{-8}\ [Js]}{\rho_{liver\ [\frac{kg}{mL}]}} \qquad (17)$$

Although the results of these techniques are almost equivalent, LDM is suggested due to the benefits of simplistic implementation and no post-processing request [54].

2.5.7 Microdosimetry model

Microdosimetry refers to the analysis of variable absorbed doses to the tissue immediately adjacent to a single source on a microscopic level. Microdosimetry underlie the differences in the dose response at the microscale level and helps to explain the main differences between radioembolization and external beam radiation therapy (EBRT). Indeed, while radiation-induced hepatitis can occur at 30 Gy in external beam radiation therapy, similar toxicity from ^{90}Y microspheres appears at higher absorbed dose level. Many studies have examined this issue.

Gulec at al. developed a hexagonal model for hepatic lobules for the Monte Carlo computation, inclusive of all contributions to the absorbed dose in a given 3D volume. They show the non- uniformity of dose absorption in the tissue depending on the distance from the source. A strong limitation of this model is the evaluation of the total absorbed dose for one single lobule and the approximation of the contribution of the adjacent lobules through the use of reflective boundaries [55].

Walrand et al., developed a radiobiologic model for the analysis and the evaluation of the micro dosimetry dose, based on a single lobule dose-death probability relationship. The lobule model used was the one developed by Gulec et al. but with the analytic Russell's dose distribution kernel [43]:

$$D(r) = 0.989A\frac{1-r/8}{r^2} \qquad (18)$$

The Russell's law results were in good agreement with the dose kernel obtained from various Monte Carlo codes. This method has the major benefit to allow the computation of the microscale dosimetry of all the 10^6 liver lobules [43].

Both studies show that the radiation dose varies in the tissues, depending on the type of tissue considered and on the distance from the sources. At the microscopic level the dose distribution is highly heterogeneous, tissue close to the source will receive a high amount of radiation while tissue at few millimeters will receive a non-lethal dose [60].

2.6 The Monte Carlo method

The calculation of absorbed dose on a microstructure scale will require a full representation of the radiation emission, the radiation transport through the regions of interest defined within the tissue and the energy deposition in each of the individual microstructures.
The full representation of every individual particle, which will be needed for absorbed dose calculations on a microstructural scale, will require a powerful simulation method recording the interaction and thus, if existing, absorption position of each emitted particle.
This can be done by MC simulations.
The name "Monte Carlo" was coined in the 1940s by scientists working on the nuclear weapon project in Los Alamos, to designate a class of numerical methods based on the use of random numbers.
The MC method is a statistical approach of deriving a macroscopic solution to a problem by the use of random numbers. It involves the random sampling of probability distribution functions (PDFs) that describe the problem of interest. Provided that the algorithm is accurate, and the physical system is well modeled, repeated sampling of the distributions will converge to the correct solution.
This gives the MC methods a great flexibility. The MC methods can therefore be applied on problems with no probabilistic content as well as to problems whose inherent structure is probabilistic [68][69].
MC methods usually follow different approaches, depending on the particular field of application. However, all these approaches tend to follow a particular scheme:

- A probability distribution that describes the system being analyzed.
- Generation of a random number.
- A rule used to sample the probability distribution from the generated random number, typically based on the underling dynamics or physics of the system under investigation.
- Variance reduction techniques to reduce computational time.

- A history of the interested quantities.

Thus, the MC methods are a collection of different methods that perform the same process: this process involves performing many simulations using random numbers and probability distributions to get an approximation of the answer to the problem [70].
At the heart of any MC method there is a random number generator. They are based on repeatable mathematical algorithms and can produce an infinite stream of random variables that are independent and identically distributed according to some probability distribution.
One of the simplest random distribution is the Linear Congruential Generator function, defined by:

$$X_{n+1} = (a\,X_n + c)\ mod\ m \qquad (19)$$

Where X_{n+1} is the sequence of random numbers, X_n the starting number, a and c two variables and m shows the maximum value that the formula can produce [70][71].
It is possible to define some desirable, or indeed essential, properties of a good uniform random number generator:

1. Absence of correlation between the numbers of the sequence.
2. Uniform distribution of the values in the sequence.
3. Low computational time.

MC methods have the capacity to increase the speed of some numerical computations and to allow simulation of physical process governed by probabilistic laws. The technique has been applied in problems across finance, molecular structure, systems biology, and most importantly for this dissertation, medical physics, where MC simulations have become the gold standard for dosimetry.
In the work described in this thesis, the MC method was used for dosimetry calculations in which the energy depositions caused by interacting photons and charged particles emitted from a radioactive source were calculated and tallied (scored) in various target regions.

Indeed, the stochastic nature of particle interactions makes them ideal to model with MC methods.

In the MC simulation of radiation transport, particles travel in discrete steps and undergo various types of interactions along the way. The history of a particle is viewed as a random sequence of free flights that end with an interaction event where the particle changes its direction of movement, loses energy and, occasionally, produces secondary particles. The step length and the type of interaction are sampled from cross section data. Sampling of the appropriate differentia cross sections, random histories can be generated and so energy and direction of the resultant particles can be determined. The integral parts of the code include: the cross-section data of the processes to be simulated, the particle transport algorithms, the specifications of the geometries and quantities to be scored, as well as the analysis of the simulation.

In short, a distance of travel is selected before an interaction occurs, the type of interaction is determined based on the interaction cross-sections (provided the distance travelled did not bring the particle outside the treatment geometry), and the resulting particle types, energies, and directions are determined for each interaction, all of which use the production of random numbers in their calculations [71] (Fig. 9).

This continues until all particles are removed from the simulation geometry or the particle energies fall below set thresholds.

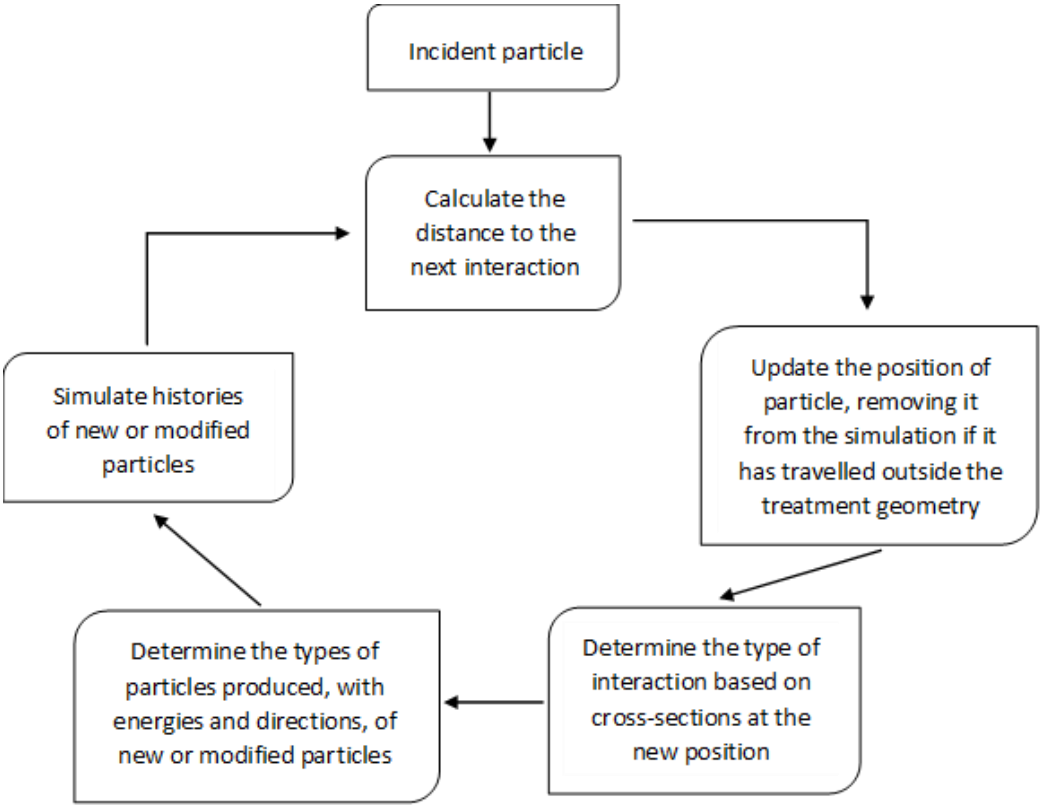

Figure 9: Flowchart describing the basic elements of a Monte Carlo simulation of charged particle transport.

It is certainly a necessary, if not sufficient, condition that one takes into account accurately all the relevant physical processes in electron-photon transport if the Monte Carlo technique is used to provide an accurate simulation.

2.6.1 Photon interaction processes

In photon transport, the major photon interactions with matter include the photoelectric effect, Compton scattering, pair production, Rayleigh scattering and photonuclear interactions. Among these interactions, the first three are the most important, because they lead energy to transfer to secondary electrons. Fig. 10 illustrates the regions of their relative predominance as delimited by the lines where the atomic cross sections of the interactions are equal.

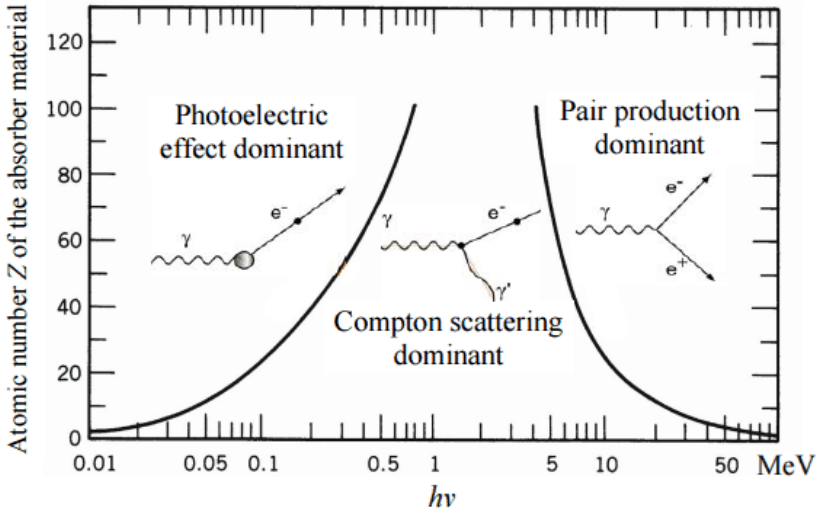

Figure 10: Relative importance of the three major types of photon interactions with photon energy and the atomic number of the attenuating material as parameters [73].

In a photoelectric interaction, the incident photon transfers all of its energy to an atomic electron. The photon gets absorbed and the electron is ejected with a vacancy left behind. The electron is mostly emitted from the closest shell to the nucleus (k-shell), and its binding energy must be less than incident photon energy. The vacancy will lead to a cascade of electron transitions form outer shells to the inner ones (Fig. 11). These transitions will in turn give rise to characteristic X-rays, Auger electrons or Coster-Kronig electrons [73][74].

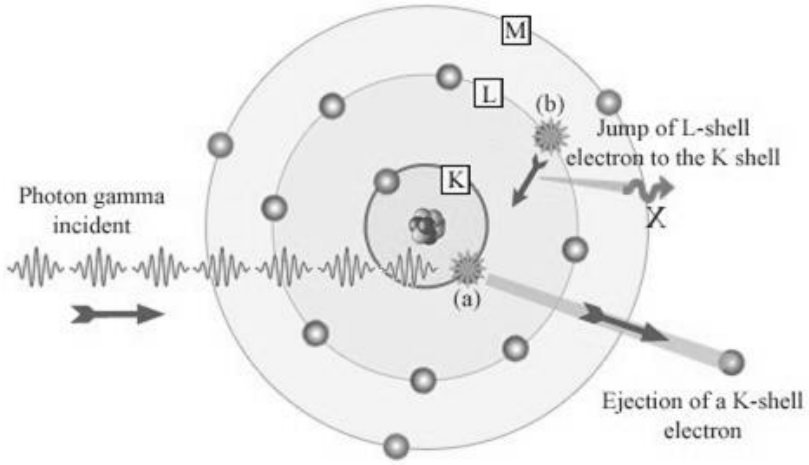

Figure 11: Schematic representation of photoelectric effect [79].

The Compton scattering is a form of incoherent scattering photon and electron interaction, in which the collision is between the incident photon and an outer-shell orbital electron of an atom.

In Compton scattering, the energy of the incident photon very much surpasses the binding energy of the electron in the atom [74].

The difference between photoelectric effect and Compton effect is that the photon is not absorbed, it is scattered with a reduced energy at an angle θ (Fig. 12).

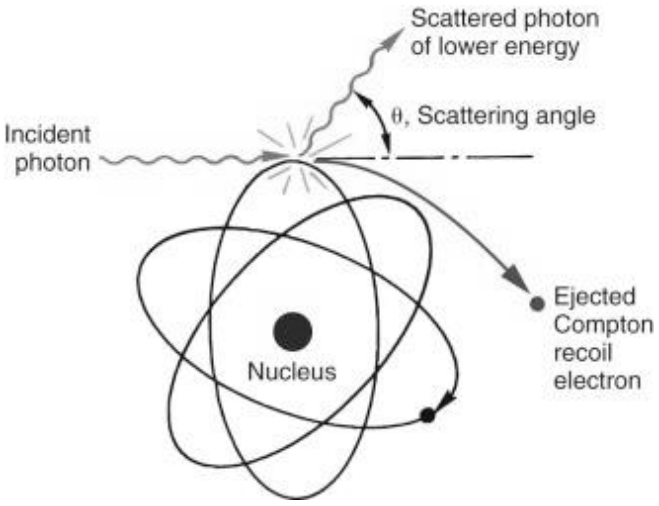

Figure 12: Schematic representation of Compton scattering [79].

Pair production occurs when a photon interacts with the electric field of charged particles surrounding the nucleus. This interaction leads to an electron and positron pair. Pair production can only occur when the energies of incident photons exceeds 1.02 MeV, that is the rest mass of the positron and of the electron. This energy is used to produce the positron-electron pair and the remaining goes into the kinetic energy that is shared by the pair [75][76] (Fig. 13).

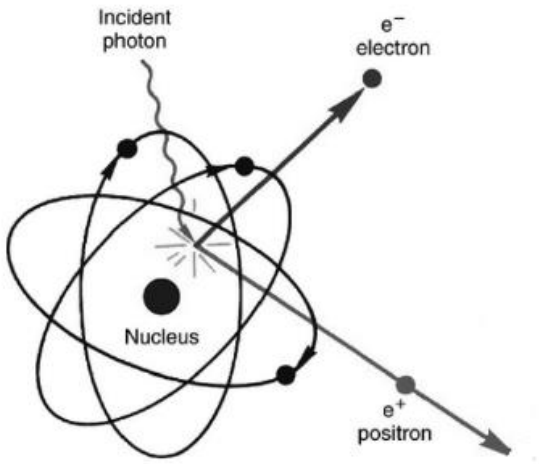

Figure 13: Schematic representation of Pair production effect [79].

Rayleigh scattering is a form of coherent scattering where the photon interacts with an electron bound by the electric field of the nucleus. This photon and electron interactions are elastic such as the photon loses no energy and it is scattered through a small angle. Rayleigh scattering is of little importance in nuclear medicine because it is not an effective process for transferring photon energy to matter.

These interactions are governed with photon cross sections of the travelled medium. They play an essential role in particle transport and relative absorbed dose simulation [75].

Given a photon at a definite location with given momentum and energy, the first step is to sample the free path lengths until the next interaction site. The probability distribution $f(s)$ of these path lengths is given by the exponential attenuation law:

$$f(s) = e^{(-\mu s)} \qquad (20)$$

with μ being the linear attenuation coefficient. The photon path lengths can be sampled from distribution using a uniformly distributed random number N_1 from interval [0,1] and the relation:

$$s = -\frac{1}{\mu} \ln(N_1) \qquad (21)$$

Using this path length, the photon can be tracked to the interaction site taking into account different materials with different attenuation coefficients μ in each voxel of the calculation grid. In the energy range of radiation therapy μ is calculated as a sum of three relevant contributions:

$$\mu = \mu_{photo} + \mu_{Compton} + \mu_{pair} \qquad (22)$$

with μ_{photo}, $\mu_{Compton}$, μ_{pair} being the linear interaction coefficients or total cross sections for photoelectric effect, Compton scatter and pair production, respectively. These parameters are different for photons of different energy. They also depend on the atomic composition of the material, i.e. they change from voxel to voxel.

A second random number N_2 from interval [0, μ] can be used to sample the interaction type. A photoelectric absorption is simulated if N_2 is less than μ_{photo}. A Compton interaction is performed if N_2 is larger than μ_{photo} but less than $\mu_{photo} + \mu_{Compton}$; otherwise a pair production process is programmed.

The parameters of secondary particles after the chosen interaction, such as energy and direction, can be sampled using further random numbers and the corresponding differential cross sections for that interaction type. The formulas of the probability distributions are more complex compared with the formulas above, but the sampling principle remains the same. Secondary particles are simulated like the primary ones, i.e. their transport starts with sampling the free path length to the next interaction site. The procedure continues as in the

case of primary particles. In each voxel the absorbed energy must be determined and accumulated. Later this leads to the dose distribution. The particle history ends if the photon leaves the calculation matrix or if its energy drops below a minimum energy [75][79].

2.6.2 Electron interaction processes

The simulation of electrons is fundamentally different from uncharged particles such as neutrons and photons that undergo few interactions with a relatively long mean-free path length compared to electrons that are affected by Coulomb forces that result in many interactions with matter. Additionally, electrons have little mass causing them to scatter more frequently at larger angles. Another issue is the approximate continuous energy loss of electrons. Although interactions are stochastic, electrons interact frequently and hence they can be approximated by a continuous interaction, except for large or catastrophic events.

Electron interactions can be broken into three categories: soft collisions, hard collisions and nuclear Coulomb field interactions. The kind of interaction that an electron will undergo depends on the relationship between the impact parameter *b* and the atomic radius *a*. The impact parameter is the perpendicular distance between the undisturbed electron path and the atomic nucleus before an interaction (Fig. 14).

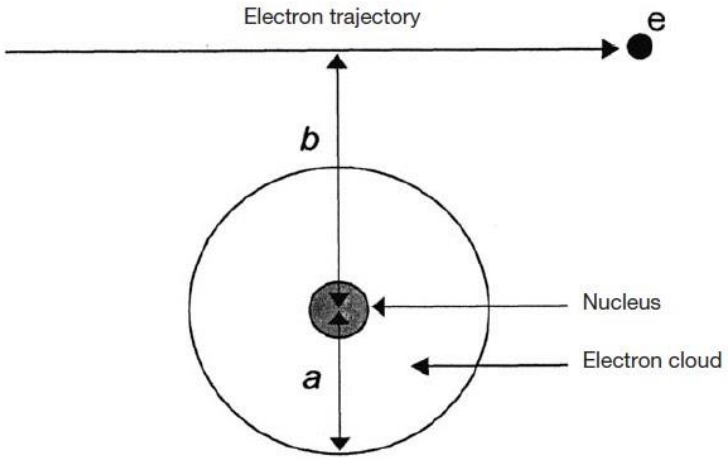

Figure 14: Interaction of an electron with an atom, where a is the atomic radius and b is the impact parameter [79].

Approximately 50% of an electron's energy loss is due to soft collisions. In each individual interaction, a small amount of energy is lost to the medium through excitation or ionization. The energy loss is typically of the order of a few eV. Soft collisions occur when the electron passes near an atom but not close with respect to the size of it, namely when $b >> a$.

Hard collisions occur when $b \sim a$. Hard collisions are considered to interact with an individual electron in the atom, which can liberate an electron from the atom. The secondary electron travels through the matter in the same fashion as the primary. In this kind of collisions, the inner shell electrons get ejected from the atom, leaving it in a state of excitation. The lower energy state is achieved by electrons in the outer shells falling into the vacation left by the liberated electron.

In the event that an electron comes close to the atomic nucleus ($b << a$), it will most likely undergo elastic scattering.

The most accurate way to model electron transport in a Monte Carlo simulation is by modeling each electron scattering event individually, not considering how small are and the time consumption. To speed up the calculation, most MC codes used a condensed history approach, treating many small interactions as one larger event [75][79].

Fig. 15 illustrates the difference between a single scattering and the condensed history technique.

The path for single scattering is not continuous as shown but it is still made of discrete events. There are many interactions with single scattering, and it would require a large amount of time. To approximate, the many small scattering events are grouped in large ones by using a multiple scattering theory. The large numbers of small interactions are elastic or semi-elastic and are approximated in the condensed history technique by a continuous energy loss along the electrons path. Then, this energy is deposited locally about the track [84].

There are three commonly used multiple-scattering theories for electrons developed: Molière [81], Goudsmit-Sanderson [82] and Lewis [83]. Each of the three, or variants of them, can be found in use today for MC simulations.

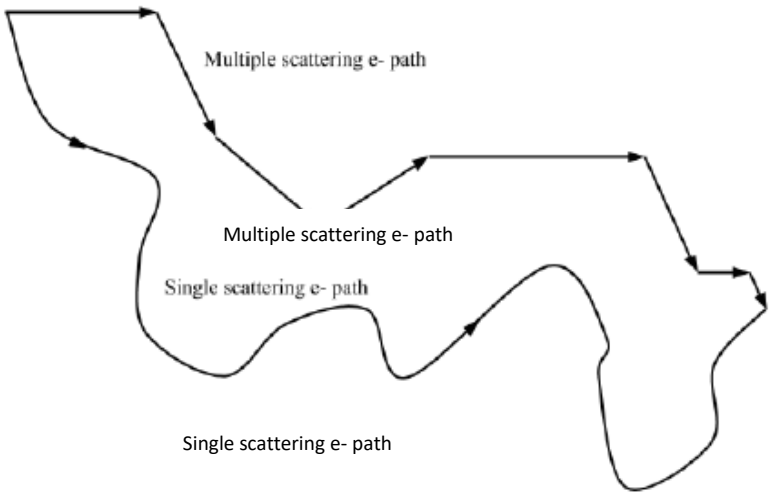

Figure 15: A sketch of the hypothetical paths of an electron using single scattering and a condensed history approach [84].

2.6.3 Monte Carlo methods

A number of different MC codes have been used in the simulation of radiotherapy treatments.

While the codes all share the same fundamental approach, they do not always provide the same results (stochastic variance withstanding). Differences in the cross-section databases referenced, the interpolation techniques applied, and the way geometries are handled can lead to variations in dose prediction. Investigations using multiple codes have shown that this disagreement can be as notable as 5%.

Noteworthy codes are: Monte Carlo N-Particle (MCNP), Electron Gamma Shower (EGS) and Geometry And Tracking (Geant4).

The MCNP code has a history that reaches back to the 1960s when the first version of the code was written at Los Alamos Laboratory. At that point the code was used mainly for 3D simulations of neutron transport. Then, MCNP added electron transport and as such its applicability has increased.

EGS was the first developed at the Stanford Linear Accelerator Center for simulation of high-energy electromagnetic cascades. At the outset it was almost exclusively used in high-energy accelerator project, even if improvements in low energy photon and electron transport changed this. Nowadays EGS has become the dominant code for medical physics

applications and some have referred to it as the de facto gold standard for clinical radiation dosimetry.

Geant4 is an open source C++ toolkit developed by CERN and designed to model particles passing through and interacting with matter. The purpose was to develop a general-purpose Monte Carlo code that is continuously supported by the research community. While the code is general purpose, the focus was on high energy particle physic rather than medical physics applications. Currently it has been applied to high energy physics, nuclear and accelerator physics, space science, and medical physics.

Geant4 has some advantages over other Monte Carlo codes previously mentioned. It has the ability to model all types of particles in a wide range of energies, down to eV range and up to TeV. Extensive research has shown Geant4 to be well validated for a wide range of particles and particle energies [87][88][89][90]. Geant4 has the most advanced geometry modeling allowing complex geometries to be used in the simulation and it is written with the object-oriented C++, whereas most other codes are written in FORTRAN. This further increases the usefulness of Geant4 to dosimetry applications of radiotherapy treatment simulations.

2.6.4 Geant4 Application for Tomographic Emission (GATE)

Geant4 Application for Tomographic Emission or GATE is a macro-structured software built from the Geant4 toolkit by the OpenGATE collaboration. The software is a community effort from researchers around the world ad is open-source where users are encouraged to offer suggestions and edit source-code to expand GATE's utility. The software was initially designed for nuclear medicine PET and SPECT imaging and has been validated for these applications but has also been extended to dosimetry. The goal was to develop a Monte Carlo tool for researchers in medicine that was as robust as Geant4 but easier to learn and use. Indeed, Geant4 is a toolkit in C++ where the user must write the application using the toolkit whereas GATE is a macro structured software with predefined commands [78].

The software inherits the robust capabilities of Geant4, notably well-validated physics models, geometry modeling tools, and visualization and three-dimensional rendering (Fig. 16). An important feature of GATE is the ability to model time-dependent events. Time-dependence is incorporated into all steps, including dynamic sources, source decays, and

geometry motion. The program uses a synchronized virtual clock to keep track of all time dependent events coherently.

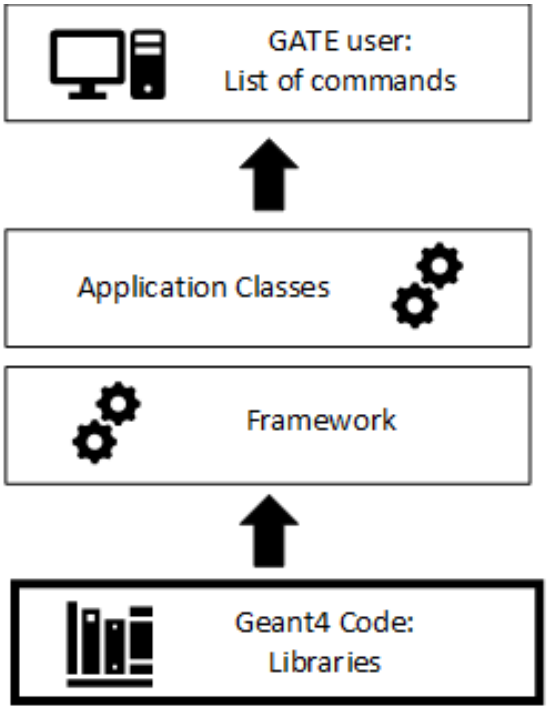

Figure 16: Structure of GATE

Most of the work done with GATE was with respect to PET and SPECT imaging until version 6 released in 2011. Before version 6 a study by Visvikis et al. [91] in 2006 investigates the use of GATE for dosimetry applications. They compared GATE to MCNPX2 and EGSnrc in two depth dose curves, from an 18 MV x-ray and 20 MeV electron beam incident on a slab of different thicknesses of water, aluminum, lung and water. They found the GATE results were in good agreement (~2.3%) with EGSnrc. Nevertheless, the GATE calculations had a slower computational time and had some deficiencies in the boundary crossing models and multiple scattering algorithms used in Geant4.

In 2008 Thiam et al [92] published their results evaluating the low-energy photon dose calculated by GATE (version 3.0.0). Looking at the results, they were in good agreement with other MC codes approximately in a range of 1 – 3.5%. Although these experiments were made with GATE versions preceding the version 6, as highlighted before, the results obtained in the dosimetry world were encouraging.

In version 6, new features were indeed added specifically for radiotherapy.

In 2011, Maigne et al. [94] compared electron dose calculations from GATE with results from EGSnrc and MCNP for energies between 15 keV and 20 MeV. The results showed that energies from 50 keV to 4 MeV had less than 3% difference between GATE and EGSnrc and MCNP and compared to EGSnrc all the differences for all the values of energy were under 4%. Hence, the authors concluded that GATE is well suited for calculating (electron) dose distributions for energies greater than 50 keV.

In 2012 Papadimitroulas et al. [95] developed a dose point kernel database for nuclear medicine applications using GATE. Dose point kernels were calculated with monoenergetic electron beams and various radioisotopes. GATE calculated values were compared to previously published results. Electron dose point kernels had a difference less than 5% for energies greater than 50 keV and approximately 6% for less than 50 keV. Beta radionuclides had a mean difference of 4% and photon values of 2%. On the basis of these results, these studies have shown that GATE is adequate for photon and electron dose calculations

Moreover, other studies carried out in the later years, involved in clinical settings, have demonstrated that GATE show good results with respect EGSnrc and MCNP also in the simulation of complex radiotherapy techniques [96][97][98][99].

Lastly, a review paper on GATE's capabilities, regarding radiotherapy and dosimetry, was published in 2015 by Sarrut et al. [86]. The paper highlights GATE's capabilities demonstrated by previous research and provides insights to the future of GATE for modeling radiotherapy systems and dosimetry studies.

While there is still room for improvement in GATE's features and accuracy (partly improved in the most recent version of the software), previous research has demonstrated that it is capable of accurately modeling radiotherapy dosimetry.

Many of the studies previously mentioned compare multiple MC codes with one another and often EGSnrc code is considered a gold standard due to its widespread use and validation in the medical physics field. Nevertheless, GATE within statistical uncertainty and parameters of the experiments is found to be in agreement for dosimetry modeling. A major advantage of GATE over the other codes is its robust geometry capabilities (built on Geant4), object-oriented language and a well-validated physics models for all particles. Moreover, GATE allows users to specify motion of all geometries in one simulation and synchronizing all

motion together. Another advantage is GATE's user-friendly macro structure makes it a more attractive simulation package to use.

On the basis of the studies carried out which have highlighted its advantages, validity and good applicability to radiotherapy, GATE was chosen as MC code in order to develop the project of this dissertation.

In this research, based on the SIRT treatment, GATE is used to develop a microscale model of the liver based on a simplification of the Functional Sub-Units (FSU), i.e. the hepatic lobule. Each FSU, as better described in the next chapter, is modeled as a hexagonal prism, with hepatic arterioles and central vein, respectively in each vertex and in the center.

Thanks to the simulations performed by GATE, the aim is to investigate the effect of radioactive microsphere distribution on the liver and its relative absorbed dose.

CHAPTER 2

Material and methods

This chapter will outline the materials and methods used for the development of the microscale model of the liver based on a simplification of the physiological hepatic lobule. An overview of the geometric parameters of the lobule model, the GATE simulation settings, and the methods to analyze the data output are presented.

1. Lobule geometry

As mentioned in chapter 1, the human liver consists of hexagon-shaped hepatic lobules arranged tightly next to each other like the structure of a honeycomb. Each hepatic lobule has a hepatic triad located at each corner of the lobule and consists of the portal artery, portal venule and the branch of bile duct. Based on this description, a liver model was developed. Specifically, the lobule dimensions proposed by Gulec et al.[6] have been chosen to build the model. The lobule height (*H*), the distance from the center to the side (*r*), and the distance from the center to the vertex (*d*) are 1500, 600, and 693 µm, respectively. These correspond to a lobular volume of 1.87 mm^3. The central vein was modeled as a pair of concentric cylinders 28 (*rc2*) and 33 (*rc1*) µm in radius and 1300 µm in length (*h*). Considering that the radioactive microspheres reach only the hepatic arteries and to simplify the geometric structure, the portal tracts were modeled as a unique hepatic artery made by a pair of concentric cylinders with a length of 1300 µm. The inner and outer radius of the hepatic artery were 15 (rh2) and 24 (*rh1*) µm, respectively (Table 2, Fig. 17).

Lobule components	Dimension (µm)
Lobule Height – H	1500
Lobule radius – r	600
Lobule distance center-vertex – d	693
Central vein outer radius – rc1	33
Central vein inner radius – rc2	28
Hepatic artery outer radius – rh1	24
Hepatic artery inner radius – rh2	15
Central vein / hepati artery height – h	1300

Table 2: Dimensions for each components of the lobule model.

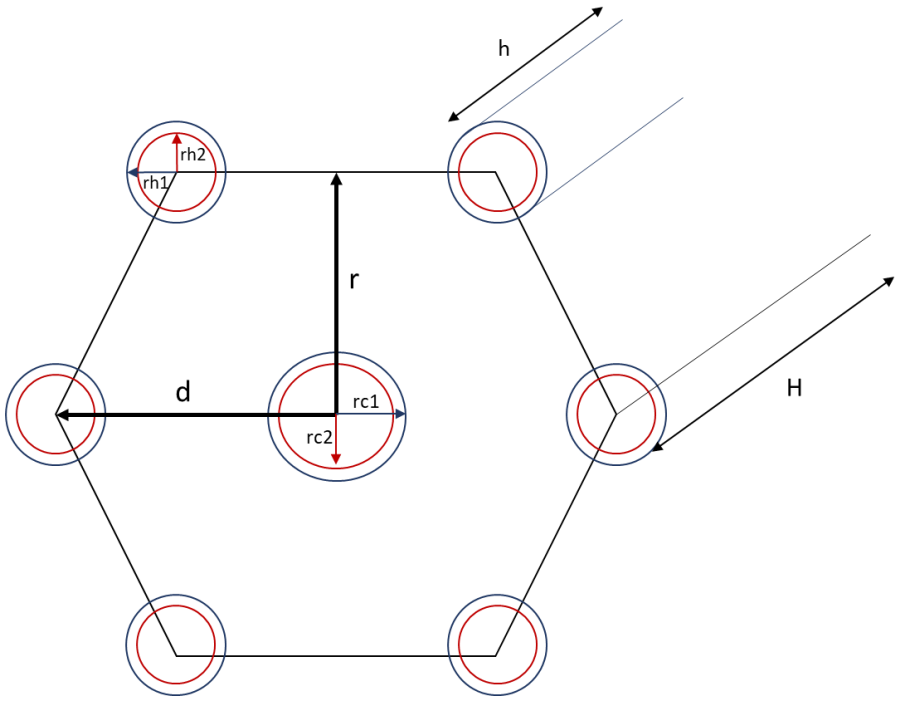

Figure 17: Schematic representation of the lobule model with its geometric parameters.

2. GATE

GATE is an advanced opensource software developed by the international OpenGATE collaboration and dedicated to numerical simulations in medical imaging and radiotherapy [103].

It uses an easy-to-learn macro mechanism to configurate simple or highly sophisticated experimental settings. It consists of several hundred C++ classes. The mechanisms used to manage time, geometry, and radioactive sources form a core layer of C++ classes close to the GEANT4 kernel (Fig. 18). An application layer allows for the implementation of user classes derived from the core layer classes, e.g. building specific geometrical volume shapes and/or specifying operations on these volumes like rotations or translations. Since the application layer implements all appropriate features, the use of GATE does not require C++ programming: a dedicated scripting mechanism that extends the native command interpreter of GEANT4 makes it possible to perform and to control Monte Carlo simulations of realistic setups.

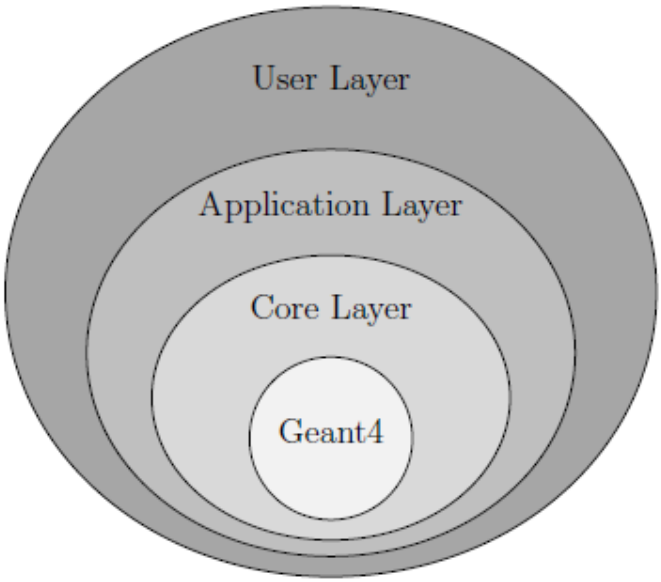

Figure 18: layer-structure of GATE [103].

The core layer represents base classes that explain the construction of geometry, the interaction physics, visualization and time management. The application layer extends on these base classes at the core layer to model specific objects or processes (for example the base class for volumes is at the core layer, where the application layer defines the specific volume types like a box or a sphere and how they can be translated). The user layer allows the running of the simulation in an interactive mode or by executing a macro script.

Macro scripts are ASCII text files (with .mac filename extensions) in which each line contains a GATE command or a comment. Macros can be executed directly in GATE by calling the macro in command-line window, from within another GATE macro or using the macro file as an argument of the GATE command line executable.

In the case of this work all GATE simulations were executed from the command-line, calling the specific macro file.

All commands and definition of components of the simulation are included in macro file and must be in a specific order. In order to create a simulation in GATE the user must define:

- The visualization component
- The environment in which to build the desired geometries, called *"world"*
- Geometries
- Physical processes
- Data outputs
- Sources
- Acquisition times

2.1 Set the visualization

The commands reported in Fig. 19 permit to visualize the geometry and the trajectories of the particles during the simulations [102].

```
#==============
#VISUALISATION
#==============

/vis/open OGLSQt
/vis/open OGLSX
/vis/viewer/set/viewpointThetaPhi 60 60
/vis/viewer/zoom 1.5
/vis/drawVolume
/vis/viewer/flush
/tracking/verbose 0
/tracking/storeTrajectory 1
/vis/scene/add/trajectories
/vis/scene/endOfEventAction accumulate 10
```

Figure 19: GATE visualization commands.

Specifically, the commands */vis/open OGLSQt* and */vis/open OGLSX* permit to set up two different viewers. With the former, it is possible to obtain an interactive viewer that allows to interact with the geometry and the results of the simulation (i.e. rotate the geometry, show the radioactive spheres, etc.). On the other hand, the latter set up a non-interactive viewer that shows only the geometry and the trajectories of the particles, without the possibilities to operate in it.

2.2 World definition

The world environment as described by GATE is a cubic box volume centered at the origin of the coordinate system. The world volume is the basic volume inside which all the other geometries have to be built and it is the only volume initially present in all GATE simulation A user can specify any size for the world volume, provided that it is sufficiently large to enclose all other volumes. The commands used to define the world are:

/gate/world/geometry/setXLength X mm (I)

/gate/world/geometry/setYLength Y mm (II)

/gate/world/geometry/setZLength Z mm (III)

/gate/world/setMaterial Name_Material (IV)

As suggested by the last commands, the world can be composed of any material. The material types are defined within the GATE material database. GATE material database is a text file still implemented in GATE software, including a list of different materials. Additional materials can also be constructed within GATE. This easily modifiable file contains all the data needed by GATE, such as elements and materials that are utilized to create the physical properties of different sorts of molecules, atoms and compounds.

Fig. 20 shows how the materials are characterized. They are described by specifying the density and the elements of the material by stoichiometric composition. In Fig. 20 the material "*Liver"* used in this work to define the lobule is shown.

```
Liver:  d=1.06 g/cm3 ; n=11
        +el: name=Hydrogen   ; f=0.102
        +el: name=Carbon     ; f=0.139
        +el: name=Nitrogen   ; f=0.03
        +el: name=Oxygen     ; f=0.716
        +el: name=Sodium     ; f=0.002
        +el: name=Phosphor   ; f=0.003
        +el: name=Sulfur     ; f=0.003
        +el: name=Chlorine   ; f=0.002
        +el: name=Potassium  ; f=0.003
        +el: name=Calcium    ; f=0.0
        +el: name=Scandium   ; f=0.0
```

Figure 20: Description of liver material in GATE database.

2.3 Geometry definition

GATE can produce volumes in several predefined shapes, such as boxes, cylinders, cones, trapezoids, etc., with some user parameters that depend on the shape. When a volume is created with GATE, it automatically appears in the GATE tree. All the commands applicable to the new volume are then available from this GATE tree. For instance, if the name of created volume is *Volume_Name*, all commands applicable to this volume start with the line:

/gate/Volume_Name/... /... / *(V)*

Any new volume must be created as the "daughter" of another volume (i.e. "*World"* volume or another volume previously created) and it is placed in the middle of its "mother volume" in reference to their origins.
In GATE, the creation of a new volume must follow three rules:

1. A volume which is located inside another must be its "daughter".
2. A "daughter" must be fully included in its "mother".
3. Volumes must not overlap.

To implement a new volume, the first step is to assign it a name and a "mother" using:

/gate/mother_Volume_Name/daughters/name Volume_Name *(VI)*

The creation of a new volume is completed when a shape to the new volume is assigned:

/gate/mother_Volume_Name/daughters/insert Volume_Shape *(VII)*

Then, it is necessary to set the size of the shape and its material (i.e. considering the lobule and hence a hexagonal volume, the parameters to set up are the radius and the height):

/gate/Volume_Name/geometry/setRadius X mm *(VIII)*
/gate/Volume_Name/geometry/setHeight Y mm *(IX)*

/gate/Volume_Name/setMaterial Name_Material *(X)*

With respect to the center of the axes in (0, 0, 0), it is possible to set the position of the geometry chosen:

/gate/Volume_Name/placement/setTranslation X Y Z mm *(XI)*

2.4 Physical processes setting

Once the volumes are described, the interaction processes of interest in the simulation must be specified.

GATE models several nuclear interactions during simulation. These interactions are considered physics models that the user must employ in the simulation study. Specifically, three models are available:

1. *Standard* processes are effective between 1keV and 100TeV.
2. *Low energy* processes are effective between 250eV and 100GeV.
3. *Penelope* processes are effective between 250 eV and 1GeV.

To add physical processes in the macro file, it is firstly necessary to enable the library in which they are contained in GATE, through the command:

/gate/physics/addPhysicsList emstandard_opt3 *(XII)*

Subsequently the user must add all the desired processes and their models:

/gate/physics/addProcess Name_Process *(XIII)*

/gate/physics/process/Name_Process/setModel StandardModel *(XIV)*
PenelopeModel

In this thesis, the principal interactions such as Photoelectric effect, Compton scattering, Rayleigh scattering, Pair production effect, Electron ionization, Bremsstrahlung, positron annihilation and the radioactive decay were set up.

The *Photoelectric effect* represents the absorption of a photon by an atomic electron with the ejection of this electron from the atom. Since a free electron cannot absorb a photon and conserve momentum, the photoelectric effect always occurs on bound electrons while the nucleus absorbs the recoil momentum.

The *Compton and Rayleigh processes* describe scattering forms. The former consists on the photon scattering by free electrons. The latter is a form of coherent scattering where the photon interacts with an electron bound by the electric field of the nucleus.

The *Pair production effect* (described in GATE under the term "*GammaConversion"*) characterizes the transformation of a photon into an electron-positron pair.

The *Electron ionization*models a charged particle passing through matter loses energy due to inelastic collision with atomic electrons of the material. Lost energy is transferred to the atom causing ionization or excitation.

The *Bremsstrahlung*is the production of an electromagnetic radiation by a charged particle accelerated in the field of another charged particles, such as nucleus.

The *Positron annihilation* simulates the in-flight annihilation of a positron with an atomic electron.

The *Radioactive decay*is the process in which an unstable atomic nucleus spontaneously loses energy by emitting ionizing particles and radiation.

2.5 Output setting

To output data in GATE, *"dose actors"* need to be defined. GATE uses the concept of an *"actor"* to store information from a simulation. The actors are tools which allow to interact with the simulation, and they can collect information during the simulation, such as energy deposit, number of particles created in a given volume, etc. An actor is assigned to a volume and that volume's daughter inherit the actor as well.

The actor required for the analysis of the dose distribution and hence the one used in this project is the so called *"DoseActor".*

To add the actor in the macro file, the general command is:

/gate/actor/addActor DoseActor Name_DoseActor *(XV)*

The following commands are:

/gate/actor/dosimetry/save Name_outputfile.fileextension *(XVI)*

/gate/actor/dosimetry/attachTo Name_Volume *(XVII)*

The first command allows to save the data of the actor to the file *Name_outputfile.* The specific properties (format, etc.) depends on the type of the actor.

The second command tells that the actor is attached to the volume *Name_Volume*. For track and step levels, the actor is activated for step inside the volume and for tracks created in the volume.

The *DoseActor* scores the energy deposited per voxel in a volume in the simulation. This energy is converted into dose depending on the material properties. It outputs indeed 3D dose map in units of Gy and energy deposited in units of MeV. The information from the *DoseActor* can be stored in several file formats. The dose can be outputted as an ASCII file (.txt), root file (.root), Analyze (.img) and MetaImage (.mhd, .raw).

The file format chosen in this application is the ASCII file. In this context, the *DoseActor* built a 3D matrix, composed by a set of 2D matrices representing the dose distribution for each slice in which the geometry is divided. The voxel size (single element of each matrix) and the number of slices is defined by the user.

Subsequently, in order to read it, the file was analyzed with MATLAB.

2.6 Source(s) definition

The sources used in these simulations are spheres with radius of 0.015 mm, charged by Yttrium-90. In fact, the goal is to represent the Theraspheres®, used in the SIRT treatment.

In GATE the best way to define a radiotracer source is through a method called Isotope source. Each source is firstly described by a name, a shape and its radius. The general commands used are:

/gate/source/addSource Name_Source *(XVIII)*

/gate/source/Name_Source/gps/type Volume *(XIX)*

/gate/source/Name_Source/gps/shape Sphere *(XX)*

/gate/source/Name_Source/gps/radius X mm *(XXI)*

Furthermore, the method can depict any radiotracer by characterizing its attributes such as the type of source (ion), the atomic number (Z), the atomic weight (A), the ionic charge (Q), the excitation energy (E), the initial activity, the emission angle and the half-life. This method is the slowest yet is the most realistic approach.

The values used for ^{90}Y in Theraspheres® are summarized in Table 3.

Element characteristic	**Value**
Type of source	Ion
Atomic Number (Z)	39
Atomic weight (A)	90
Ionic charge (Q)	0
Excitation energy (keV) (E)	0
Initial activity (Bq)	2500
Emission angle	Iso
Half-life (hours)	64.2

Table 3: ^{90}Y characteristics used in order to implement it as a source in GATE.

The necessary commands are:

/gate/source/Name_Source/gps/particle ion *(XXII)*

/gate/source/Name_Source/gps/ion Z A Q E *(XXIII)*

/gate/source/Name_Source/setForcedHalflife X s *(XIV)*

/gate/source/Name_Source/gps/energytype Mono *(XV)*

/gate/source/Name_Source/gps/monoenergy 0. MeV *(XVI)*

/gate/source/Name_Source/setActivity Y Bq *(XVII)*

The final step of the GATE set up is the definition of the beginning and the end of the acquisition. The commands *setTimeStart*, *setTimeStop* and *setTimeSlice* are used to define the number of runs to make and the duration.

For all the simulations, one second of dose collection was performed. To reduce long simulation run time a scaling of the output data was applied.

3. MATLAB script

The setting of the simulation in GATE consists in the definition of simple lines of commands without any C++ programming.

Nevertheless, to simulate a large number of lobules, the user must manually define for every single lobule and its components (central vein and arterioles) all the commands necessary to build again the geometry.

A MATLAB code was developed which allows to automatically obtain the file for GATE. Given the size of the desired lobule area, in terms of number of columns and lines of lobule, it output all the command lines for the definition of lobule geometry, including the hepatic artery and the central vein. Moreover, it prints also the code lines for the sphere definition and placements, with the possibility to choose their spatial configurations inside the lobule area.

4. Simulation settings

In order to calculate the absorbed dose and to evaluate the effect of the ^{90}Y microsphere distribution, different configurations based on two different architecture were performed.

1. Firstly, simulations using a single lobule (SL) geometry were carried out with different configurations of the radioactive spheres

2. Secondly, simulation based on multi-lobule (ML) architecture were led, on healthy and tumoral tumor tissue, given uniform or non-uniform radioactive sphere distribution.

4.1 Single lobule simulations

The lobule geometry and structure are represented in Fig. 21 and Fig. 22.

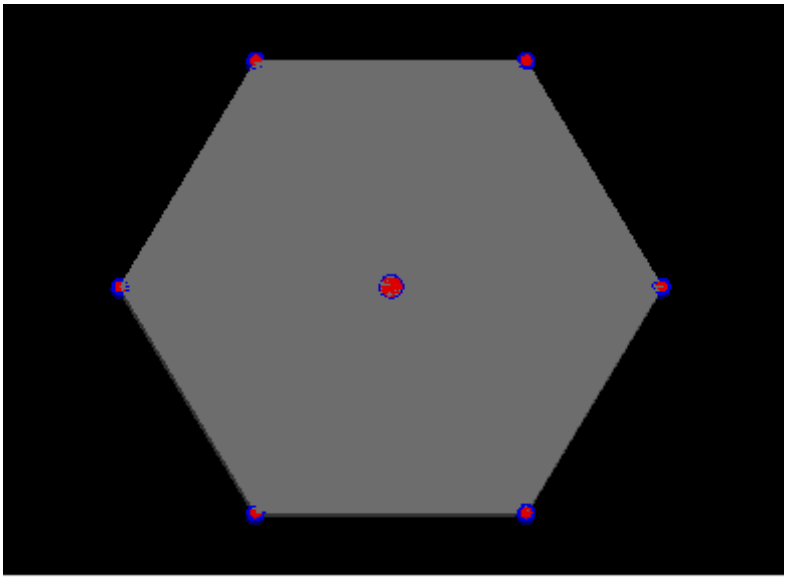

Figure 21: Front view of lobule model created in GATE.

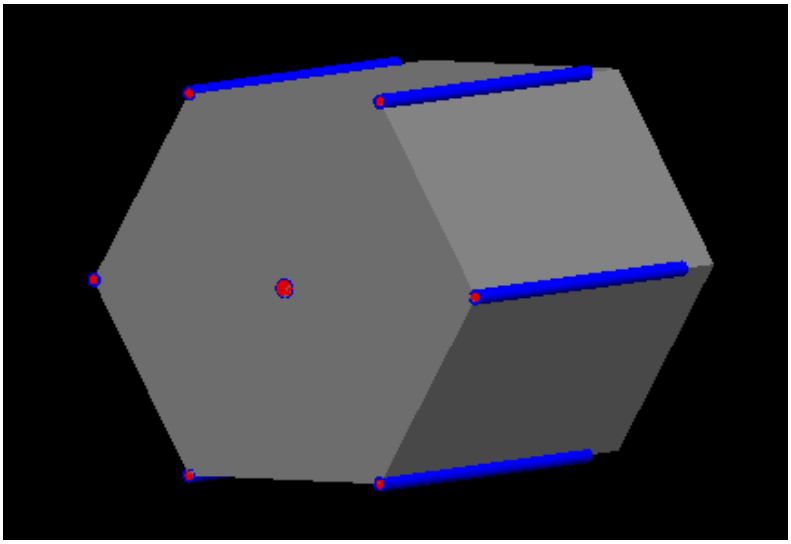

Figure 22: Prospective view of lobule model created in GATE.

To evaluate the different effects of uniform and non-uniform spheres deposition and the relation between the administered and absorbed dose, different microspheres distributions were simulated:

- one radioactive source is placed in the middle of each hepatic arterioles (SL-UNIF) (Fig. 23). Each source was placed in the middle of each hepatic arteriola.and has an activity of 2500Bq (activity of the glass spheres), therefore the total administered activity is 15000 Bq.

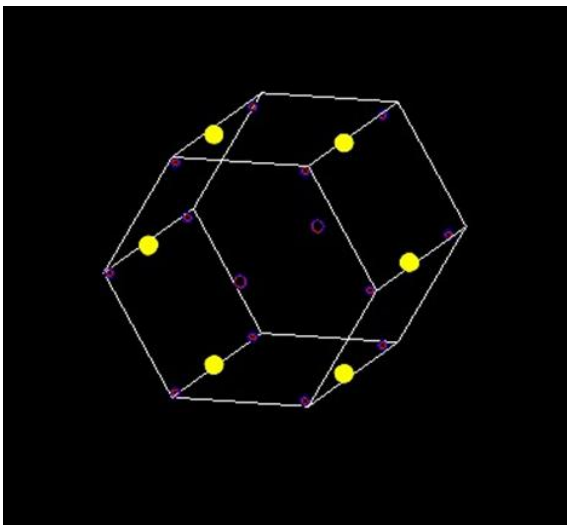

Figure 23: SL-UNIF sphere configuration. Each source is placed in the middle of each hepatic arteriole.

- three equidistant radioactive sources are placed in three hepatic arterioles (SL-3M) (Fig. 24). Every source is equidistant from the other and uniformly spaced along the arteriole's length. With this source configuration the initial activity administered to the lobule is 22500Bq, corresponding to nine sources with an activity of 2500Bq each.

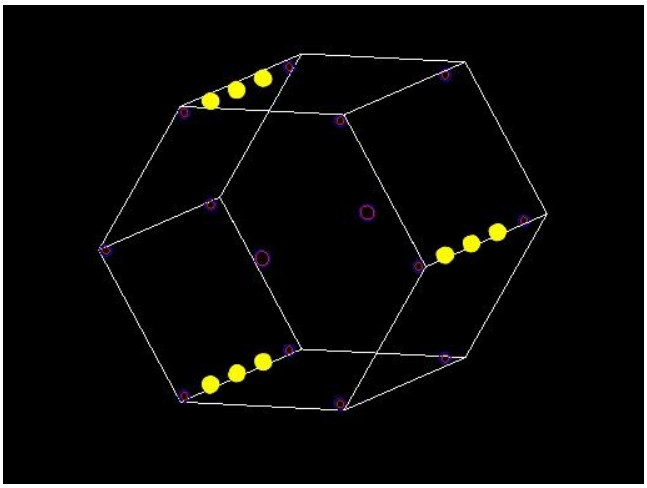

Figure 24: SL-3M sphere configuration. Three equidistant radioactive sources are place in three hepatic arterioles.

- five equidistant radioactive sources are placed in two hepatic arterioles on the opposite sides of the same lobule (SL-5M) (Fig. 25). With this source configuration the initial activity administered to the lobule is 25000 Bq, corresponding to ten sources with an activity of 2500Bq each.

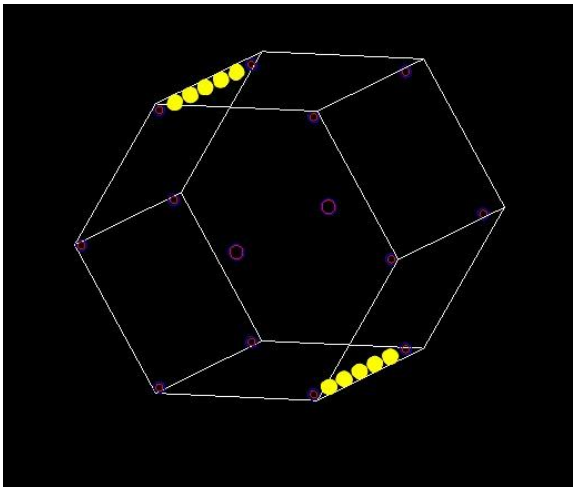

Figure 25: SL-5M sphere configuration. Five equidistant radioactive sources are placed in two hepatic arterioles.

For each simulation, the total value of absorbed dose inside the lobule is computed. as the sum of all the values of the absorbed dose for voxel averaged over the total number of voxels which constitute the lobule.

4.2 Single tumoral lobule simulation

Using the same geometry of the SL-UNIF simulation, a tumoral lobule was simulated. As in reality the tumor has a higher density with respect to the healthy tissue and lacking in literature stoichiometric data on the HCC, the tumoral lobule was modelled by changing its material density. .

Specifically, another material called “Liver2” was defined (Fig 26) with the same characteristic as the “Liver” material but with an increased density [g/cm^3] in order to simulate the different absorption of radiation in the two materials [116][117].

```
Liver:  d=1.06 g/cm3 ; n=11
        +el: name=Hydrogen   ; f=0.102
        +el: name=Carbon     ; f=0.139
        +el: name=Nitrogen   ; f=0.03
        +el: name=Oxygen     ; f=0.716
        +el: name=Sodium     ; f=0.002
        +el: name=Phosphor   ; f=0.003
        +el: name=Sulfur     ; f=0.003
        +el: name=Chlorine   ; f=0.002
        +el: name=Potassium  ; f=0.003
        +el: name=Calcium    ; f=0.0
        +el: name=Scandium   ; f=0.0


Liver2:  d=1.40 g/cm3 ; n=11
        +el: name=Hydrogen   ; f=0.102
        +el: name=Carbon     ; f=0.139
        +el: name=Nitrogen   ; f=0.03
        +el: name=Oxygen     ; f=0.716
        +el: name=Sodium     ; f=0.002
        +el: name=Phosphor   ; f=0.003
        +el: name=Sulfur     ; f=0.003
        +el: name=Chlorine   ; f=0.002
        +el: name=Potassium  ; f=0.003
        +el: name=Calcium    ; f=0.0
        +el: name=Scandium   ; f=0.0
```

Figure 26: Description of the material implemented in the simulation, as well as described in GATE

4.3 Multi-lobule simulations

The ML simulations were performed on a total of 289 hepatic lobule, that corresponds to a surface of 3,5 cm x 1,0 cm and to a total volume of 538,4 mm^3.

Four different scenarios were simulated:

- one radioactive source is placed in the middle of each hepatic arterioles of every single lobule (ML-UNIF) (Fig. 27). The number of sources set is equal to 631, that corresponds of a total administered activity of 15775000 Bq.

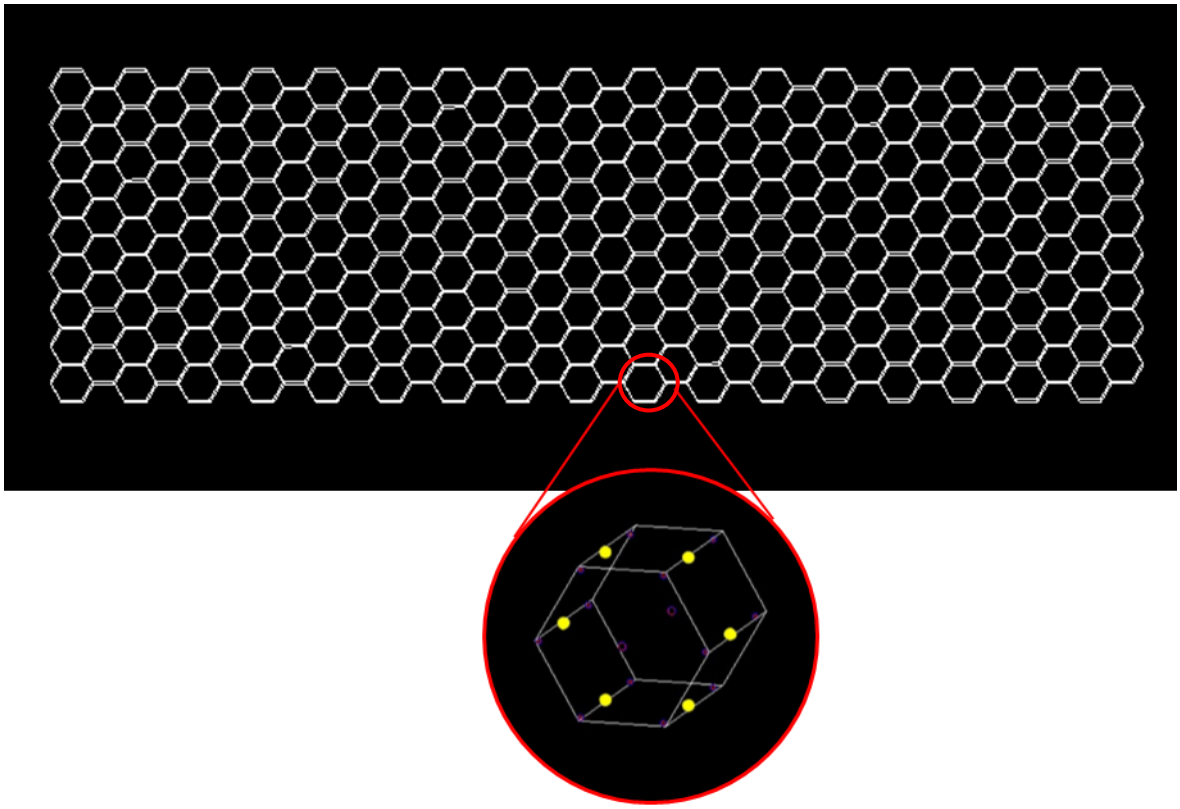

Figure 27: ML-UNIF, schematic representation of the 289 lobules obtained with GATE code. One radioactive source is placed in the middle of each hepatic arterioles of every single lobule.

- one radioactive source is placed in the middle of each hepatic arterioles of 81 lobules, located in the upper right corner (ML-NOUNIF) (Fig. 28, red area). The number of sources set is equal to 201, that corresponds of a total administered activity of 517500 Bq.

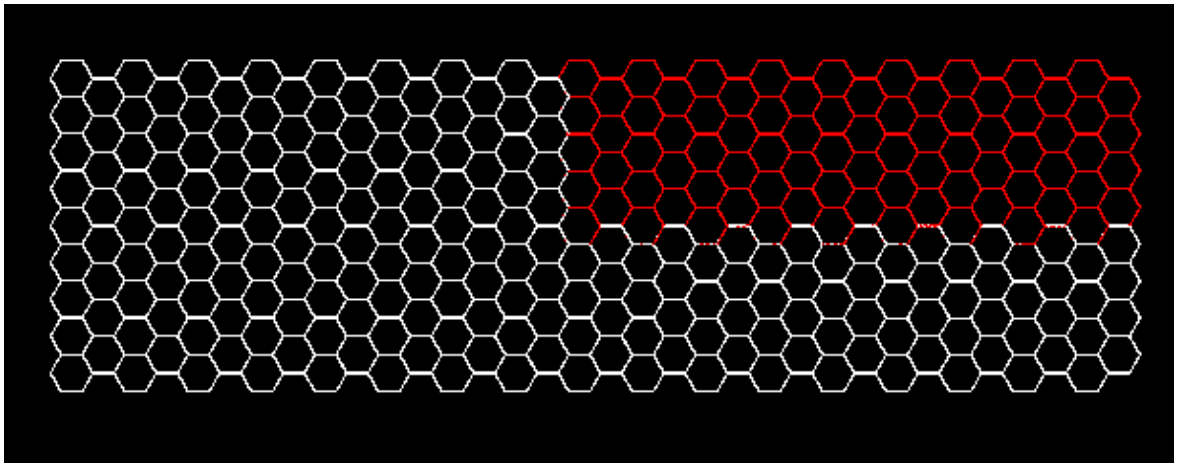

Figure 28: ML-NOUNIF, schematic representation of the 289 lobules obtained with GATE code. The red part shows the 81 lobules in which the spheres were placed.

- One radioactive source is placed in the middle of each hepatic arterioles of 81 tumoral lobules and of 9 healthy lobules adjacent to the pathological ones (ML-MIX 1) (Fig. 29). The number of sources set is equal to 229, that corresponds of a total administered activity of 572500 Bq.

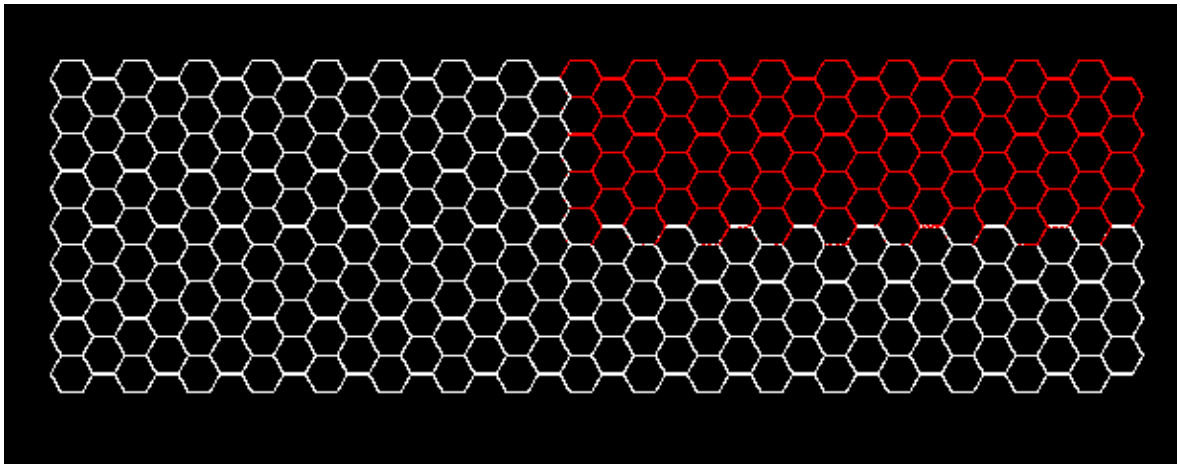

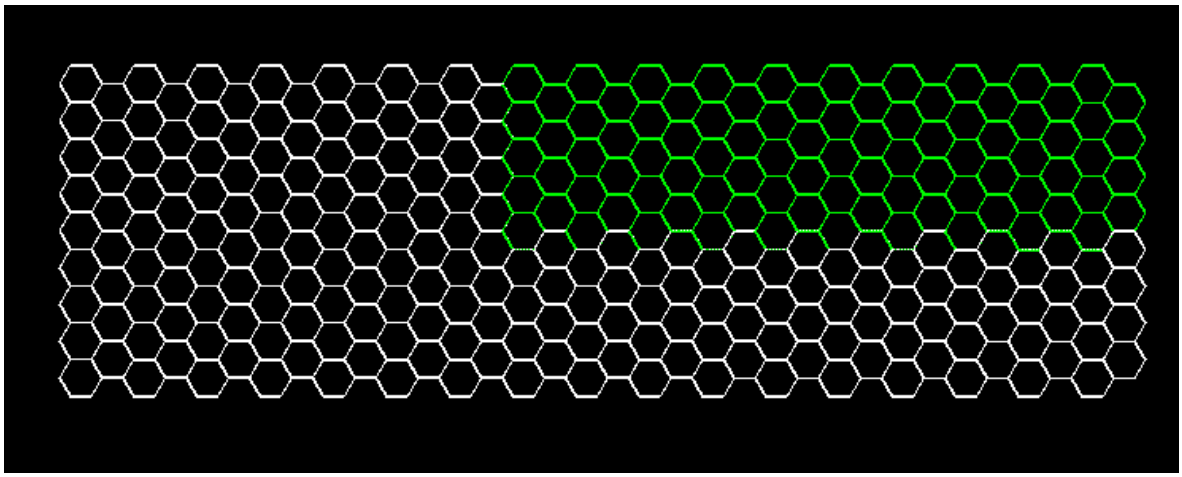

Figure 29: ML-MIX 1, schematic representation of the 81 tumoral lobules (red part) (top); Schematic representation of the area in which were placed the sources (green area: 81 tumoral lobules + 9 healthy lobules) (bottom).

- one radioactive source is placed in the middle of each hepatic arterioles of 81 healthy lobules and of 9 tumoral lobules adjacent to the normal ones (ML-MIX 2) (Fig. 30). The number of sources set is equal to 229, that corresponds of a total administered activity of 572500 Bq.

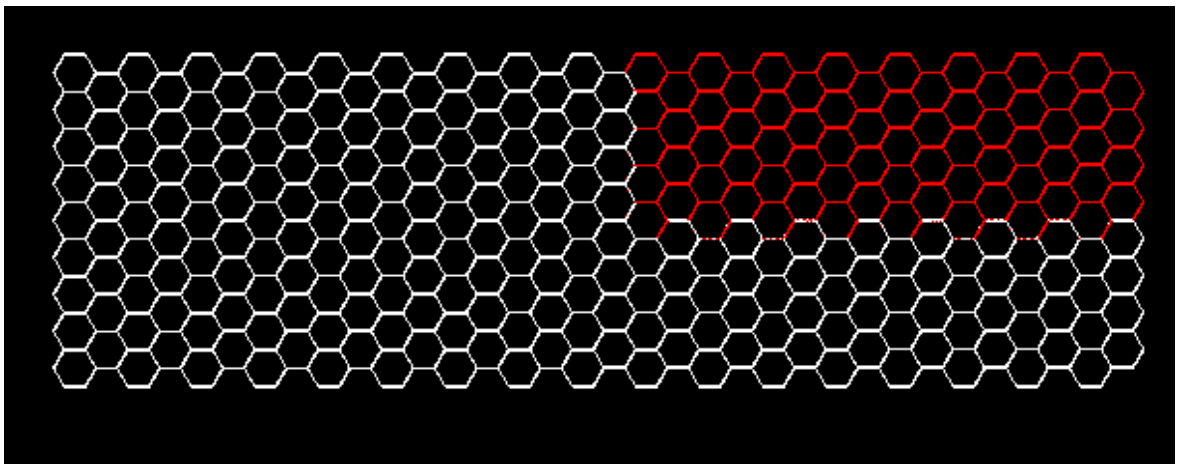

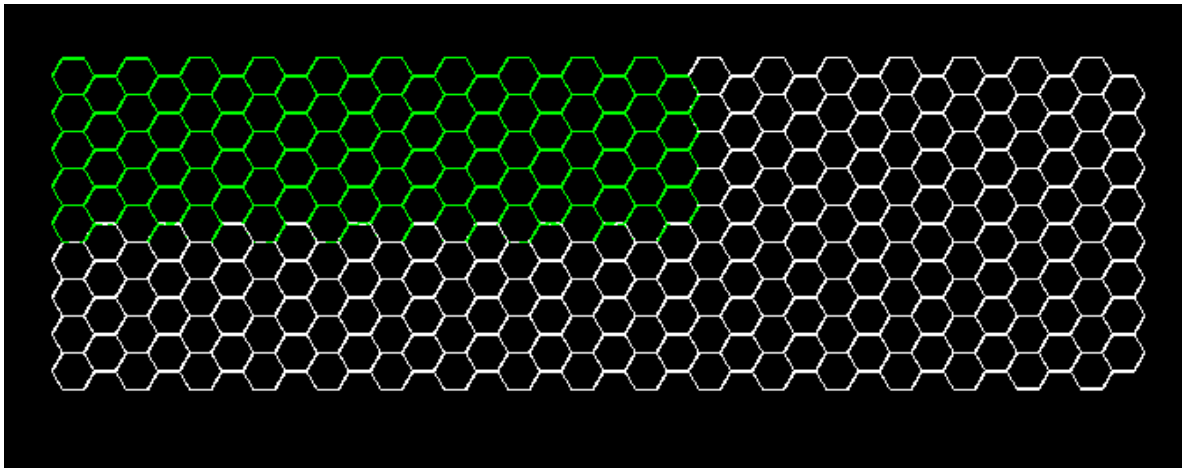

Figure 30: ML-MIX 2, schematic representation of the 81 tumoral lobules (red part) (top); Schematic representation of the area in which were placed the sources (green area: 81 healthy lobules + 9 tumoral lobules) (bottom).

5. Output analysis

After the GATE simulation has been executed for a short period of time (1s), a dose map file was generated.

The dose map file was composed by a 3D matrix. As schematized by the Fig. 31, each matrix represents the correspondent slice in which the volume was divided. Each element of the matrices shows the value of dose (d_i) per voxel.

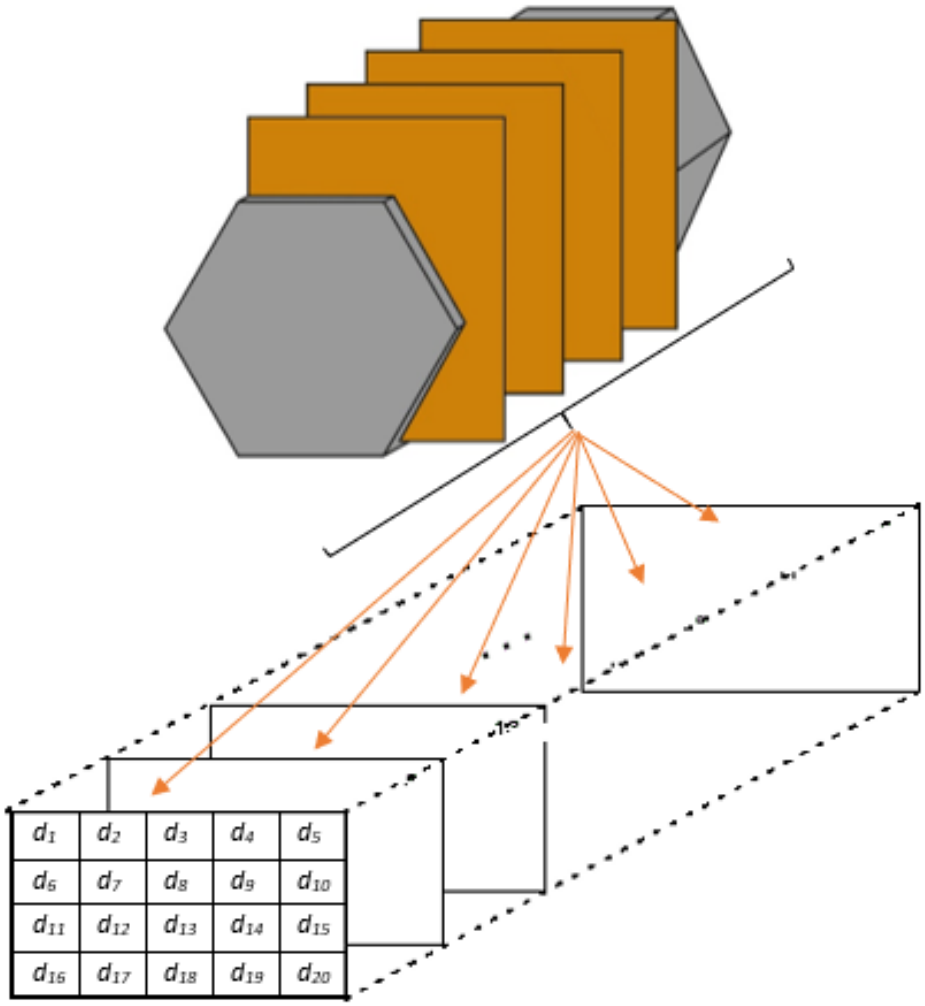

Figure 31: Schematic representation of the 3D matrix output by GATE. Each matrix represents the correspondent slice in which the volume was divided

The initial average absorbed dose (D_0) over the entire volume of interest for that period of time was computed by using:

$$D_0 = \frac{\sum_{i=1}^{N} d_i}{N} \qquad (23)$$

where d_i is dose per voxel and N is the total number of voxels.

Subsequently , the calculation of the total absorbed dose for all time (t = ∞) was performed as follows:

$$D(\infty) = \int_0^{\infty} D_0 \; e^{-\frac{t}{\tau}} \, dt \qquad (24)$$

$$\downarrow$$

$$D(\infty) = D_0 \tau \qquad (25)$$

$$\tau = \frac{t}{\ln(2)} \qquad (26)$$

Where τ is the decay constant and *t* is the half-life of the ^{90}Y [103].

In other words, a short time period was considered in which an initial dose per unit time was obtained, then it was analytically integrated over time from zero to infinity with an exponential decay corresponding just to the physical half-life of the isotope.

All these steps were carried out in MATLAB. Through few simple lines of commands, the program was able to import the ASCII file, read each single matrix of it, sum all the dose values and apply the time scaling procedure.

Moreover, MATLAB has facilitated extensions to visualize matrix as color map. As reported in the next chapter, these capabilities of the software have been exploited to achieve colored dose distribution map for each slice, to qualitatively value the dose trend in the volume.

CHAPTER 3

Results and discussion

In the following paragraph the results obtained from the SL and ML simulations are shown in terms in terms of colormaps of the absorbed dose and dose distribution trend in every slice of the hexagon. Moreover, a comparison between the initial administered activity and the final absorbed dose is investigated

1. Single lobule simulations

1.1 Single lobule, SL-UNIF: one radioactive source in the middle of the hepatic arterioles.

The color map of the dose at the central slice (Fig 32, top) and the subsequent slice (Fig. 32, bottom) are reported.
The central slice corresponds to the position in which the sources are placed inside the arteriole and each source is clearly visible in each vertex of the lobule. Moving from the central slice is possible to see the diffusion of the radioactivity from the sources to the inner lobule region.

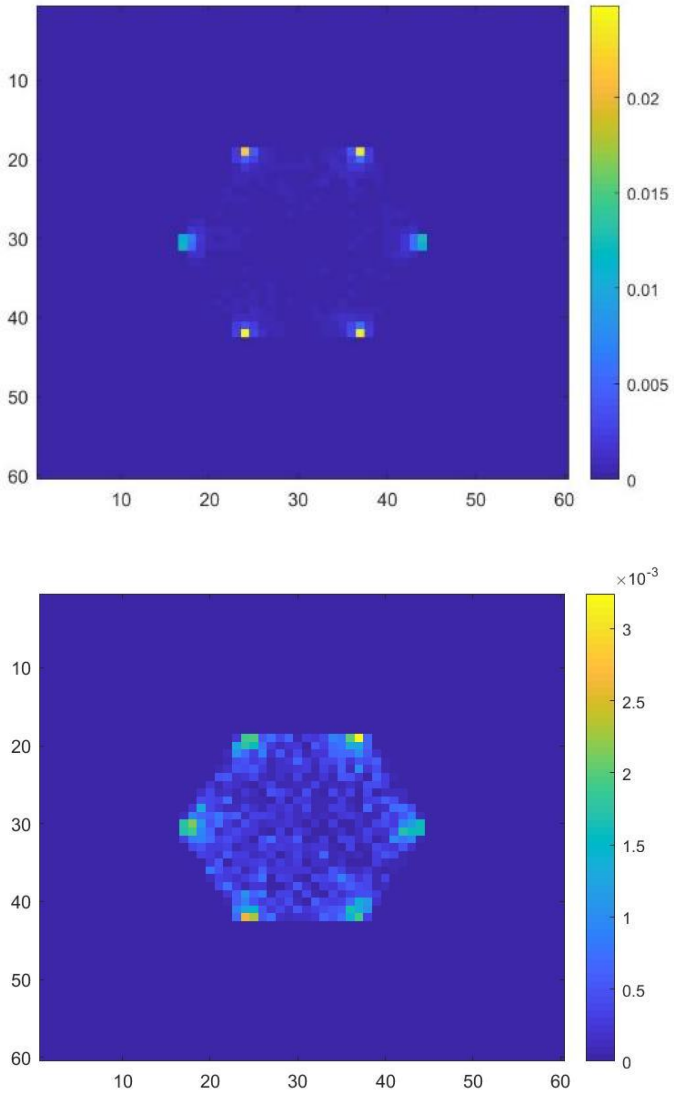

Figure 32: Colormap of the dose distribution in the simulation UNIF: the central slice of the lobule (top), and the subsequent slice (bottom) showing the spread of the radiation from the sphere (point with higher value on each corner) to the center of the lobule

Moving from the center of the lobule the radiation start to spread isotropically on each side of the source. With the uniform distribution each source in the vertex contributes to increase the absorbed dose in the inner part of the lobule in a symmetric way. The absorbed dose decreases also going further in the z direction from the source, as highlighted from the dose distribution graph in Fig (33).

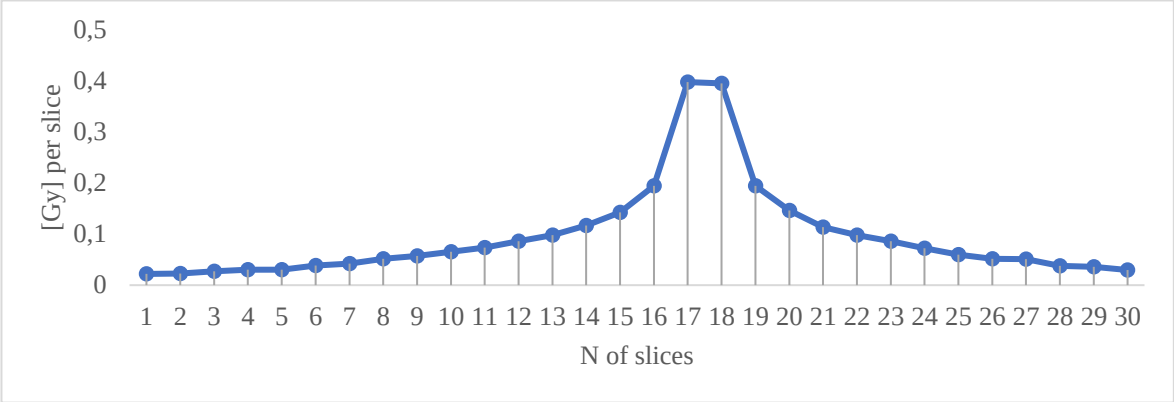

Figure 33: Dose distribution trend through the slices in UNIF simulation. 0 refers to the first frontal slice while 30 to the last slice

Specifically, the values reported for each slice are the sum of the absorbed dose computed on each voxel in the correspondent slice.
It is possible to notice the symmetric distribution of the absorbed dose, starting from the source (central slice) with the maximum values and decreasing symmetrically on both sides. The little asymmetry in the first part of the graph is explained due to the fact that the lobule has a length of 1,5mm while the hepatic arteriole of just 1,3 mm. The sources are placed in the center of the arteriole, so considering the entire lobule the position of the source is shifted of 1 mm with respect to the lobule center in the z coordinate.

	UNIF simulation	**Gulec et al. [6]**
Initial Activity [kBq]	15	15
Absorbed Dose [Gy]	64.02	64

Table 4: Comparison between the obtained total absorbed dose in UNIF simulation and the results in the literature.

The comparison of the simulation performed through GATE and those provided by Gulec et al. [6] reached through the MCNP software is summarized in table 4, highlighting a good agreement of the two.

1.2 Single lobule, simulation SL-3M: three equidistant radioactive sources in three hepatic arterioles

The output colormaps of the dose at the central slice and the subsequent slice of the SL-3M configuration are reported in Fig. 34.

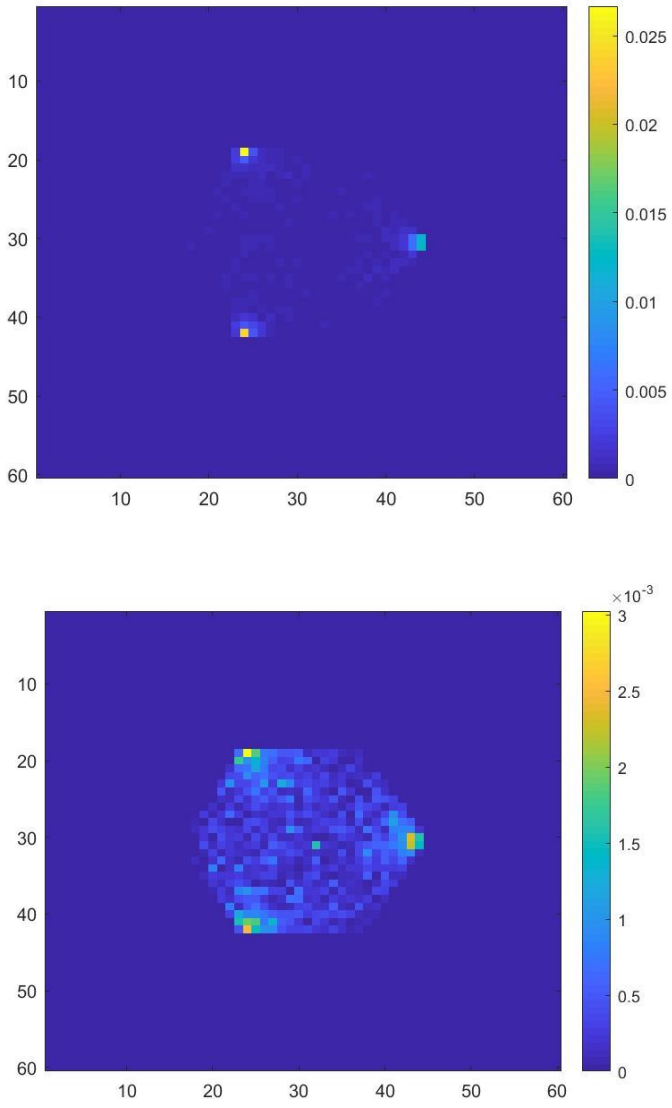

Figure 34: Colormap of the dose distribution for the SL-3M configuration: the central slice of the lobule (top), 3 point with a higher value can be seen, corresponding to the arteriole in which the spheres where placed. The subsequent slice (bottom) from which the distribution of radiation is visible.

The SL-3M case simulates a non-uniform distribution of sources inside the lobule, placing three sources in three arterioles. This results in a higher concentrated absorbed dose in the correspondent arteriole and in an ununiform spread of radiation. The center part of the lobule will receive the radiation just from three vertexes and, due to the placement of the three spheres uniformly spaced along the z axis, the radiation is higher also in the terminal and initial part of the lobule along the z direction. This is highlighted from the analysis of the absorbed dose distribution with respect to each slice in figure 35:

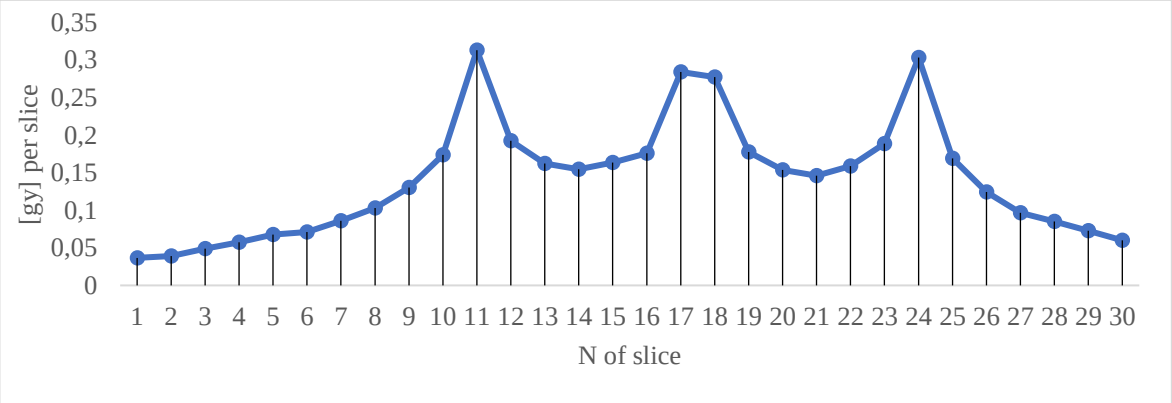

Figure 35: Dose distribution trend through the slices in Simulation 3M. The three peaks correspond to the three spheres placed along the z direction inside the lobule arteries. 0 corresponds to the first frontal slice while 30 to the last slice.

From Fig. 35 it is possible to notice the three peaks corresponding to the three sources inside the hepatic arteriole. Also in this case the symmetry expected of the distribution of the dose inside the lobule is respected. The peak representing the central sphere is lower respect to the other two due to the fact that the sphere is placed between two different slices and when outputted the value is divided in two different slices to.

1.3 Single lobule, simulation SL-5M: five equidistant radioactive sources in two hepatic arterioles

The color map of the dose at the central slice and the subsequent slice are reported for the central slide (Fig 36, top) and the subsequent one (Fig. 36, bottom). The central slice corresponds to the position in which the sources are placed inside the arteriole and each source is clearly visible in each vertex of the lobule. Moving from the central slice is possible to see the diffusion of the radioactivity from the sources to the inner lobule region.

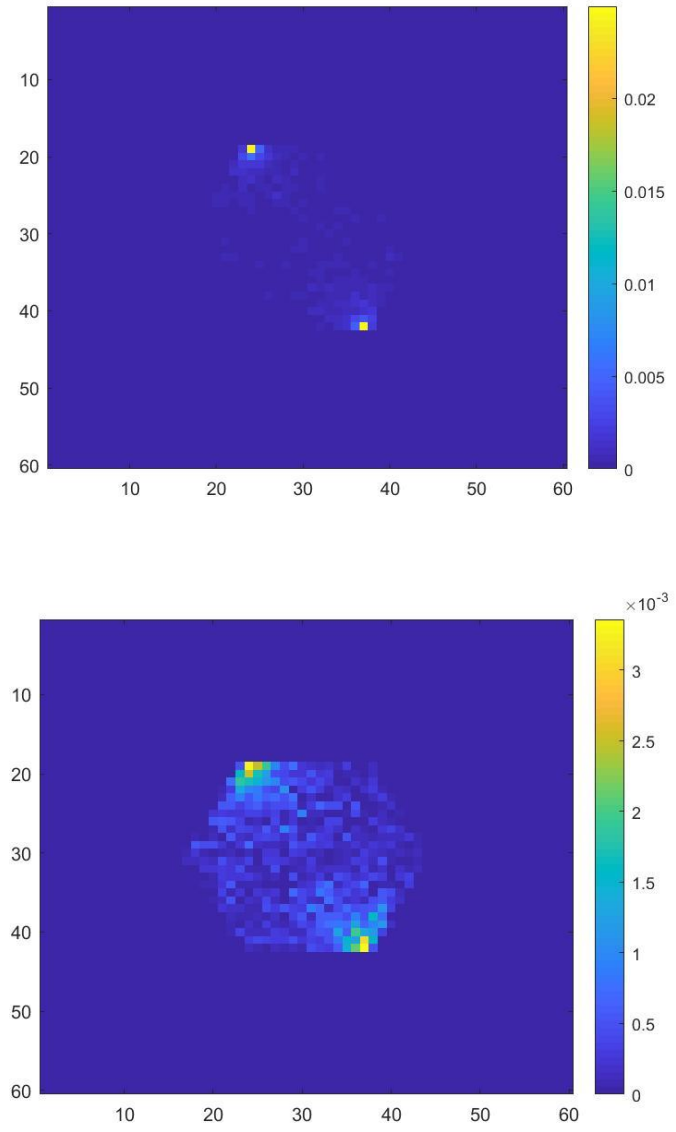

Figure 36: colormaps for the 5M configuration: the central slice (top) where 2 point with a higher value can be seen, corresponding to the arteriole in which the spheres where placed, the subsequent slice (bottom) from which the distribution of radiation is visible.

The 5M case simulates a non-uniform distribution of sources inside the lobule, placing five sources in two arterioles. This results in a higher concentrated absorbed dose in the correspondent arteriole and in an ununiform spread of radiation toward the center of the lobule. The center part of the lobule will receive the radiation just from two point and due to the placement of the five spheres uniformly spaced along the z axis, the radiation is higher also all along the lobule depth in the z direction. This is highlighted from the analysis of the absorbed dose distribution with respect to each slice in figure 37.

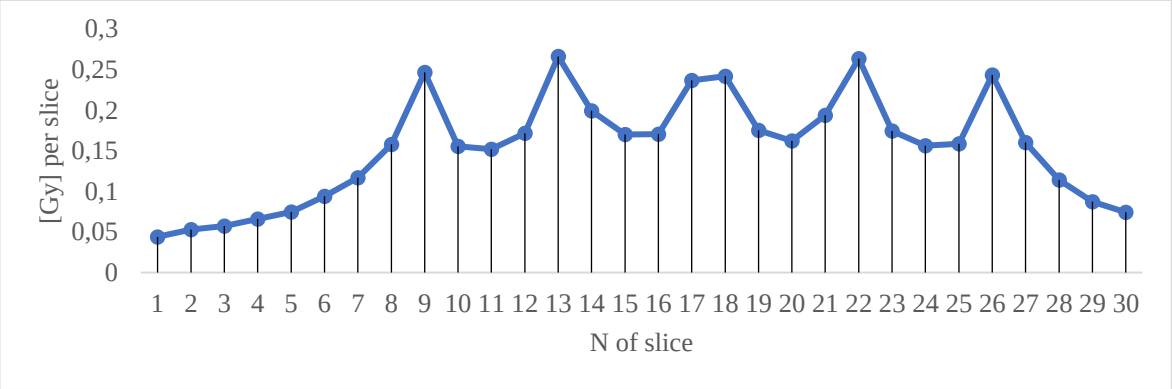

Figure 37: Dose distribution trend through the slices in Simulation 5M. The five peaks correspond to the five spheres placed along the z direction inside the lobule arteries. 0 corresponds to the first frontal slice while 30 to the last slice.

The presence of the five sources is highlighted by the five peaks. Also in this case the symmetry of the dose distribution is respected, with the little asymmetry at the beginning of the slice for the different length of the arterioles respect to the entire lobule. As the value of the third peak is divided into two different slices, it results lower respect to the other peak.

Finally, the values obtained with the three different configurations are compared to evaluate the relation between the administered dose and the absorbed dose (Table 5):

Single Lobule Simulations	**SL-UNIF simulation**	**SL-3M simulation**	**SL-5M simulation**
Initial Activity [kBq]	15	22,5	25
Absorbed Dose [Gy]	64,02	95,46	103,61

Table 5: Comparison between the different obtained total absorbed doses for each simulation.

As expected, the absorbed dose increases with increasing of the initial activity. Specifically, the simulations executed show a constant and linear ratio between the final absorbed dose (D_∞) and the relative initial activity (A_0) (Fig. 38):

- SL-UNIF: $A_0 = 15000\ Bq$ $D_\infty = 64.02\ Gy$ $\frac{D_\infty}{A_0} = 0.00426$
- SL-3M: $A_0 = 22500\ Bq$ $D_\infty = 95.46\ Gy$ $\frac{D_\infty}{A_0} = 0.00424$
- SL-5M: $A_0 = 25000\ Bq$ $D_\infty = 103.61\ Gy$ $\frac{D_\infty}{A_0} = 0.00414$

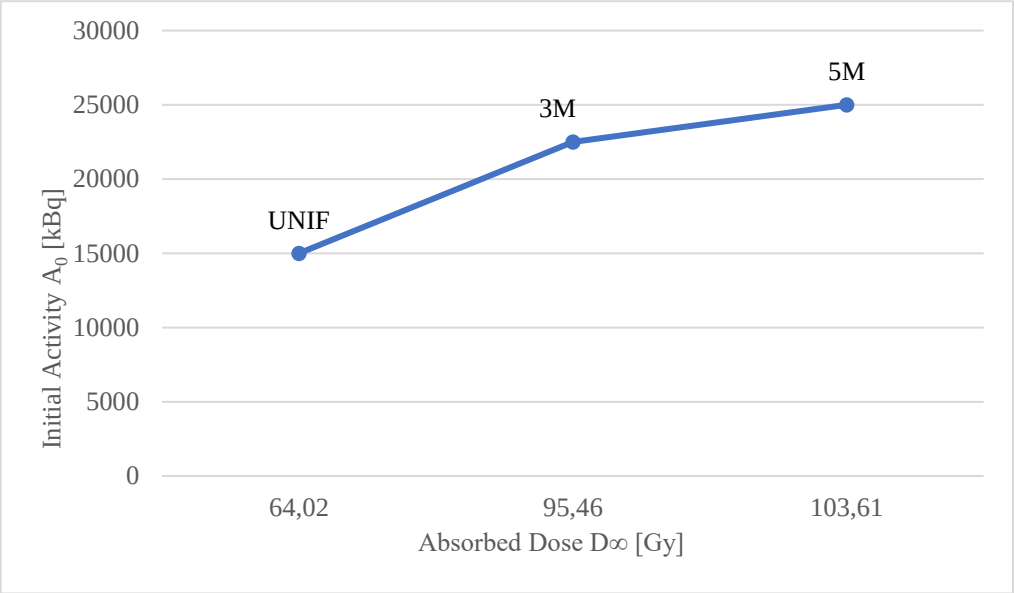

Figure 38: Absorbed dose over the administered activity (D_∞ / A_0) for the different simulations (namely SL-UNIF, SL-3M, SL-5M).

Furthermore, the analysis of the outputs through Matlab permits to obtain the maps of the dose distribution that shows the qualitative and quantitative trend of the dose for each slice in which the geometry is divided. Is in fact possible to interact with the dose maps and obtain the numerical value for each pixel, that allows to evaluate the different values of absorbed dose in every element inside the hexagon.

The different spheres configurations highlight a different distribution of the radioactivity inside the lobule, affecting different region and so different structure. The tissues more closed to the sources are subjected to a higher activity that continues to decrease at a marked rate toward the center of the lobule. This behavior is pointed out from the observation of the dosemaps computed for every configuration. An example is shown in Fig (Fig. 39).

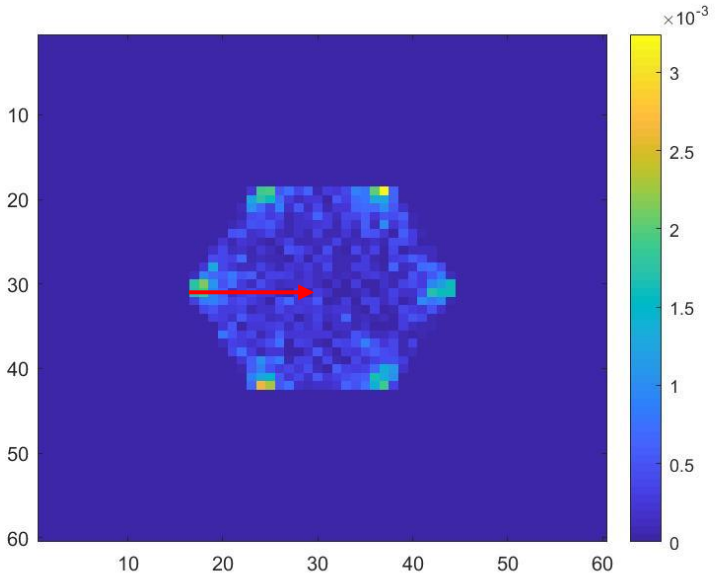

Figure 39: Colormap of dose distribution from region with higher initial activity (where the sphere is set) to the center of the lobule of simulation UNIF. The value decrease as highlight with the arrow, from the source with higher value to the center of the lobule.

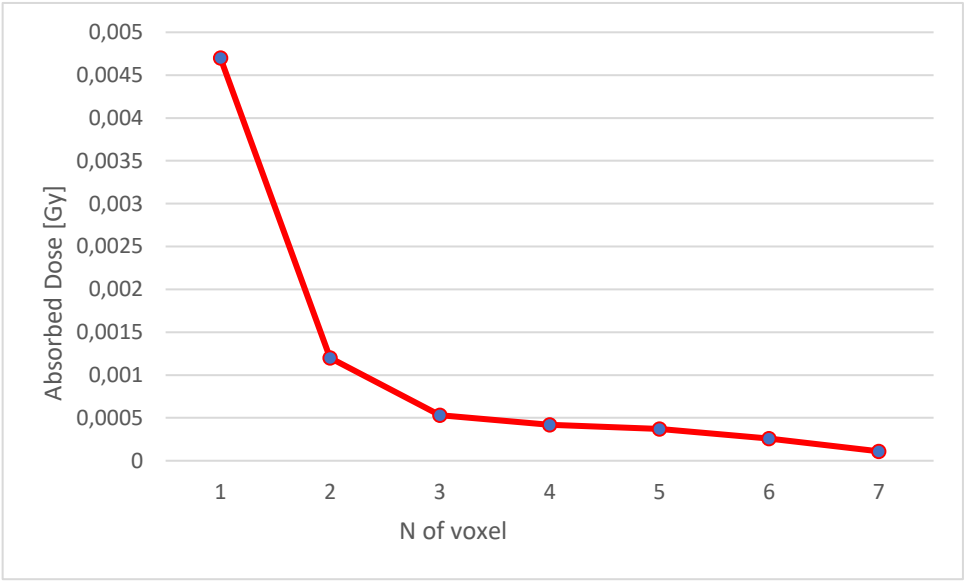

Figure 40: Dose profile refered to Fig 39. Voxel 1 corresponds to the voxel with the higher value in which the source is placed while voxel 7 corresponds to the central voxel of the hexagon.

A decrease of the absorbed dose value occurs moving from the vertex to the center of the lobule (Fig 39 and Fig 40). The absorbed dose decreases drastically in the first millimeters around the source and then it slows down reaching the lobule center. The comparison between the simulations SL-UNIF with respect to the simulations SL-3M and SL-5M shows that the non-uniformity of the dose distribution does not change the total absorbed dose inside the single lobule. The linear ration between the 3 cases is a proof of that.

2. Single tumoral lobule simulation

The dose at the central slice and the subsequent slice are reported in Fig. 36. . The central slice corresponds to the position in which the sources are placed inside the arteriole (Fig 41, top) and each source is clearly visible in each vertex of the lobule. The subsequent slice shows the diffusion of the radioactivity from the sources to the inner lobule region (Fig. 41, bottom).

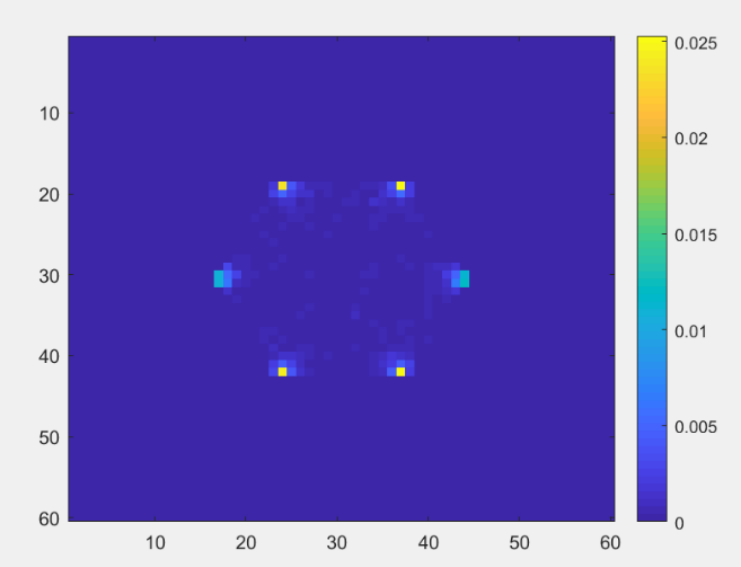

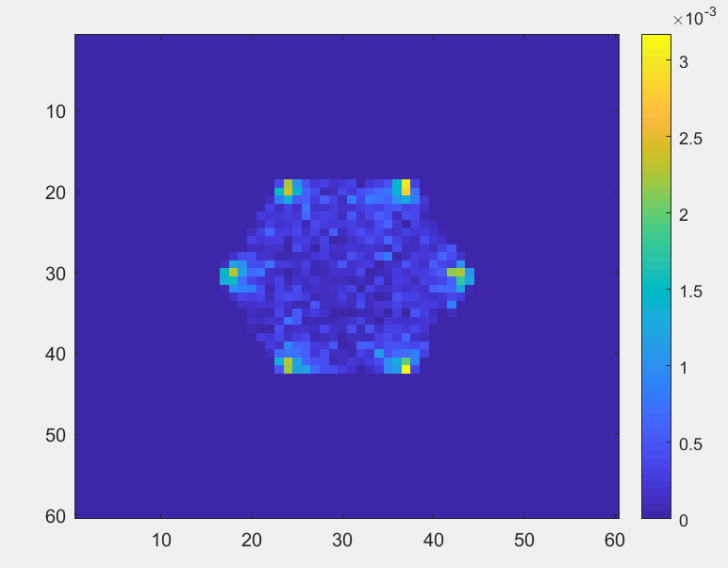

Figure 41: Colormaps of the dose distribution in pathological lobule case simulation: the central slice of the lobule(top), the subsequent slice (bottom) showing the spread of the radiation from the sphere (point with higher value on each corner) to the center of the lobule

A uniform distribution of the spheres and of radiation inside the lobule is shown, as for the case with the normal liver lobule in simulation UNIF. The results of the two simulations are reported in Table 6.

Single tumoral lobule	**Healthy lobule**	**Tumoral lobule**
Initial Activity [kBq]	15	15
Absorbed dose [Gy]	64,02 Gy	61,2 Gy

Table 6: Comparison between the absorbed dose values obtained in Simulation UNIF (healthy lobule) and with a lobule in pathological case (tumor tissue).

The value of total absorbed dose in this case is 61 Gy. A small difference in the absorbed dose (4,40%) was assessed between healthy case and pathologic one as the different materials affect the passage of the radioactive particles through the matter, generating in this situation (tumoral lobule) a lower quantity of absorbed dose. This behavior can indeed be mathematically explained, referring to the definition of the total absorbed dose as. The

absorbed dose, D, is characterized as the mean energy, ΔE, absorbed from a radioactive source by a tissue of matter of mass, Δm, in a limited volume, *V*, by Equation 27 [52].

$$D = \frac{\Delta E}{\Delta m} \quad \text{[Gy]} \qquad (27)$$

The mass can be explained in terms of density and volume:

$$\Delta m = \rho \, x \, V \quad \text{[kg]} \qquad (28)$$

where ρ is the density of the material considered. Substituting the Equation 28 in the Equation 27, it is demonstrated the inversely proportional relationship between D and ρ. With increasing the density material, the relative total absorbed dose decreases (Equation 29).

$$D = \frac{\Delta E}{\rho \, x \, V} \quad \text{[Gy]} \qquad (29)$$

Nevertheless, although it stood to reason that the change of material would have led to an alteration of the absorbed dose, the discrepancy between the two values (healthy lobule – tumoral lobule) is not so significant..

3. Multi lobule simulations

The results of the multi-lobule simulation are reported in the following paragraphs.

For every multi-lobule simulation the central slice of the lobule and the following slice are shown, as well as the absorbed dose through the lobule. A comparison between the administered and absorbed dose in the different cases is performed.

3.1 Multi-lobule, simulation ML-UNIF uniform distribution of sources in normal liver tissue

The dose at the central slice and the following slice are reported in Figs 42 top and bottom. The central slice corresponds to the position in which the sources are placed inside the arteriole (Fig 42, top) and each source is clearly visible in each vertex of the lobule. The subsequent slice shows the diffusion of the radioactivity from the sources to the inner lobule region (Fig. 42, bottom).

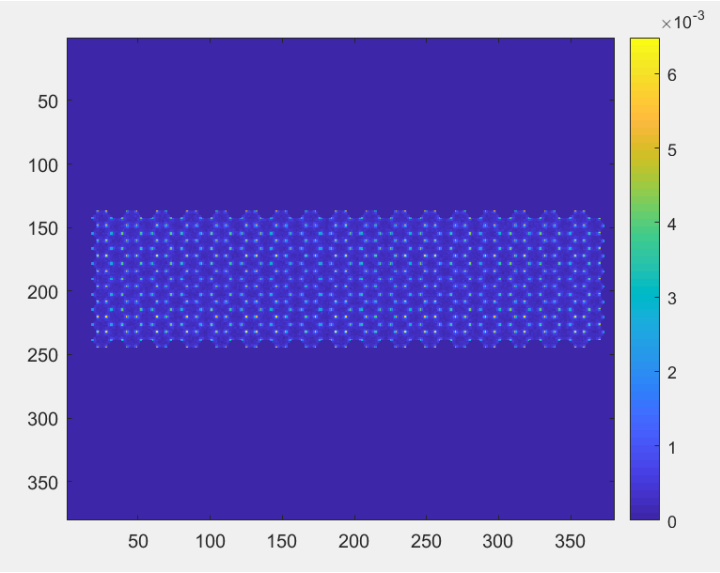

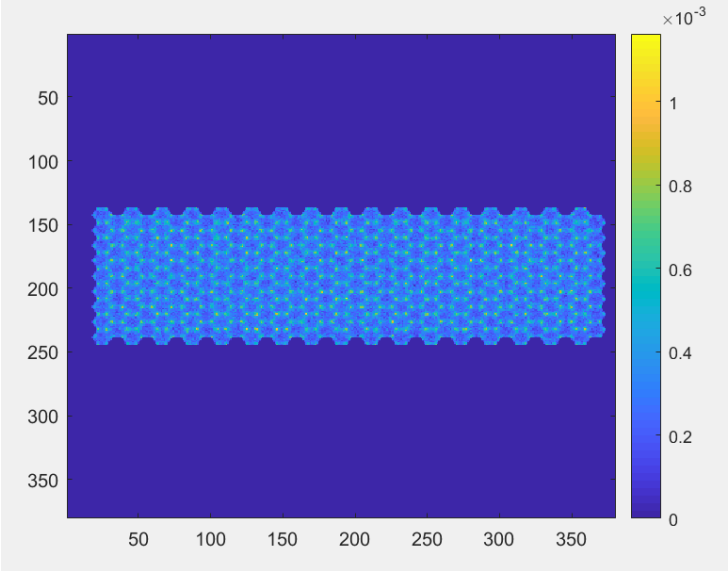

Figure 42: Colormaps of the dose distribution in simulation ML-UNIF: the central slice of the lobule (top) in which the spheres are placed, and the uniform distribution of the sources is clearly visible and the subsequent slice (bottom), in which the spread of the radiation is highlight, with higher values in the surroundings of the sources and lower values in the center of each lobule.

The absorbed dose for each slice is illustrated and plotted in Figure 43:

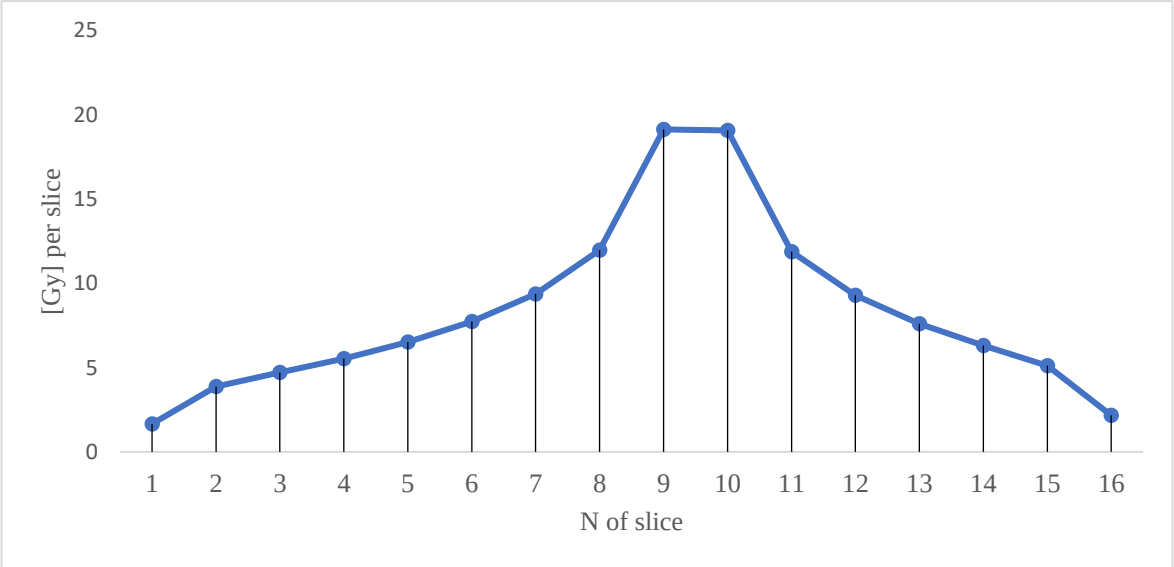

Figure 43: Dose distribution trend through the slices in simulation ML-UNIF. The peak corresponds to the position of the source inside the lobule arterioles. Slice number 1 corresponds to the first frontal slice of the lobule while slice number 16 represents the last face of the lobule. A symmetric trend is noticeable

The results in terms of absorbed dose, obtained with the single lobule in simulation UNIF and the one with the multi-lobule ML-UNIF are compared (Table 7).

	SL-UNIF simulation	**ML-UNIF simulation**
Initial Activity – A_0 [kBq]	15	16575
Absorbed dose - D_∞ [Gy]	64,02	81,49
D_∞ / A_0	4,26 e^{-03}	4,91 e^{-06}

Table 7: Comparison between the absorbed dose values obtained in Simulation UNIF and in multi-lobule simulation ML-UNIF.

The UNIF simulation was performed on a single lobule corresponding to a volume of 1,86 mm^3, the simulation performed on a multi-lobule geometry keeps constant the uniform spheres distribution inside each lobule (one sphere for each vertex, for every lobule), but increase the number of lobule subjected to the treatment to 289, leading to a total liver volume of 538,4 mm^3. The results show a higher absorbed dose in the ML simulation not linearly relate to the result of the UNIF simulation. This highlights the importance of the effect of the adjacent spheres placed in the surrounding lobules. In fact, when simulating a single lobule, the effect of the spheres in the adjacent lobules is neglected. On the contrary, the radiation from other sources placed in the surrounding lobules spread isotropically around each source, affecting and increasing the absorbed dose in the neighboring lobules. A difference of 20Gy is encountered between the two configurations, when simulating a uniform distribution of sources in the tissue.

For this reason, the values obtained with the simulation SL-UNIF cannot be predictive of the absorption of the dose over the total liver. In different studies [6][43] the total administered dose over all the liver is approximate by multiplying the dose absorbed in one lobule for the total number of lobules. The simulation conducted over a greater number of lobule (ML-UNIF) shows a discrepancy with this approximation and highlights the importance of simulate the effect of the neighboring sources and structures.

3.2 Multi-lobule, simulation ML-NOUNIF: non uniform distribution of sources in normal liver tissue

The dose at the central slice and the following slice are reported in Fig. 44. The central slice corresponds to the position in which the sources are placed inside the arteriole (Fig 44, top) and each source is clearly visible in each vertex of the lobule. The subsequent slice shows the diffusion of the radioactivity from the sources to the inner lobule region (Fig. 44, bottom).

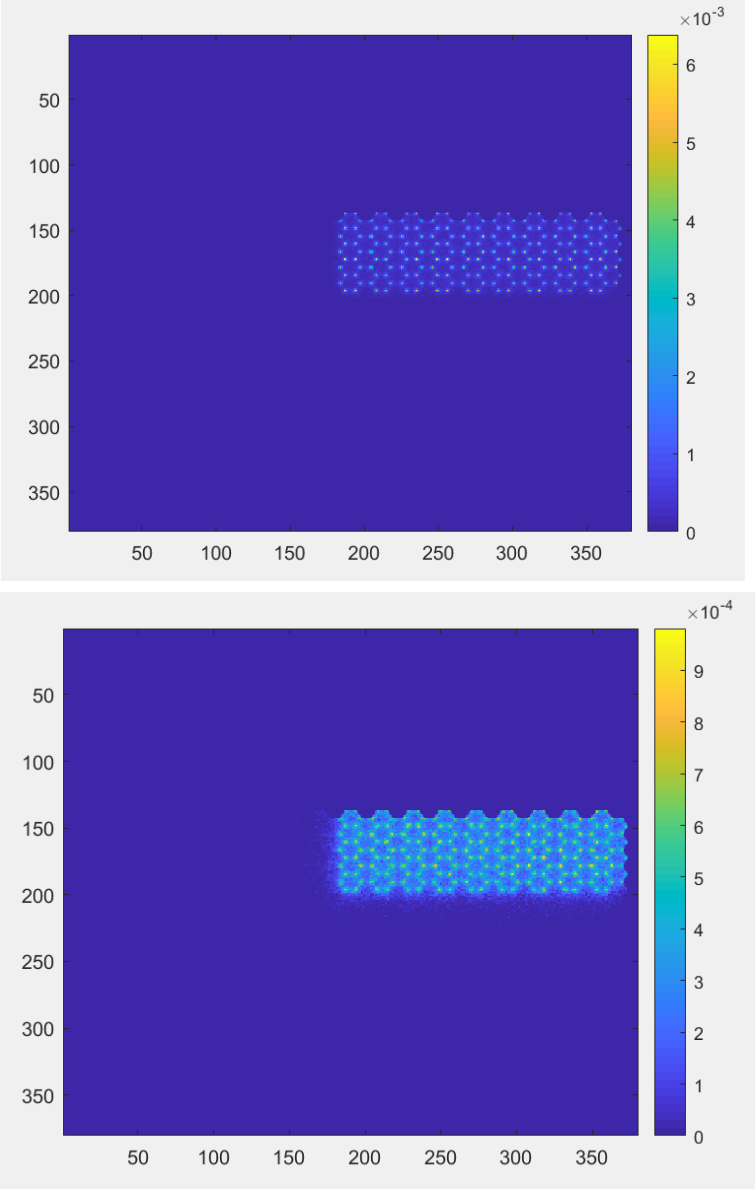

Figure 44: Colormaps of the dose distribution in simulation ML-NOUNIF: the central slice of the lobule (top) in which the spheres are placed, and the non-uniform distribution of the sources is clearly visible. All the sphere are placed in the upper right corner of the area. The subsequent slice (bottom), in which the spread of the radiation is highlight, with higher values in the surroundings of the sources and lower values in the center of each lobule.

The absorbed dose for each slice is computed and plotted in Figure 45:

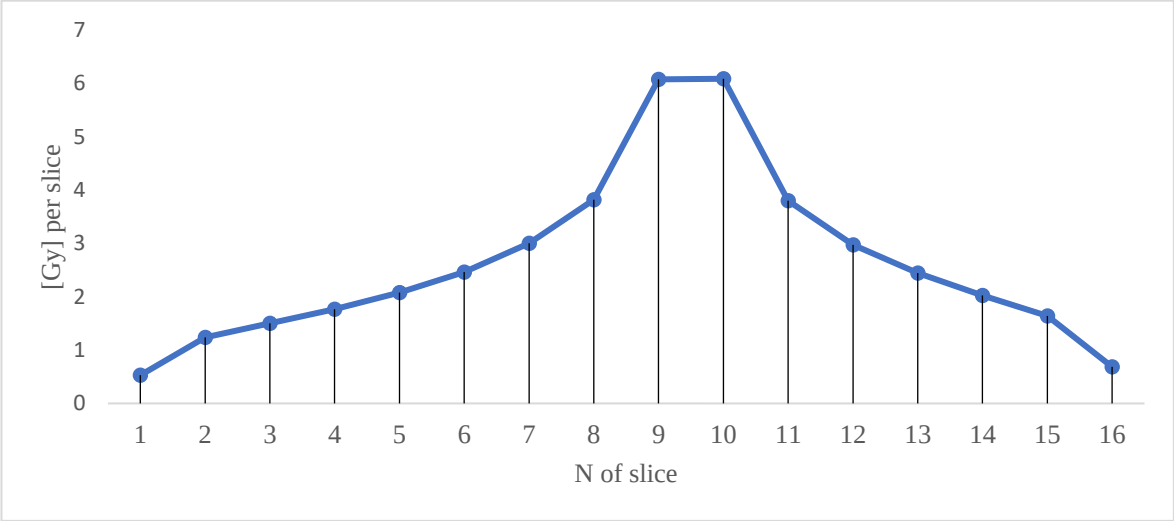

Figure 45: Dose distribution trend through the slices in simulation ML-NOUNIF. The peak corresponds to the position of the source inside the lobule arteriola. Slice number 1 corresponds to the first frontal slice of the lobule while slice number 16 represents the last face of the lobule. A symmetric trend is noticeable

A comparison between the absorbed dose in the case of ML-UNIF and ML-NOUNIF distribution of sources is presented in Table 8:

	ML-UNIF simulation	**ML-NOUNIF simulation**
Initial Activity – A_0 [kBq]	517,5	16575
Absorbed dose - D_∞ [Gy]	26,03	81,49
D_∞ / A_0	4,91 e-06	5,02 e-05

Table 8: Comparison between the total absorbed dose values obtained in Multi-lobule Simulation-1 and in multi-lobule simulation-2.

In contrast to SL simulation results, by modifying the initial administered activity and the surface of tissue involved in the treatment in a ML scenario, there is no longer a linear ratio between the uniform state with respect to the inhomogeneous one. The absorption of the dose is highly dependent on the distribution and placement of the sources inside the tissue. As in the previous case (ML-UNIF), it is further proved the importance of the spread of

radiation from the adjacent radioactive spheres. For this reason, it is important to consider the effect of the surrounding sources to have a complete and more realistic simulation of the treatment.

3.3 Multi-lobule, simulation ML-MIX1: Tumor tissue and normal liver tissue with sources mainly in the tumor tissue

The dose at the central slice and the subsequent slice are shown in Figure 46.

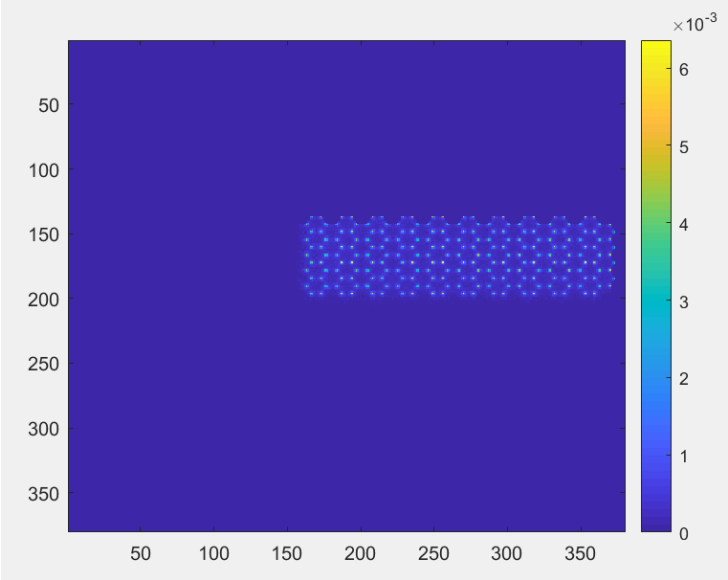

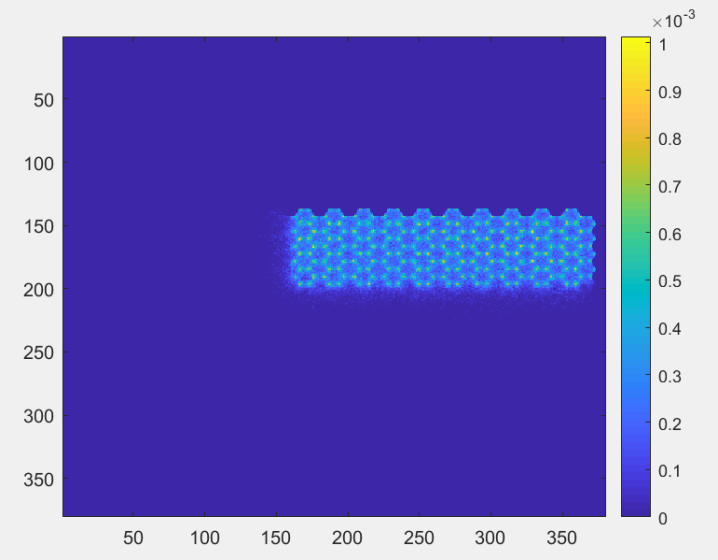

Figure 46: Colormaps of the dose distribution in simulation ML-MIX1: the central slice of the lobule (top) in which the spheres are placed. All the spheres are placed in the upper right corner of the area involving the tumor tissue and a little part of normal tissue. The subsequent slice (bottom), in which the spread of the radiation is highlight, with higher values in the surroundings of the sources and lower values in the center of each lobule.

The absorbed dose for each slice is plotted in Figure 47.

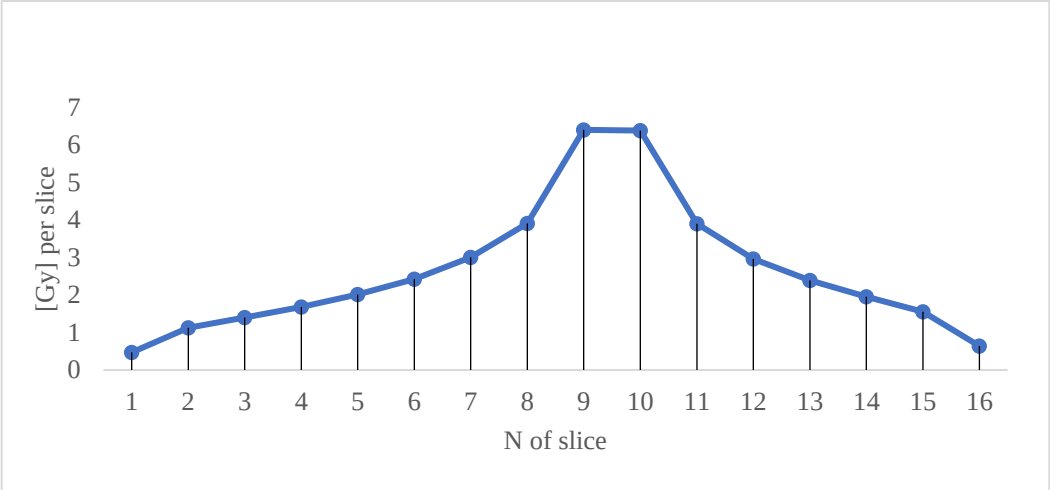

Figure 47: Dose distribution trend through the slices in simulation ML-MIX1. The peak corresponds to the position of the source inside the lobule arteriola. Slice number 1 corresponds to the first frontal slice of the lobule while slice number 16 represents the last face of the lobule. A symmetric trend is noticeable

3.4 Multi-lobule ML-MIX2: Tumor tissue and normal liver tissue with sources mainly in the normal liver

The dose at the central slice and the subsequent slice are shown in Figure 48, top and bottom respectively.

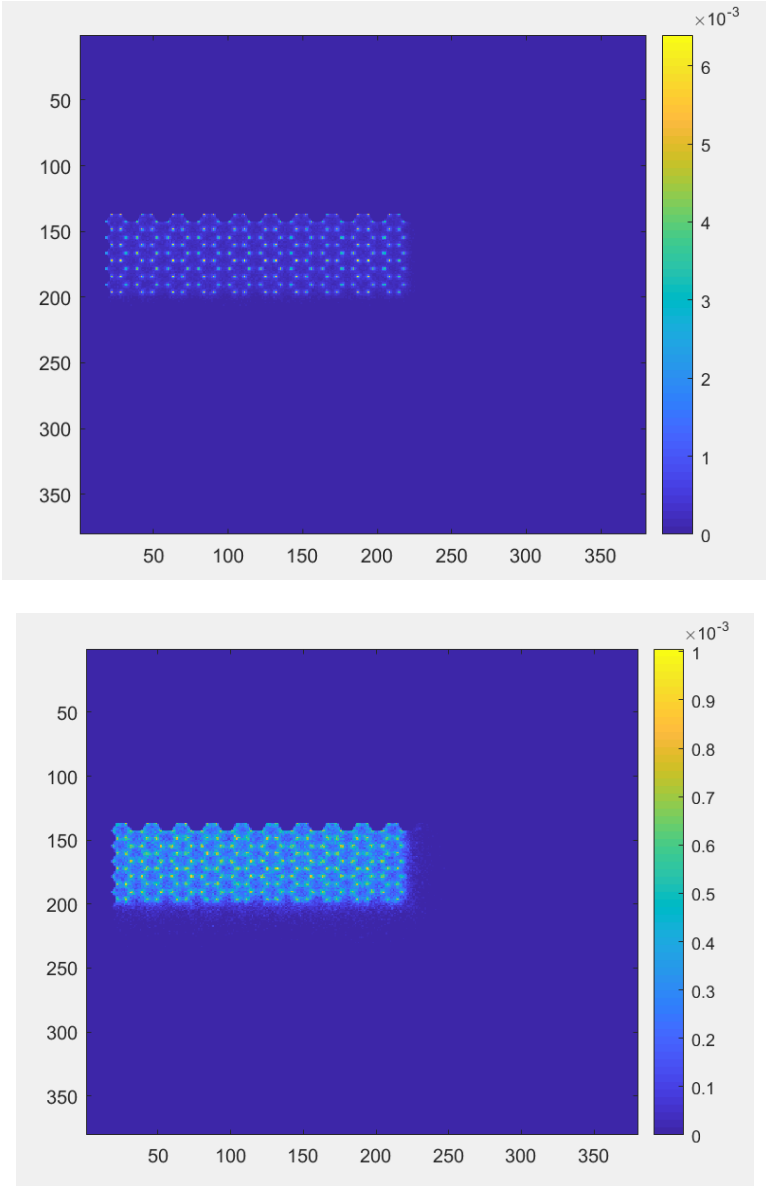

Figure 48: Colormaps of the dose distribution in simulation ML-MIX2: the central slice of the lobule (top) in which the spheres are placed. All the spheres are placed in the upper left corner of the area involving the normal liver tissue and a little part of tumor tissue. The subsequent slice (bottom), in which the spread of the radiation is highlight, with higher values in the surroundings of the sources and lower values in the center of each lobule.

The absorbed dose for each slice is plotted in Figure 49:

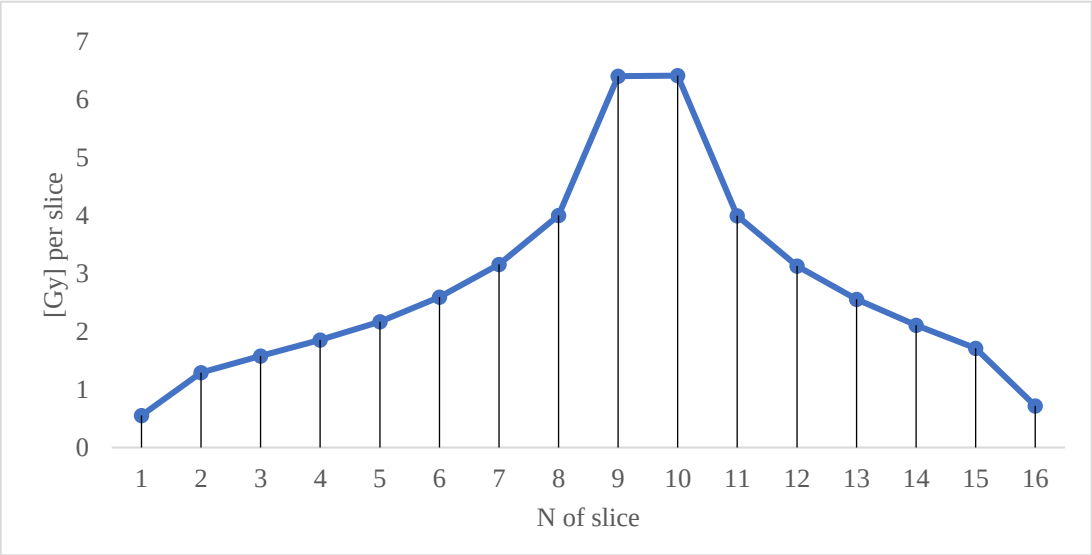

Figure 49: Dose distribution trend through the slices in simulation ML-MIX2. The peak corresponds to the position of the source inside the lobule arteriola. Slice number 1 corresponds to the first frontal slice of the lobule while slice number 16 represents the last face of the lobule. A symmetric trend is noticeable.

The results of the last two cases ML-MIX1 and ML-MIX2 are then compared in Table 9:

	ML-MIX1 simulation	**ML-MIX2 simulation**
Initial Activity [kBq]	550	550
Absorbed dose [Gy]	26,08	27,34

Table 9: Comparison between the total absorbed dose values obtained in simulation ML-MIX1 and in simulation ML-MIX2

Here the two scenarios involved an equal number of radioactive sources acting on an equal surface. In one case the tissue is the healthy liver one, in the other one is composed by tumor tissue.

As mentioned before, differences in the dose absorption between healthy and tumor tissue were highlighted when simulating and comparing the SL-UNIF single lobule case and the single tumor lobule simulation. In accordance with the previous results, a little discrepancy was expected between simulation ML-MIX1 and ML-MIX2. It is indeed highlighted a difference of the 4.60% between the two scenarios.

As described by the Equation 27, 28 and 29, it is newly confirmed that the change of material (and hence of density) affects the passage of the radioactive particles through the matter, generating a lower quantity of absorbed dose.

CHAPTER 4

Conclusions

One of the main concerns in radioembolization is the evaluation of the distribution of the microsphere inside the tumor and the normal liver tissue. The different deposition of the microsphere like non uniform deposition or the formation of cluster of microspheres, can lead to different absorption of the dose by the surrounding tissue (normal and tumor tissue). This can cause collateral effect on the normal liver tissue, or a better treatment of the tumor site. For this reason, the study on the microscopic level, of the different sphere distribution and the correlate absorbed dose by the surrounded tissue, is of main interest in pre-clinical studies of the radioembolization treatment. The main objective of this study was to to develop a microscopic model of the liver lobule able to reproduce the microarchitecture and microvasculature of the hepatic region both in the physiological and pathological cases, to predict the radiation distribution and the consequent absorbed dose. The software GATE was used to set-up and perform the simulations after a validation against literature data from Gulec et al. [6]

The software was complemented by a Matlab script that allows to obtain, given the size of the desired lobule area, the complete macrofile for GATE, regarding the lobule geometry and sphere definition and placement.

Two set of simulations were formed: SL and ML. The simulations performed on a SL assessed a linear relationship between the administered and absorbed dose in different cases of uniform and non-uniform sources distribution.

The ML simulations include four different scenarios. The first two scenarios with, respectively, a uniform and non-uniform distribution of the sources inside a healthy liver tissue. The last two scenarios involve a region of tumor tissue with two different configurations of the sources. The first one with the sources mainly at the tumor, and the second one with the sources mainly at the healthy liver tissue.

The linear relationship between the administered and absorbed dose in the case of uniform and non-uniform sources distributions for the ML is not preserved. This fact can be explained due to the mutual influence of the neighboring sources in the total computation of absorbed

activity. The radiation spreads from one source no longer just inside one lobule but affecting the surrounding structures. This results in an increased absorbed dose not related with the one lobule simulation. Comparing the two simulations with the tumor (ML-MX1 and ML-MX2) a higher absorption in the healthy liver tissue with respect to the tumor was found. The tumor is in fact a denser material and for this is less penetrated by radiation.

The main limitation of this work is the reduced number of lobules due to calculations limitations imposed by the computational machine used (Asus X555Q, CPU AMD Quad Core A10-9600P radeon R5, 10 compute cores 4C+6G 2.40 Ghz, 16 Gb RAM). Even if the multi-lobules model allowed to compare the absorption when treating majorly the tumor site or the normal liver tissue, a more realistic scenario is required for the modeling of a larger portion of the liver/tumor and, consequently, higher numbers of lobules.

Secondly, lacking literature data, the tumor was modelled by changing the density with respect to the healthy tissue. Although from CT analysis the tumor can be considered a denser material with respect to the healthy one [116] [117], there are no specific biological available data. Therefore, the assumption of a density value of 1,4 g/cm^3 here proposed is just an approximation to simulate a different and denser material, accordingly also to what suggested by the GATE community.

To conclude, the reported microstructural dosimetry model can help in the detailed assessment of the dose distributions in the hepatic subunits and in relating these codes to their effects.

Nevertheless, the small-scale dosimetry model of the liver tissue created in the project is still at an early stage. Some improvement needs to be made.

First of all, the work will benefit of the simulation of a larger portion of the liver and tumor. Secondly, to better describe the microsphere distribution, it is mandatory to obtain a realist description of the tumor tissue. Lastly, a user-friendly interface could be developed based on the implemented Matlab script to allow the users to easily define the geometry, the material parameters and sources placement.

BIBLIOGRAPHY

[1] Guyton, A. C. and Hall, J. E. (2006), 'Textbook of Medical Physiology', Elsevier.

[2] Patton, K. and Thibodeau, G. (2010), 'Anatomy and physiology', 7 edn, Louis.

[3] Martini, F., Timmons, M.J. and Tallitsch R. B. (2015), 'Human Anatomy', 8 edn, Pearson Benjamin Cummings

[4] Haobam, R. S. (2018), 'Study of the Anatomical Variations of the Liver in Human', PhD Thesis, The Tamil Nadu Dr. M.G.R. Medical University

[5] Simoncini, C. (2017), 'Patient-specific numerical modelling for the optimization of HCC Selective Internal Radiation Therapy: an image based approach', PhD Thesis, University of Rennes 1.

[6] Gulec, S. A., Sztejnberg, M. L., Siegel, J. A., Jevremovic, T. and Stabin, M. (2010), 'Hepatic Structural Dosimetry in 90Y Microsphere Treatment: A Monte Carlo Modeling Approach Based on Lobular Microanatomy', J. Nucl. Med. 51(2), 301–310.

[7] Virtual Liver: 3D Liver Anatomy (2012).
URL: http://pie.med.utoronto.ca/vliver/

[8] Hitachi Medical Systems America Inc. (2012), 'MRI Anatomy and Positioning Series'.
URL: http://www.hitachimed.com/self-learning-activity/docs/AbdominalImagingModule

[9] Pescia, D. (2011). 'Segmentation des tumeurs du foie sur des images CT. (Segmentation of liver tumors on CT images)', PhD Thesis, Ecole Centrale de Paris, MAS laboratory.

[10] Luersen, G., Bhosale, P., Szklaruk, J. (2015), ‘State-of-the-art cross-sectional liver imaging: beyond lesion detection and characterization’, Journal of Hepatocellular Carcinoma.

[11] Mescher, A.L. (2010), ‘Junqueira's Basic Pathology’, Text & Atlas. 12th ed 2010: The McGraw-Hill Companies.

[12] Bray F, Ferlay J, Soerjomataram I, Siegel RL, Torre LA, Jemal A., ‘Global cancer statistics 2018: GLOBOCAN estimates of incidence and mortality worldwide for 36 cancers in 185 countries’, CA Cancer J Clin. 2018;68:394–424

[13] Schuppan, D., Afdhal, N.H. (2008), “Liver Cirrhosis”, Lancet. 2008 March 8; 371(9615): 838–851.

[14] Llovet JM, Zucman-Rossi J, Pikarsky E, Sangro B, Schwartz M, Sherman M, Gores G. (2016) ‘Hepatocellular carcinoma’, Nat Rev Dis Primers. 2016;2:16018.

[15] El-Serag HB (2017),’Hepatocellular carcinoma’. N Engl J Med 2011;365:1118-1127

[16] Witjes CD, Karim-Kos HE, Visser O, et al. (2012). ‘Hepatocellular carcinoma in a low-endemic area: rising incidence and improved survival’, Eur J Gastroenterol Hepatol 2012;24:450-457.

[17] H. H. Marti (2005), “Angiogenesis–a self-adapting principle in hypoxia,” EXS, no. 94, pp. 163–180.

[18] D. Hanahan and J. Folkman (1996), “Patterns and emerging mechanisms of the angiogenic switch during tumorigenesis,” Cell, vol. 86, no. 3, pp. 353–364.

[19] Edge, S., Byrd, D., Compton, C., Fritz, A., Greene, F. and Trotti, A. (2010), ‘American Joint Committee on Cancer (AJCC) cancer staging manual’, Springer.

[20] Paloma Sanz-Cameno, María Trapero-Marugán, María Chaparro, Evan Anthony Jones, and Ricardo Moreno-Otero (2010), 'Angiogenesis: From Chronic Liver Inflammation to Hepatocellular Carcinoma', Journal of Oncology, vol. 2010, Article ID 272170, 7 pages.

[21] J. Cazejust, B. Bessoud, N. Colignon, C. Garcia-Alba, O. Planché, Y. Menu (2014), 'Hepatocellular carcinoma vascularization: From the most common to the lesser known arteries', Journal de Radiologie Diagnostique et Interventionnelle, Volume 95, Issue 1, January 2014, Pages 30-39

[22] Balogh, J., Victor, D., 3rd, Asham, E. H., Burroughs, S. G., Boktour, M., Saharia, A., Monsour, H. P., Jr (2016). Hepatocellular carcinoma: a review. Journal of hepatocellular carcinoma, 3, 41–53.

[23] Sacco, R., Mismas, V., Marceglia, S., Romano, A., Giacomelli, L., Bertini, M., Bargellini, I. (2015). Transarterial radioembolization for hepatocellular carcinoma: An update and perspectives. World journal of gastroenterology, 21(21), 6518–6525.

[24] Andreana, L., Isgrò, G., Marelli, L., Davies, N., Yu, D., Navalkissoor, S. and Burroughs, A. K. (2012), 'Treatment of hepatocellular carcinoma (HCC) by intra-arterial infusion of radio-emitter compounds: trans-arterial radio-embolisation of HCC.', Cancer Treat. Rev. 38(6), 641–9.

[25] Raoul, J.-L., Sangro, B., Forner, A., Mazzaferro, V., Piscaglia, F., Bolondi, L. and Lencioni, R. (2011), 'Evolving strategies for the management of intermediate-stage hepatocellular carcinoma: available evidence and expert opinion on the use of transarterial chemoembolization.', Cancer Treat. Rev. 37(3), 212–20.

[26] Murthy, R., Nunez, R., Szklaruk, J., Erwin, W., Madoff, D. C., Gupta, S., Ahrar, K., Wallace, M. J., Cohen, A., Coldwell, D. M., Kennedy, A. S. and Hicks, M. E. (2005), 'Yttrium-90 microsphere therapy for hepatic malignancy: devices, indications, technical considerations, and potential complications.', Radiographics 25 Suppl 1, S41–S55.

[27] Braat AJAT, Kappadath SC, Bruijnen RCG, van den Hoven AF, Mahvash A, de Jong HWAM, et al. (2017), 'Adequate SIRT activity dose is as important as adequate chemotherapy dose', Lancet Oncol Elsevier Ltd. 2017;18:e636

[28] Koloukani, S.A., Cao, A., Cao, Q. (2014) Radioembolization of Yttrium-90 Microspheres for Clinical Treatment of Hepatic Malignancy. J Nucl Med Radiat Ther 5:187.

[29] Kennedy, A. S., Nutting, C., Coldwell, D., Gaiser, J. and Drachenberg, C. (2004), 'Pathologic response and microdosimetry of (90)Y microspheres in man: review of four explanted whole livers.', Int. J. Radiat. Oncol. Biol. Phys. 60(5), 1552–63.

[30] Carr, B. I. (2004), 'Hepatic arterial 90Yttrium glass microspheres (Therasphere) for unresectable hepatocellular carcinoma: interim safety and survival data on 65 patients.', Liver Transpl. 10, S107–S110.

[31] Sundram, F. X., (2017), 'Selective internal radiation therapy for liver tumours', Clinical Medicine 2017 Vol 17, No 5:449-53.

[32] Garin, E., Rolland, Y., Laffont, S. and Edeline, J. (2016), 'Clinical impact of 99mTc-MAA SPECT/CT-based dosimetry in the radioembolization of liver malignancies with 90Yloaded microspheres', Eur. J. Nucl. Med. Mol. Imaging 43(3), 559–575.

[33] Garin, E., Lenoir, L., Rolland, Y., Edeline, J., Mesbah, H., Laffont, S., Poree, P., Clement, B., Raoul, J.-L. and Boucher, E. (2012), 'Dosimetry Based on 99mTc-Macroaggregated Albumin SPECT/CT Accurately Predicts Tumor Response and Survival in Hepatocellular Carcinoma Patients Treated with 90Y-Loaded Glass Microspheres: Preliminary Results', J. Nucl. Med. 53(2), 255–263.

[34] Pasciak, A. S., Bradley, Y., McKinney, I. M.,(2016) ' Handbook of Radioembolization: physics, biology, nuclear medicine and imaging', CRC Press, I edn.

[35] Wang, E. A., Broadwell, S. R., Bellavia, R. J., & Stein, J. P. (2017). Selective internal radiation therapy with SIR-Spheres in hepatocellular carcinoma and cholangiocarcinoma. Journal of gastrointestinal oncology, 8(2), 266–278.

[36] Rault, E., Vandenberghe, S., Staelens, S., Lemahieu, I. (2009), 'Optimization of Yttrium-90 Bremsstrahlung Imaging with Monte Carlo Simulations', 4th European Conference of the International Federation for Medical and Biological Engineering. 22. pp. 500–504. Retrieved 21 October 2013

[37] Elschot, M., Vermolen, B. J., Lam, M. G. E. H., de Keizer, B., van den Bosch, M. A. A. J. and de Jong, H. W. A. M. (2013), 'Quantitative Comparison of PET and Bremsstrahlung SPECT for Imaging the In Vivo Yttrium-90 Microsphere Distribution after Liver Radioembolization', PLoS One 8(2).

[38] Wondergem, M., Smits, M.L.J. (2013), '99mTc-Macroaggregated Albumin Poorly Predicts the Intrahepatic Distribution of 90Y Resin Microspheres in Hepatic Radioembolization', J Nucl Med August 1, 2013 vol. 54 no. 8 1294-1301.

[39] Ray, C. E., Battaglia, C., Libby, A. M., Prochazka, A., Xu, S. and Funaki, B. (2012), 'Interventional radiologic treatment of hepatocellular carcinoma-A cost analysis from the payer perspective', J. Vasc. Interv. Radiol. 23(3), 306–314.

[40] Schwen, L. O., Preusser, T., (2012), 'Analysis and Algorithmic Generation of Hepatic Vascular Systems', International Journal of Hepatology, vol. 2012, Article ID 357687.

[41] Schwen LO, Krauss M, Niederalt C, Gremse F, Kiessling F, et al. (2014), 'Spatio-Temporal Simulation of First Pass Drug Perfusion in the Liver. PLOS Computational Biology 10(3): e1003499.

[42] White, D., Coombe, D., Rezania, V. and Tuszynski, J. (2016), 'Building a 3D Virtual Liver: Methods for Simulating Blood Flow and Hepatic Clearance on 3D Structures', PLoS One 11(9), 1–24.

[43] Walrand, S., Hesse, M., Chiesa, C., Lhommel, R. and Jamar, F. (2014a), 'The Low Hepatic Toxicity per Gray of 90Y Glass Microspheres Is Linked to Their Transport in the Arterial Tree Favoring a Nonuniform Trapping as Observed in Posttherapy PET Imaging', J. Nucl. Med. 55, 135–141.

[44] Walrand, S., Hesse, M., Jamar, F. and Lhommel, R. (2014b), 'A hepatic dose-toxicity model opening the way toward individualized radioembolization planning.', J. Nucl. Med. 55(8), 1317–22.

[45] Basciano, C. A., Kleinstreuer, C., Kennedy, A. S., Dezarn, W. A. and Childress, E. (2010), 'Computer modeling of controlled microsphere release and targeting in a representative hepatic artery system.', Ann. Biomed. Eng. 38(5), 1862–79.

[46] Kennedy, A. S., Kleinstreuer, C., Basciano, C. A. and Dezarn, W. A. (2010), 'Computer Modeling of Yttrium-90-Microsphere Transport in the Hepatic Arterial Tree to Improve Clinical Outcomes', Int. J. Radiat. Oncol. Biol. Phys. 76(2), 631–637.

[47] Kleinstreuer, C., Basciano, C. a., Childress, E. M. and Kennedy, a. S. (2012), 'A new catheter for tumor targeting with radioactive microspheres in representative hepatic artery systems. Part I: impact of catheter presence on local blood flow and microsphere delivery.', J. Biomech. Eng. 134(5), 051004.

[48] Childress, E. M. and Kleinstreuer, C. (2014b), 'Impact of fluid-structure interaction on direct tumor-targeting in a representative hepatic artery system.', Ann. Biomed. Eng. 42(3), 461–74.

[49] Childress, E. M., Kleinstreuer, C. and Kennedy, A. S. (2012), 'A new catheter for tumor targeting with radioactive microspheres in representative hepatic artery systems. Part II: solid tumor-targeting in a patient-inspired hepatic artery system.', J. Biomech. Eng. 134(5), 051005.

[50] Kennedy, Andrew S., Charles Nutting, Douglas Coldwell, James Gaiser, e Cinthia Drachenberg. «Pathologic Response and Microdosimetry of 90Y Microspheres in Man: Review of Four Explanted Whole Livers». International Journal of Radiation Oncology*Biology*Physics 60, n. 5 (dicembre 2004): 1552–63.

[51] http://icrpaedia.org/Absorbed,_Equivalent,_and_Effective_Dose

[52] Cremonesi, Marta, Carlo Chiesa, Lidia Strigari, Mahila Ferrari, Francesca Botta, Francesco Guerriero, Concetta De Cicco, et al. «Radioembolization of Hepatic Lesions from a Radiobiology and Dosimetric Perspective». Frontiers in Oncology 4 (19 agosto 2014).

[53]Dezarn, William A., Jeffery T. Cessna, Larry A. DeWerd, Wenzheng Feng, Vanessa L. Gates, James Halama, Andrew S. Kennedy, et al. «Recommendations of the American Association of Physicists in Medicine on Dosimetry, Imaging, and Quality Assurance Procedures for ^{90} Y Microsphere Brachytherapy in the Treatment of Hepatic Malignancies: AAPM Recommendations ^{90} Y Microsphere Brachytherapy». Medical Physics 38, n. 8 (1 agosto 2011): 4824–45.

[54] Pasciak, Alexander S., Austin C. Bourgeois, e Yong C. Bradley. «A Comparison of Techniques for 90Y PET/CT Image-Based Dosimetry Following Radioembolization with Resin Microspheres». Frontiers in Oncology 4 (22 maggio 2014).

[55] Vauthey, J. «Body Surface Area and Body Weight Predict Total Liver Volume in Western Adults». Liver Transplantation 8, n. 3 (marzo 2002): 233–40.

[56] Gallio, Elena, Elisa Richetta, Monica Finessi, Michele Stasi, Riccardo Emanuele Pellerito, Gianni Bisi, e Roberto Ropolo. «Calculation of Tumour and Normal Tissue Biological Effective Dose in 90 Y Liver Radioembolization with Different Dosimetric Methods». Physica Medica 32, n. 12 (dicembre 2016): 1738–44.

[57] Chiesa, C., M. Mira, M. Maccauro, C. Spreafico, R. Romito, C. Morosi, T. Camerini, et al. «Radioembolization of Hepatocarcinoma with 90Y Glass Microspheres: Development of an Individualized Treatment Planning Strategy Based on Dosimetry and Radiobiology». European Journal of Nuclear Medicine and Molecular Imaging 42, n. 11 (ottobre 2015): 1718–38.

[58] Richetta, Elisa, Massimo Pasquino, Matteo Poli, Claudia Cutaia, Chiara Valero, Marco Tabone, Benedetta Peiretti Paradisi, Massimiliano Pacilio, Riccardo Emanuele Pellerito, e Michele Stasi. «PET-CT Post Therapy Dosimetry in Radioembolization with Resin 90Y Microspheres: Comparison with Pre-Treatment SPECT-CT 99mTc-MAA Results». Physica Medica 64 (agosto 2019): 16–23.

[59] Bastiaannet, Remco, S. Cheenu Kappadath, Britt Kunnen, Arthur J. A. T. Braat, Marnix G. E. H. Lam, e Hugo W. A. M. de Jong. «The Physics of Radioembolization». EJNMMI Physics 5, n. 1 (dicembre 2018).

[60] Dieudonné, Arnaud, Robert F. Hobbs, Manuel Sanchez-Garcia, e Rachida Lebtahi. «Absorbed-Dose Calculation for Treatment of Liver Neoplasms with 90Y-Microspheres». Clinical and Translational Imaging 4, n. 4 (agosto 2016): 273–82.

[61] Ng, Sherry C., Victor H. Lee, Martin W. Law, Rico K. Liu, Vivian W. Ma, Wai Kuen Tso, e To Wai Leung. «Patient Dosimetry for 90Y Selective Internal Radiation Treatment Based on 90Y PET Imaging». Journal of Applied Clinical Medical Physics 14, n. 5 (settembre 2013): 212–21.

[62] Strigari, L., R. Sciuto, S. Rea, L. Carpanese, G. Pizzi, A. Soriani, G. Iaccarino, M. Benassi, G. M. Ettorre, e C. L. Maini. «Efficacy and Toxicity Related to Treatment of Hepatocellular Carcinoma with 90Y-SIR Spheres: Radiobiologic Considerations». Journal of Nuclear Medicine 51, n. 9 (1 settembre 2010): 1377–85.

[63] Jones, L C, e P W Hoban. «Treatment Plan Comparison Using Equivalent Uniform Biologically Effective Dose (EUBED)». Physics in Medicine and Biology 45, n. 1 (1 gennaio 2000): 159–70.

[64] Tong, Aaron K T, Yung Hsiang Kao, Chow Wei Too, Kenneth F W Chin, David C E Ng, e Pierce K H Chow. «Yttrium-90 Hepatic Radioembolization: Clinical Review and Current Techniques in Interventional Radiology and Personalized Dosimetry». The British Journal of Radiology 89, n. 1062 (giugno 2016): 20150943.

[65] Ho S, Lau WY, Leung TWT, Chan M, Ngar YK, Johnson PJ, et al. Partition model for estimating radiation doses from yttrium-90 microspheres in treating hepatic tumours. Eur J Nucl Med. 1996;23:947–52.

[66] Bombardieri E, Seregni E, Evangelista L, Chiesa C, Chiti A (Eds.) Clinical Applications of Nuclear Medicine Targeted Therapy. Springer International Publishing Switzerland 2018. ISBN 978-3-319-63067-0

[67] Therasphere®byBTG. (http://www.therasphere.com). Available from: http://www.therasphere.com/physicians-package-insert/package-insert-eu- en.pdf

[68] Kahn, H. (1956), 'Applications of Monte Carlo: AEC-3259', The Rand Corporation.

[69] Harrison, R. L. (2010), 'Introduction to Monte Carlo simulation', AIP Conf Proc. 2010 January 5; 1204: 17–21.

[70] Kalos, M. H., Whitlock, P. A. (2008), 'Monte Carlo methods', Wiley-VCH.

[71] Rubinstein, R. Y., Kroese, D. P. (2007), 'Simulation and the Monte Carlo Model', John Wiley and Sons, II ed.

[72] Raeside, D. E. (1976), 'Monte Carlo principles and applications', Physics in Medicine and Biology, vol. 21, pp 181-197.

[73] Crowe, S. B. (2011), 'The development of Monte Carlo techniques for the verification of radiotherapy treatments', PhD Thesis, Queensland University of Technology.

[74] Brown, F.B. (2005), 'Fundamentals of Monte Carlo Particle Transport', Lecture Notes for Monte Carlo course, Los Alamos National Laboratory report, LA-UR-05-4983:

[75] Rogers, D. W. O., Bielajew, A. F (1990) 'Monte Carlo Techniques of Electron and Photon Transport for Radiation Dosimetry', National Research Council of Canada, The Dosimetry of Ionizing Radiation, Chapter 5, Vol. III

[76] Stenvall, A. (2012), 'A small-scale dosimetry model of the liver tissue', PhD Thesis, Lund University.

[77] Cecen, Y. (2013), 'Monte Carlo radiation transport in external beam radiotherapy', Bitlis Eren Univ J sci & Technol, ISSN 2146-7706.

[78] Villoing, D., Marcatili, S., Garcia, M.P., Bardiès, M. (2017), 'Internal dosimetry with Monte Carlo code GATE: validation using ICRP/ICRU female reference computational model', Phys. Med. Biol. 62 1885–1904

[79] Cherry, S. R., J. A. Sorenson, and M. E. Phelps (2012), 'Physics in nuclear medicine', Elsevier/Saunders, Philadelphia, 4th ed edition. ISBN 9781416051985.

[80] Podgorsak, E. B. (2005),'Radiation oncology physics: a handbook for teachers and Students', International Atomic Energy Agency, Vienna. ISBN 9201073046.

[81] G.Z. Molière: Z. Naturforsch. 3a, 78 (1948).

[82] S. Goudsmit, J. L. Saunderson: Phys. Rev. 57, 24 (1940).

[83] Lewis, H.W., (1950) ‘Multiple scattering in an infinite medium’, Phys. Rev. 78, 526–529.
[84] Berger, M. J. (1963), ‘Monte Carlo Calculation of the penetration and diffusion of fast charged particles’, Methods in Comput. Phys., 1:135 – 215.

[85] Chiavassa, S., Lemosquet, A., Aubineau-Lanièce, I., de Carlan, L.,Clairand, I., Ferrer, L., Bardiès, M., Franck, D., Zankl, M. (2005),’Dosimetric comparison of Monte Carlo codes (EGS4, MCNP, MCNPX) considering external and internal exposures of the Zubal phantom to electron and photon sources’, Radiation Protection Dosimetry, Volume 116, Issue 1-4, 20 December 2005, Pages 631–635.

[86] Sarrut, D. , Bardiès, M. , Boussion, N. , Freud, N. , Jan, S. , Létang, J. , Loudos, G. , Maigne, L. , Marcatili, S. , Mauxion, T. , Papadimitroulas, P. , Perrot, Y. , Pietrzyk, U. , Robert, C. , Schaart, D. R., Visvikis, D. and Buvat, I. (2014), ‘A review of the use and potential of the GATE Monte Carlo simulation code for radiation therapy and dosimetry applications’, Med. Phys., 41: 064301.

[87] I. Kawrakow, E. Mainegra-Hing, D. Rogers, F. Tessier, and B. Walters (2010), ‘The egsnrc code system: Monte carlo simulation of electron and photon transport’, National Research Council of Canada, NRCC Report PIRS-701.

[88] P. Andreo and M. Ljungberg (1998), ‘General Monte Carlo Codes for use in Medical Radiation Physics’, ser. Medical Science Series, Institute of Physics Publishing, ch. 4

[89] A. Bielajew, H. Hirayama, W. Nelson, and D. Rogers (1994), ‘History, overview and recent improvements of egs4’, National Research Council of Canada and National Laboratory for High Energy Physics and Stanford Linear Accelerator Center.

[90] M. Stabin and H. Zaidi (2003), ‘Monte Carlo Codes for use in therapeutic nuclear medicine’, ser. Series in Medical Physics and Biomedical Engineering, Institute of Physics Publishing, ch. 6

[91] D. Visvikis, M. Bardies, S. Chiavassa, C. Danford, A. Kirov, F. Lamare, L. Maigne, S. Staelens, R. Taschereau (2006), 'Use of the GATE Monte Carlo package for dosimetry applications', Nucl. Instrum. Methods A 569, 335-340

[92] C. O.Thiam, V. Breton, D.Donnarieix, B. Habib, and L.Maigne (2008), 'Validation of a dose deposited by low-energy photons using GATE/GEANT4', Phys. Med. Biol. 53, 3039–3055

[93] L. Grevillot, T. Frisson, N. Zahra, D. Bertrand, F. Stichelbaut, N. Freud, D.Sarrut (2010), 'Optimization of GEANT4 settings for Proton Pencil Beam Scanning simulations using GATE', Nucl. Instrum. Methods in Phys. Research B 268, 3295–3305

[94] L. Maigne, Y. Perrot, D. R.Schaart, D.Donnarieix, and V. Breton (2011),'Comparison of GATE/GEANT4 with EGSnrc and MCNP for electron dose calculations at energies between 15 keV and 20 MeV', Phys. Med. Biol. 56, 811-827

[95] P. Papadimitroulas, G.Loudos, G. C. Nikiforidis, and G. C. Kagadis (2012), 'A dose point kernel database using GATE Monte Carlo simulation toolkit for nuclear medicine applications: Comparison with other Monte Carlo codes', Med. Phys. 39 (8), 5238-5247

[96] S. Benhalouche, D. Visvikis, A. Le Maitre, O. Pradier, and N. Boussion (2013), 'Evaluation of clinical IMRT treatment planning using the GATE Monte Carlo simulation platform for absolute and relative dose calculations', Med. Phys.40, 021711-1-021711-12

[97] H-RSadoughi, S.Nasseri, M.Momennezhad, H-R Sadeghi, and M-H Bahreyni-Toosi (2014),'A Comparison Between GATE and MCNPX Monte Carlo Codes in Simulation of Medical Linear Accelerator', J Med Signals Sens. Jan-Mar; 4(1): 10–17

[98] Y.Tayalati, S.Didi, M.Zerfaoui,and A. Moussa (2013),"Monte Carlo Simulation of 6MV Elekta Synergy Platform Linac photon beam using Gate/Geant4'.

[99] C. J. Boylan, A. H. Aitkenhead, C. G. Rowbottom, and R. I. Mackay (2013),'Simulation of realistic linac motion improves the accuracy of a Monte Carlo based VMAT plan QA system', Radiotherapy and Oncology 109, 377–383

[100] Junqueira, L. C., Kelley, R. (1998), 'Basic Histology' , Appleton & Lange Stamford, Conn 1998. 494 p.

[101] Wambaugh, J., Shah, I. (2010), 'Simulating microdosimetry in a virtual hepatic lobule', PLoS Comput. Biol., 6(4):e1000756.

[102] Aguwa, K. (2015), 'Radiation dose study in nuclear medicine using GATE', Master of Science, University of Arizona.

[103] GATE, Physics Reference Manual, http://wiki.opengatecollaboration.org/index.php/Users_Guide

[104] Geant4, Physics Reference Manual, https://geant4.web.cern.ch/support/user_documentation

[105] Högberg, Jonas, Magnus Rizell, Ragnar Hultborn, Johanna Svensson, Olof Henrikson, Johan Mölne, Peter Gjertsson, e Peter Bernhardt. «Increased Absorbed Liver Dose in Selective Internal Radiation Therapy (SIRT) Correlates with Increased Sphere-Cluster Frequency and Absorbed Dose Inhomogeneity». EJNMMI Physics 2, n. 1 (dicembre 2015).

[106] Garin, E., Lenoir, L., Edeline, J., Laffont, S., Mesbah, H., Porée, P., Sulpice, L., Boudjema,K., Mesbah, M., Guillygomarc, A., Quehen, E., Pracht, M., Raoul, J.-L., Clement, B., Rolland, Y. and Boucher, E. (2013), 'Boosted selective internai radiation therapy with 90 Y-loaded glass microspheres (B-SIRT) for hepatocellular carcinoma patients : a new personalized promising concept', Eur. J. Nucl. Med. Mol. Imaging pp. 1057–1068.

[107] Garin, E., Lenoir, L., Rolland, Y., Edeline, J., Mesbah, H., Laffont, S., Poree, P., Clement, B., Raoul, J.-L. and Boucher, E. [2012], 'Dosimetry Based on 99mTc-Macroaggregated Albumin SPECT/CT Accurately Predicts Tumor Response and Survival in Hepatocellular Carcinoma Patients Treated with 90Y-Loaded Glass Microspheres: Preliminary Results', J. Nucl. Med. 53(2), 255–263.

[108] Garin, E., Rolland, Y., Laffont, S. and Edeline, J. [2016], 'Clinical impact of 99mTc-MAA SPECT/CT-based dosimetry in the radioembolization of liver malignancies with 90Yloaded microspheres', Eur. J. Nucl. Med. Mol. Imaging 43(3), 559–575.

[109] Kao, Y.-h., Steinberg, J. D., Tay, Y.-s., Lim, G. K. Y., Yan, J., Townsend, D. W., Takano, A., Burgmans, M. C., Irani, F. G., Teo, T. K. B., Yeow, T.-n., Gogna, A., Lo, R. H. G., Tay, K.-h., Tan, B.-s., Chow, P. K. H., Satchithanantham, S., Tan, A. E. H., Ng, D. C. E. and Goh, A. S. W. [2013], 'Post-radioembolization yttrium-90 PET/CT - part 1: diagnostic reporting', EJNMMI Res. 3(1).

[110] Petitguillaume, A. (2014), Dosimétrie Monte Carlo personnalisée pour la planification et l'évaluation des traitements de radiothérapie interne : développement et application à la radiothérapie interne sélective (SIRT), PhD thesis, Université Paris Sud.

[111] Högberg, J. et al., (2014), 'Heterogeneity of microsphere distribution in resected liver and tumour tissue following selective intrahepatic radiotherapy', EJNMMI Res 4:48.

[112] Högberg, J., Rizell, M., Hultborn, R., Svensson, J., Henrikson, O., Mölne, J., Gjertsson, P. and Bernhardt, P. (2015), 'Increased absorbed liver dose in Selective Internal Radiation Therapy (SIRT) correlates with increased sphere-cluster frequency and absorbed dose inhomogeneity', EJNMMI Phys. 2(1), 10.

[113] Högberg, J. (2015b), 'Small-scale absorbed dose modelling in Selective Internal Radiation Therapy: Microsphere distribution in normal liver tissue', Gothenburg: University of Gothenburg.

[114] Schreiner, W., Buxbaum, PF. (1993), ‘ Computer-optimization of vascular trees’, IEEE Trans Biomed Eng, 2nd Department of Surgery, University of Vienna, Wien, Austria, May;40(5):482-91.

[115] Kretowski, M., Rolland, Y., Bézy-Wendling J., Coatrieux, JL. (2003), ‘Physiologically based modeling of 3D vascular networks and CT scan angiography’, Department of Computer Science, Technical University of Balystok, Poland, IEEE Trand Med Imaging, 2003, Feb;22(2):248-57.

[116] Madrazo, Beatrice L. “Using imaging studies to differentiate among benign liver tumors.” Gastroenterology & hepatology vol. 6,7 (2010): 423-7.

[117] Bryant, M. K., Dorn, D. P., Zarzour, J., Smith, J. K., Redden, D. T., Saddekni, S., … Dubay, D. A. (2014). Computed tomography predictors of hepatocellular carcinoma tumour necrosis after chemoembolization. HPB : the official journal of the International Hepato Pancreato Biliary Association, 16(4), 327–335.

[118] Kao, Yung Hsiang, Eik Hock Tan, Chee Eng Ng, e Soon Whatt Goh. «Clinical implications of the Body Surface Area Method versus Partition Model Dosimetry for Yttrium-90 Radioembolization Using Resin Microspheres: A Technical Review». *Annals of Nuclear Medicine* 25, n. 7 (agosto 2011): 455–61. https://doi.org/10.1007/s12149-011-0499-6.